ELECTROCHEMICAL REGENERATION OF CERIC SULFATE

By

Jantje Been

B. A. Sc. (Chemical Engineering) University of British Columbia

A THESIS SUBMITTED IN PARTIAL FULFILLMENT OF

THE REQUIREMENTS FOR THE DEGREE OF

MASTER OF APPLIED SCIENCE

in

THE FACULTY OF GRADUATE STUDIES

CHEMICAL ENGINEERING

We accept this thesis as conforming

to the required standard

THE UNIVERSITY OF BRITISH COLUMBIA

April 1989

In presenting this thesis in partial fulfilment of the requirements for an advanced degree at the University of British Columbia, I agree that the Library shall make it freely available for reference and study. I further agree that permission for extensive copying of this thesis for scholarly purposes may be granted by the head of my department or by his or her representatives. It is understood that copying or publication of this thesis for financial gain shall not be allowed without my written permission.

Department of Chemical Engineering

The University of British Columbia
Vancouver, Canada

Date April 06, 1989

Abstract

Ceric sulfate slurries were regenerated electrochemically from cerous sulfate slurries in 1.6 molar sulfuric acid using a labsize tube and wire electrochemical cell. The cell consisted of a platinised titanium tube as the anode and a tungsten wire as the cathode. The reactor was run in a batchwise fashion. The anode to cathode area ratio was eleven. The dissolved ceric sulfate concentration was varied from 0 to 0.5 molar whereas the total cerium concentration was varied from 0.5 to 0.8 molar. The anode current density was varied between 90 and 250 mAmps/cm^2 with a corresponding cathode current density of 1000 to 2800 mAmps/cm^2. All runs were conducted at 50 degrees Celsius and atmospheric, or slightly above atmospheric, pressure.

In a separate voltametric study, the technique of linear sweep voltammetry was applied to both anode and cathode. Current interruption was used to correct for the iR-drop at the cathode. However, any theoretical or mechanistic modelling attempts based on the obtained kinetic data were unsuccessful. This is attributed to the presence of a highly unstable system due to the presence of adsorption processes at both cathode and anode. The potential and current readings changed with time as the thickness and nature of the adsorbed layer changed.

An empirical model, based on the data from the flow reactor, illustrated that an increase in electrolyte velocity (from 1.1 to 2.8 m/sec), an increase in total cerium concentration, or a decrease in the superficial current density gave an increase in the cell current efficiency for cerium(IV).

Some other important qualitative findings were:

- The dissolved cerous sulfate concentration was found to be a function of the dissolved ceric sulfate concentration as well as the total cerium concentration.

- It was observed that the presence of cerium sulfate solids led to an inhibition of mass transfer at the anode, resulting in a reduced electrode current efficiency for cerium(IV).

- Adsorption of cerium sulfate species on the cathode inhibits the cerium reduction reaction.The electrode current efficiency for hydrogen was never observed to be lower than 94 percent.

Table of Contents

Abstract ii

List of Tables vii

List of Figures viii

Acknowledgement x

1 Introduction 1

2 Background 5

2.1 Electrode Reactions 5

2.2 The Cerium Redox Reaction 6

2.3 Gas Evolving Electrodes - the hydrogen evolution reaction 7

2.3.1 Supersaturation 8

2.3.2 Efficiency of Gas Evolution 9

2.3.3 Mass Transfer 10

2.3.4 Superposition of Microconvective and Macroconvective Mass Transfer 12

2.3.5 Effective Conductivity 14

2.4 Preliminary Experiments 15

2.5 The Cerium(III) Oxidation Reaction 18

3 Experimental Techniques 22

3.1 The Current Interrupter Technique 22

3.2 The Rotating Disc Electrode - experimental determination of the kinetic characteristics of an electrode reaction 24

4 Apparatus and Methods **27**

4.1 Apparatus and Procedures of Kinetic Experiments 27

4.1.1 Anode Kinetic Study 27

4.1.2 Cathode Kinetic Study 31

4.2 Apparatus of the Laboratory Electrochemical Cell 34

4.3 Procedure for Obtaining Data from the Laboratory Electrochemical Cell 41

5 Results and Discussion **45**

5.1 The Dissolved Cerium(III) Concentration 45

5.2 Anode Kinetics on the Rotating Disc Electrode 48

5.3 Cathode Kinetics on the Rotating Wire Electrode 53

5.4 Modelling 59

6 Conclusions, Recommendations **70**

6.1 Conclusions 70

6.2 Recommendations 72

7 Nomenclature **73**

Bibliography **76**

A Ancillary Equipment **81**

B Calibration Curves and Analytical Methods **86**

C Experimental Results **92**

D Model Algorithm, Sample Calculations **123**

D.1 Semi-Empirical, Semi-Mechanistic Model Algorithm 123

D.2 Sample Calculation One 126

D.3 Sample Calculation Two 128

D.4 Sample Calculation Three 129
D.5 Sample Calculation Four 130
D.6 Sample Calculation Five 133
D.7 Sample Calculation Six 134

List of Tables

4.1 Ranges of the dependent and independent operating variables of the tube and wire reactor runs. 44

B.2 Calibration of the nitrogen rotameter, at STP 87

B.3 Calibration of the reactor gas rotameter, at STP 87

C.4 Slurries used in the kinetic studies 93

C.5 Partial current density data of the cerium reduction reaction on the rotating wire cathode, area 1.255 cm^2. 106

C.6 Results of cathode kinetic study, slurries A,B, and C. 107

C.7 Results of cathode kinetic study, slurries D,E, and F. 108

C.8 Results of cathode kinetic study, slurries G,H, and I. 109

C.9 Results of cathode kinetic study, slurries J,K, and L. 110

C.10 Results of cathode kinetic study, slurry M. 111

C.11 Experimental and modelling results of flow reactor run 1 113

C.12 Experimental and modelling results of flow reactor run 2 114

C.13 Experimental and modelling results of flow reactor run 3 115

C.14 Experimental and modelling results of flow reactor run 4 116

C.15 Experimental and modelling results of flow reactor run 5 117

C.16 Experimental and modelling results of flow reactor run 6 118

C.17 Experimental and modelling results of flow reactor run 7 119

C.18 Experimental and modelling results of flow reactor run 8 120

List of Figures

2.1 Method of Biegler for determining surface roughness of platinized titanium or platinum electrodes. 20

3.2 A drop in overpotential as a result of current interruption 23

3.3 Circuit of the current interrupter technique 23

4.4 Apparatus for the kinetic studies 28

4.5 Photographs of the cell(above), and the apparatus for the kinetic studies(below). 29

4.6 Rotating wire electrode 32

4.7 Methods for finding the iR-drop 35

4.8 iR-corrected potential data for two runs in 1.6 molar sulfuric acid 36

4.9 Apparatus of the laboratory electrochemical cell 37

4.10 Photograph of the electrochemical cell 38

4.11 Construction of the cell 39

5.12 Potential versus total current density data from the rotating wire cathode 54

5.13 iR-corrected potential versus total current density data from the rotating wire cathode 55

5.14 Predicted cell current efficiencies and cell potentials by 'the model' versus the experimental values obtained from the laboratory flow reactor. 61

5.15 Predicted cell current efficiencies by the empirical model versus the experimental values obtained from the laboratory flow reactor. 64

5.16 The effect of velocity on current efficiency 67

5.17 The effect of total cerium concentration on current efficiency 68

5.18 The effect of current density on current efficiency 69

B.19 Calibration curve for the nitrogen flow, at STP 88
B.20 Calibration curve for the reactor gas, at STP 89

C.21 Anode kinetic data in slurry A. 94
C.22 Anode kinetic data in slurry B. 95
C.23 Anode kinetic data in slurry C. 96
C.24 Anode kinetic data in slurry D. 97
C.25 Anode kinetic data in slurry E. 98
C.26 Anode kinetic data in slurry F. 99
C.27 Anode kinetic data in slurry G. 100
C.28 Anode kinetic data in slurry H. 101
C.29 Anode kinetic data in slurry I. 102
C.30 Anode kinetic data in slurry J. 103
C.31 Anode kinetic data in slurry K. 104
C.32 Anode kinetic data in slurry L. 105
C.33 Cell current efficiencies as determined from the gas analysis and the concentration analysis of runs 1 - 4. 121
C.34 Cell current efficiencies as determined from the gas analysis and the concentration analysis of runs 5 - 8. 122

Acknowledgement

My sincere thanks to Professor Colin Oloman and Klaus Oehr for their advice and help in this work.

Also acknowledged are the staff of the workshop and stores for their help and advice.

I would like to thank the Science Council of British Columbia for their financial support.

Finally, I like to thank Pacific Northern Gas Ltd. and B.C.Research for their support and cooperation.

Chapter 1

Introduction

In the seventies the advantages of AQ, anthraquinone, and THAQ, tetrahydroanthraquinone, as an additive in the manufacture of wood pulp became apparent [2],[46]. The use of AQ leads to 2-3 percent higher pulping yields than equivalent Kraft pulping processes and results in energy savings through a reduction of the process temperature, increased pulp production and a decrease in the amount of sulfides required which limits the generation of sulfurous gases. Since THAQ works as a catalyst only small quantities are required. In 1980, the Canadian government approved the use of THAQ and AQ in the pulp and paper industry. Consequently, the demand is expected to grow as increasing numbers of pulp mills are using the additives. One major drawback, however, is that AQ is an expensive chemical and many mills are reluctant to use it for reasons of its cost-effectiveness.

Currently, two AQ manufacturing processes are in use employing anthracene or phthalic anhydride as their raw material. The anthracene route, although it has a high AQ yield, is constrained to future expansion by the limited availability of anthracene, a minor component of coal tar. The phthalic anhydride is used with benzene and aluminum chloride in the presence of sulfuric acid to produce AQ in high yields. However, the cost of the process is relatively high as it produces an aluminum sludge which has to be disposed of.

A process utilizing naphthalene as a raw material has been developed by Kawasaki Kasei Chemicals Ltd of Japan using a vanadium pentoxide catalyst to catalytically oxidize naphthalene. Both NQ, naphthaquinone, and phthalic anhydride are produced in

approximately equal proportions which need to be separated for further treatment to produce AQ, a technically and economically difficult problem.

Oxidation of naphthalene by ceric sulphate has been described and investigated by others but so far a commercially viable NQ production method has not been developed. In order to accomplish this goal, B.C.Research has been involved in extensive research aimed at obtaining high NQ yields from the oxidation of pure liquid naphthalene by ceric sulphate. The NQ is subsequently converted to THAQ by reaction with butadiene and the ceric sulfate is regenerated from cerous sulfate by electro-oxidation on a platinized titanium anode in strong sulfuric acid. It is imperative for attaining high NQ yields that the solution produced by the electrochemical cell has a high concentration of the oxidizing agent. The cell itself should be run at high current densities to be economically feasible whereas the secondary cathodic reaction, the reduction of Ce(IV), should be suppressed to give high current efficiencies.

The following is a brief summary of the results of the B.C.Research THAQ project [2],[36].

Initially, lead dioxide was used as the anode material. It was found, however, that this was not stable at low current densities and ceric ion concentrations greater than 0.3 molar. Current is wasted by the reduction of cerium(IV) and the plating of formed Pb^{+2} ions onto the cathode. In addition, if lead dioxide is not constantly maintained at a sufficiently high negative electrode potential it reacts with sulfuric acid to form lead sulfate. Platinum and platinized titanium, on the other hand, are stable in concentrated cerium sulfate solutions.

Tungsten was chosen as the cathode material for the reason that it has a particularly high heat of adsorption for hydrogen and, consequently, does not form current limiting stable hydrides. Tungsten is attacked by turbulent ceric sulfate electrolyte if it is not sufficiently polarized.

Current efficiency was found to decrease typically with increasing anode current density but it increased with increasing cathode current density. The latter was believed to be the result of a repulsion of negatively charged ceric sulfate anions.

An increase in electrolyte velocity resulted in an increase in the current efficiency.

The ceric sulfate production efficiency was observed to decrease with increasing ceric sulfate concentration. This was primarily attributed to an increase in the partial current density of the cathodic cerium(IV) reduction reaction and a slight increase in the minimum redox potential for generating ceric sulfate.

Since the current efficiency was found to be strongly dependent on the dissolved cerium(III) concentration it was noted that it is important to maintain this concentration at a maximum, possibly by electrolyzing a cerous sulfate suspension.

An increase in temperature resulted in an increase in the ceric sulfate production efficiency but also increased gel formation and, consequently, cell voltage. A near optimum temperature was found to be 50 degrees Celsius.

During electrolysis, a non-conducting film of ceric sulfate polymer was formed on the cathode. The formation of this gel was promoted by high temperatures, high cathode current densities, low electrolyte acidity, low electrolyte velocities, and high ceric sulfate concentrations. The deposit can be removed easily using a dilute sulfuric acid ($\sim$1.0 molar) solution mixed with 0.3–0.5 molar hydrogen peroxide. Consequently, the incorporation of a cleaning cycle in the electrolysis process was suggested or the use of initially H_2O_2-spiked electrolyte in batch runs. The latter would eliminate the the need for power shutdowns which could increase the platinum and tungsten corrosion rates.

To suppress the cathodic reduction of Ce(IV) a differential area cell was employed with an anode to cathode ratio of approximately ten. This ratio enabled reasonably high anode current densities and high cell current efficiencies.

The above work led to a patented process for preparing ceric sulfate electrolytically from a saturated cerous sulfate solution or suspension at an anodic current density of

100 mA/cm^2 or higher and a cathodic currrent density of 1000 mA/cm^2 or higher in the presence of 1 to 2 molar sulfuric acid [36]. Current efficiencies as high as 95% had been observed.

The design of the electrochemical reactor is difficult because little data on the kinetics of the electrode reactions under practical (i.e. commercial) conditions of operation are available. The phenomena of gel deposition, oxide formation, as well as gas evolution at high current densities affect the electrode processes and the circumstances of mass transfer are different to those documented in the literature. These uncertainties all point to the desirability of a comprehensive reactor model based on experimental data as a basis for reactor design.

The object of this thesis was to construct a reactor model for the generation of ceric sulfate from concentrated cerous sulfate solutions in sulfuric acid. Based on experimentally obtained kinetic data, this model was to be used in the design of simple electrochemical cells such as a tube and wire differential area cell. The selection of materials as well as the variable ranges were based on the aforementioned work by BC Research.

Linear sweep voltammetry was used in the kinetic studies. Data were obtained at a platinised titanium rotating disc anode and, subsequently, at a tungsten rotating wire cathode. The total cerium concentration was varied from ~0.5 molar to ~0.8 molar. The dissolved ceric sulfate concentration was increased from ~0 molar to ~0.5 molar. The sulfuric acid concentration was held constant at ~1.6 molar. Temperature and pressure were also constant at 50 degrees Celsius and one atmosphere absolute, respectively.

In the second phase of this thesis, a flow loop was constructed containing a tube and wire cell through which the cerium sulfate electrolyte was pumped at 1 to 3 m/s.

In both, the kinetic studies and the flow experiments, the anode current density was ~100-300 mAmps/cm^2 and the cathode current density was ~1000-3000 mAmps/cm^2.

Chapter 2

Background

2.1 Electrode Reactions

In the process of the electrochemical regeneration of ceric sulfate, competing reactions are present both at the anode and at the cathode. At the anode the primary reaction is the oxidation of cerous sulfate to form ceric sulfate. This reaction is limited by mass transfer at increased potentials. The secondary reaction is the oxygen evolution reaction which is kinetically controlled.

Anode Reactions	*Reversible Potential*
	Volts, IUPAC
$Ce^{+3} \Longrightarrow Ce^{+4} + e^-$	1.46
$2H_2O \Longrightarrow O_2 + 4H^+ + 4e^-$	1.23

Similarly, at the cathode the primary reaction is the evolution of hydrogen. The reduction of ceric sulfate to form cerous sulfate is the secondary reaction.

Cathode Reactions	*Reversible Potential*
	Volts, IUPAC
$2H^+ + 2e^- \Longrightarrow H_2$	0.00
$Ce^{+4} + e^- \Longrightarrow Ce^{+3}$	1.46

The hydrogen evolution reaction is kinetically controlled whereas the ceric sulfate reduction reaction is mass transfer controlled [38]. Consequently, cathode current efficiency is promoted by high current densities whereas anode current efficiency is promoted by low current densities. The use of a differential area cell is aimed at optimizing the cell

current efficiency by producing relatively high cathode current densities together with relatively low anode current densities.

2.2 The Cerium Redox Reaction

Cerium is a member of the lanthanides with an electronic configuration of $[Xe]4f^15d^16s^2$ [12]. It readily forms the trivalent ion and is the only lanthanide that forms a stable tetra-positive species which, nevertheless, is a strong oxidizing agent. Its ready extraction into organic solvents make Ce(IV) a preferred and commonly used oxidant in organic chemistry. The Ce(III)/Ce(IV) couple is also widely used in analytical chemistry where it is preferred to the ferro-ferricyanide couple for determining electrochemical mass-transport characteristics.

The redox reaction mechanism was initially assumed by Vetter to be simply

$$Ce^{+4}_{aq} + e^- \rightleftharpoons Ce^{+3}_{aq} \tag{2.1}$$

It has now become apparent that cerium readily forms complexes with the solvent. Solvation explains the dependence of the redox potential on the nature and concentration of the acid medium. The standard potential [12] is 1.70 V in 1 molar $HClO_4$, 1.44 V in 1 molar H_2SO_4 and 1.42 V in 4 molar H_2SO_4.

In 1 - 2 molar sulfuric acid it is almost impossible to predict the extent of Ce(III) complexing but it is believed that Ce(III) exists in solution primarily as Ce^{+3} and $CeSO_4^+$ and to some extent as $Ce(SO_4)_2^-$. The $Ce(SO_4)_3^{-2}$ complex seems to be predominantly formed by Ce(IV). These remarks are based on available equilibrium constants for cerium-sulfate reactions at 25 degrees Celsius and an ionic strength of 2 for the Ce(IV) complexes and 0.5 for Ce(III) complexes. In the present project the ionic strength, μ, is expected to vary from 2 at the beginning of a run, when the Ce(IV) concentration is zero, to 3 at the end of a run when the Ce(IV) concentration is around 0.5 molar. The reaction temperature is 50 degrees Celsius. Such an increase in temperature is expected to have a significant

effect on the equilibrium constants. Temperature corrections for equilibrium constants require a knowledge of the Gibbs free energy of formation as well as enthalpy and specific heat data. This thermodynamic information is not available and thus in order to obtain a rough idea of the concentration distribution, the following available constants can be used.

$$\frac{CeSO_4^+}{(Ce^{+3})(SO_4^{-2})} = 56 \text{ mol}^{-1}.\text{l} \quad \text{at } \mu\text{=0.5, ref [8]}$$

$$= 10.5 \text{ mol}^{-1}.\text{l} \quad \text{at } \mu\text{=2, ref [35]}$$

$$\frac{Ce(SO_4)_2^-}{(Ce^{+3})(SO_4^{-2})^2} = 800 \text{ mol}^{-2}.\text{l}^2 \quad \text{at } \mu\text{=0.5, ref [8]}$$

$$\frac{(CeSO_4^{+2})(H^+)}{(Ce^{+4})(HSO_4^-)} = 3500 \quad \text{ref [18]}$$

$$\frac{(Ce(SO_4)_2)(H^+)}{(CeSO_4^+)(HSO_4^-)} = 200 \quad \text{ref [18]}$$

$$\frac{(Ce(SO_4)_3^{-2})(H^+)}{(Ce(SO_4)_2)(HSO_4^-)} = 20 \quad \text{ref [18]}$$

$$\frac{(H^+)(SO_4^{-2})}{HSO_4^-} = 0.083 \text{ mol.l}^{-1} \quad \text{ref [17]}$$

Since this project is not so much concerned with possible electrode reaction mechanisms but more with reliable kinetic data to be used for reactor design, concentration distributions are not essential and for reasons of dubious validity should merely be used as quidelines for qualitative analysis.

2.3 Gas Evolving Electrodes - the hydrogen evolution reaction

To minimize an 'electrochemical short-circuit' by reversible reactions in an undivided cell the size of the cathode needs to be reduced relative to the size of the anode. For an industrially viable process the working electrode current density, in this case the anode,

should be in the range of 100 - 300 mA/cm^2. This implies that the cathode current density is in the range of 1000 - 3000 mA/cm^2 for a reduction in size of the cathode by a factor of ten relative to the anode. The effects of gas evolution at such high current densities on the electrode overpotential are significant. The following is a literature review on the effects of gas evolution on conductivity and mass transfer as applicable to hydrogen evolution at high current densities.

2.3.1 Supersaturation

As hydrogen is produced by the reduction of hydrogen ions it initially adheres to the electrode surface as a hydrogen atom. It then combines with another hydrogen atom to form molecular hydrogen. Driven by a concentration gradient these dissolved molecules diffuse to the bulk of the electrolyte. At low current densities, of the order of a few mAmps/cm^2, the hydrogen diffusion proceeds without the formation of a gas phase.

As the electrode current density increases, the concentration of the dissolved gas at the electrode-electrolyte interface also increases and eventually reaches supersaturated levels resulting in the nucleation and growth of gas bubbles. These bubbles grow until they reach a certain size and then are detached. When rising through the electrolyte solution they grow by coalescence with other bubbles.

At very high current densities, of the order of 10,000 mAmps/cm^2, the formed bubbles, which adhere to the electrode surface at numerous nucleation sites, may interact to form a film of gas through which some current is carried by continuously shifting arcs which are formed between the electrolyte and the electrode. This so-called 'anode-effect' is marked by a sudden increase in voltage and decrease in amperage [33].

Few measurements of the level of supersaturation are available due to the experimental difficulties. Shibata [42] studied the evolution of hydrogen at a platinized platinum electrode in 1 N sulfuric acid at current densities ranging from 0.1 to 1000 mA/cm^2. The concentration of molecular hydrogen in the vicinity of the electrode was determined using

a galvanostatic potential-transient method and from the concentration overpotential. The results of both methods were in agreement and it was found that the hydrogen concentration increased with an increasing cathode current density reaching a limiting value of 160-fold the saturation gas concentration at 300 mA/cm^2.

It has to be kept in mind, however, that the level of supersaturation depends on the number of nucleating sites at the surface and, consequently, on the surface condition of the electrode. By changing the platinum surface from smooth to a mechanically ground one, the limiting gas concentration varied from 165-fold to 23-fold the saturation value [49]. In addition, the surface condition may be affected by gel formation. Roald and Beck [40] found in their study on the dissolution of magnesium in hydrochloric acid that the formation of an aluminum hydroxide gel restricted the hydrogen bubble growth.

Independent methods based on bubble growth data and data for the fractional gas coverage of the electrode surface resulted in much lower supersaturation levels indicating the need to distinguish between the supersaturation level responsible for nucleation and the supersaturation level, at a short distance from the electrode, governing bubble growth [49]. The latter is of main importance in mass transfer enhancement whereas the first determines the concentration overpotential.

2.3.2 Efficiency of Gas Evolution

Until recently it was assumed that nearly all the gas generated at electrodes in dissolved form was transformed into gas bubbles which adhere to the electrode before departing to the bulk of the solution. New studies have indicated that, in reality, this view is far from the truth [52], [53]. In the entire regime of nucleate gas evolution the efficiency of gas evolution is smaller than unity. This means that only a fraction of the total amount of dissolved gas generated is evolved at the electrode in the form of gas bubbles. The efficiency of gas evolution is a function of the difference in the dissolved gas concentration at the electrode and in the bulk of the solution. In addition, it is dependent on the current

density, the bubble departure diameter as well as on the fractional surface coverage and, naturally, on the diffusion coefficient of hydrogen.

The dissolved gas concentration at the electrode-electrolyte interface can be determined by the methods used and described by Shibata [42]..

Vogt obtained efficiency values for the evolution of hydrogen gas of 30% at 100 mA/cm^2 to 65% at 3000 mA/cm^2 [52]. These calculations were based on the micro-convective model, which will be discussed later, and the mass transfer coefficient due to macroconvection. Janssen and Barendrecht experimentally measured the efficiency for hydrogen evolution using high speed photography and found it to be approximately constant at 75% for current densities of 10 - 100 mA/cm^2 [28]. It is believed that their value is significantly higher than the efficiency as calculated by Vogt since it is determined from pictures taken just above the top of the working electrode. The volume of gas at that point has increased due to gas absorption by the rising bubbles.

The determination of the gas evolution efficiency cannot be generalized since it depends on supersaturation data which in turn depends on the particular conditions of the experimental apparatus. The efficiency can also be determined independently from bubble growth data [53]. This method, however, is found to be inferior to the one described above due to highly scattered experimental data.

Nevertheless, it can be concluded that the efficiency of gas evolution is generally much less than unity in the range of industrial current densities.

2.3.3 Mass Transfer

After nucleation, there is a period of bubble growth during which the growing bubble pushes liquid past the electrode in radial directions. The micro-convective model assumes these convective currents to be primarily responsible for mass transfer within the boundary layer. Stephan [45] presented such a model with reference to models for heat transfer phenomena in nucleate boiling. A dimensionless correlation was presented based

on the break-off bubble diameter as the characteristic length:

$$Sh = 0.93 Re^{0.5} Sc^{0.487} \tag{2.2}$$

where, $Sh = \frac{k_c d}{D}$, $Re = \frac{V_G d}{A\upsilon}$, $Sc = \frac{\upsilon}{D}$

However, no satisfactory method to determine the bubble diameter is available and, consequently, mean values from experiments are often used in the above equation. In acidic electrolyte, this diameter for hydrogen is 60 μm and for oxygen 40 μm. But at the high current densities of this thesis significant coalescence is expected to take place leading to higher diameters. When extrapolating the data obtained by Janssen and Hoogland, diameters varying from 430 μm to 2000 μm are obtained for current densities in the range of 1000 mA/cm^2 to 3000 mA/cm^2 [25].

On the other hand, as mentioned before, the formation of a gel layer may limit the break-off diameter to a smaller value. Substituting a smaller diameter into the above equation gives a larger mass transfer coefficient which again results in a lower supersaturation level sustaining bubble growth. Janssen confirmed that the electrode material could have a significant effect on the diffusion layer thickness [26]. He observed that hydrogen bubbles rising from a Ni-Teflon electrode in alkali were very big with a diameter of 0.24 cm at a current density of 100 mA/cm^2. The diffusion layer thickness was, consequently, greater than for other materials such as pure nickel and platinum. Janssen also investigated the effects of electrode roughness and found that when the mechanically applied grooves were smaller in depth and width than δ, electrode roughness does not significantly affect the diffusion layer thickness [26]. Since gel formation is present at the cerium(IV) concentrations used in the present work and since observation of the bubbles produced was not possible due to the opaqueness of the solution, a suitable break-off bubble diameter can only be guessed at. In general, the bubble size decreases strongly with increasing velocity and increases with increasing current density [25].

Stephan compared a wide range of experimental data with the micro-convective model [45]. The data included hydrogen, oxygen, and chlorine evolution on a wide range of

electrode materials from acidic or alkaline electrolytes. The Schmidt number varied from 160 to 23,000 and the Reynolds' number ranged from 3×10^{-6} to 0.9. Current densities were as low as 0.3 mA/cm^2 and as high as 10,000 mA/cm^2. The model fit the data fairly well even though the scatter was much greater than for similar equations of heat transfer in boiling. The reason for this is mainly the simplicity of the model and the wide range of experimental parameters.

In the above mass transfer correlations the efficiency of gas evolution was assumed to be 100%. Further studies have indicated that this efficiency is actually much lower than 100%, sometimes as low as 30-50% for current densities within the industrial range [52], [53]. Vogt admits that when the micro-convective model is corrected for these new efficiencies in the range of usual industrial current density values, the obtained mass transfer coefficients are about 30% too low [52]. Until the models have been modified and fitted with corrected numerical factors it is suggested to use the above correlations as if the efficiency of gas evolution is 100%.

2.3.4 Superposition of Microconvective and Macroconvective Mass Transfer

The macroconvective mass transfer coefficient can be approximated well with the equation of Chilton and Colburn for turbulent heat and mass transfer. The equation is based on the equivalent hydraulic diameter and reads

$$Sh = 0.023(Re)^{0.8}(Sc)^{1/3} \tag{2.3}$$

For mass transfer at high Schmidt numbers the assumed velocity profile is of little importance. Also at high Reynolds numbers the mass transfer boundary layer is very thin. Consequently, the above empirical correlation may be applied to flow in smooth tubes, pipes, annuli as well as to flow between parallel plates. The Chilton-Colburn relation seems to be superior to other semi- empirical models [24] for

$$10^4 < \mathrm{Re} < 5{\times}10^4$$

$$10 < \mathrm{Sc} < 5\times10^3$$

An increased electrolyte velocity increases the macro-convective mass transfer but, in addition, it lowers the supersaturation levels near and at the electrode surface. As a result, an increase in velocity has a direct effect on such parameters as bubble departure diameter and gas evolution efficiency and thus decreases microconvective mass transfer. On the other hand, an increase in current density increases supersaturation levels, bubble departure diameters and, hence, results in a greater microconvective mass transfer. The larger bubbles and the greater number of bubbles shield a greater fraction of the electrode surface, impeding macroconvective mass transfer [4].

The overall mass transfer coefficient can be found from the design equation proposed by Vogt which involves the interaction of both macro- and microconvection and which is found to be superior to the simple addition of the individual mass transfer coefficients [55]:

$$k = (k_{mc}^2 + k_c^2)^{0.5} \tag{2.4}$$

A theoretical approach has been attempted, however, the above equation is simpler to use and fits experimental data well [48].

In the kinetic study of this project a rotating wire electrode is used. Eisenberg, Tobias and Wilke [14] studied ionic mass transfer and concentration polarization at vertical rotating electrodes and found empirically that the diffusion layer thickness depended on the kinematic viscosity, diffusion coefficient, rotational speed, and on rotor diameter by:

$$\delta = 99.62\frac{d_i^{-0.40}\upsilon^{0.344}D^{0.356}}{S^{0.70}} \tag{2.5}$$

Using this correlation makes it possible to translate the data from the rotational electrode to useful predictions about similar electrochemical systems with different hydrodynamic flow patterns.

2.3.5 Effective Conductivity

Extensive research has been done to evaluate the effects of gas bubbles on the overall electrolyte conductivity. The theoretical equations as developed by Maxwell and Bruggeman regarding uniformly dispersed gas phases are still considered far superior to all other theoretical and empirical models that have since been developed.

More recent studies, however, have led to many valuable qualitative and quantitative observations. Sides found that a bubble attached to the electrode obstructs the current flow less than a bubble dispersed in the bulk of the solution [43]. He determined, based on theoretical models, the increase in the resistance to be negligible if the attached bubbles are more than three diameters apart. For void fractions greater than 0.2 he found Maxwell's equation to be most satisfactory [44].

Maxwell equation:

$$K_m = \frac{1-f}{1+\frac{f}{2}} \tag{2.6}$$

Bruggeman equation:

$$K_m = (1-f)^{3/2} \tag{2.7}$$

In practice, Kuhn [30], and later Bongenaar-Schlenter [9], suggested the existence of a very thin crowded bubble layer adjacent to the electrode which is formed immediately and, at very low gas production rates, adds a significant resistive element. Consequently, the presence of two regions is now generally accepted. The first region, the bubble layer next to the electrode, has a high bubble density which decreases to a bulk bubble concentration over a certain distance called the bubble layer thickness. Based on this concept Bongenaar-Schlenter et al. [9] developed a new model applying the Bruggeman equation to the varying void distribution over the interelectrode gap.

This approach requires assumptions regarding the voidage at the electrode and the void distribution away from the electrode. Assuming a one hundred percent efficiency of gas evolution, the bulk voidage is only a few percent of the total volume and can be

neglected. Near the electrode, the ohmic effect is much greater and the gas void fraction as a function of the distance from the electrode depends on current density, liquid velocity, bubble diameter, solution composition and, possibly, the extent of gel formation. The latter affects the substrate characteristics on which the bubbles are formed. Reliable data for parameters such as bubble diameter, the solution composition near the electrode surface and the extent of gel formation are not available and, consequently, a theoretical approach to determine the gas voidage profile is not available.

The conductivity is a function of all of the above conditions. Temperature and pressure are constant throughout the project, at the rotating wire electrode and the flow reactor, and are, therefore, not considered as variables. Generally, an increase in pressure and/or a decrease in temperature affects the conductivity through an increase in the proportion of dissolved gas carried off with the electrolyte [29]. It is possible to relate the rotating electrode hydrodynamics to the actual cell liquid flow velocity through the diffusion layer thickness. Then,

$$\kappa_e = f(i_t, \delta, Ce^{+3}conc., Ce^{+4}conc., d_{wm}) \tag{2.8}$$

2.4 Preliminary Experiments

Initially, an attempt was made to obtain the kinetics of the hydrogen reaction on tungsten using a rotating disc electrode. The objective was to obtain overvoltage data as a function of current density, cerium(IV) concentration and possibly cerium(III) concentration. Since the hydrodynamics are well known and the convective-diffusion equation has been solved rigorously for the steady state of rotating disc electrodes in the absence of gas evolution, it was hoped to obtain additional information regarding the diffusion layer thickness and maybe values of the exchange current density and transfer coefficients. However, the construction of the rotating disc was such that the active electrode area was located face down in the solution. A bubble adhered to the electrode, grew by coalescence to a steady-state size and then remained attached to the electrode in the center

of the rotating disc. Needless to say, the effect on the ohmic potential was significant, especially at the small electrode, which, with an area of 0.012 cm^2, was often completely covered.

Since the hydrogen evolution reaction was expected to be entirely in the kinetic regime and not limited by mass diffusion at a sulfuric acid concentration of 1.6 molar, potentiostatic measurements were taken at a stationary electrode. It was then that many of the problems came to light.

In saturated cerium(III) solutions with high concentrations of cerium(IV) ,0.2-0.5 molar, and 1.6 molar sulfuric acid, the current density was observed to drop about 20% at a value of 200 mA/cm^2 as the speed of the stirrer bar was decreased from full speed to medium speed. The drop in current density was less at higher current densities.

In concentrated cerium solutions, gel formation on the cathode surface resulted in a large increase in the ohmic resistance. The gel is believed to consist of cerium sulfate complexes. Two different deposits are observed, both being highly resistant to current flow. One deposit had a yellow, almost flower-like appearance originating at the edges of the exposed electrode area and growing towards the center in the form of leaves of a longitudinally stratified crystal-like deposit. The second type of deposit appeared as a thin transparent film with a yellowish shine. Since the stratification of the first deposit seemed to coincide with the longitudinal grooves on the rough tungsten surface, it appeared that gel formation is favored by rough surfaces. Consequently, a pure tungsten welding rod with a smooth etched surface was tested and gel formation over the time of the experiment was reduced significantly to the extent that it was negligible.

It was difficult to obtain reproducible steady state current values. The current decreased as a function of time and often approached constant values only after long periods of time (30 - 50 min). Even after such long time-periods the current fluctuated due to a high rate of gas evolution.

In addition, the electrode history seems to be important in the concentrated cerium

solutions. It was found that at a low potential the current could be increased by moving the potential to a higher cathode potential and then back to the potential being investigated. First it was thought that the transparent gel layer on the main body of the electrode dissolved at higher current densities due to a more vigorous hydrogen evolution which physically disrupted the gel and/or to the electrochemical reaction of the gel to form cerous sulfate. This, however, would lead to a more transient behavior after which the gel would be reformed decreasing the current density. Such a transient behavior was not observed.

The above procedure was useful in the identification of some of the problems. However, the data obtained cannot be used quantitatively since the hydrogen overpotentials in concentrated cerium solutions do seem to depend on the hydrodynamics of the solution. Using a magnetic stirbar produces turbulent flows of an unknown and unmeasurable nature.

Harrison, in his study on the effect of bubbles on the measured electrochemical parameters during hydrogen evolution on nickel, experienced many of the same difficulties [22]. He found that at a rotating disc electrode the approach to steady state was slow, taking longer than 100 seconds and even longer at stationary electrodes. He concluded that "the mechanism of bubble formation, growth, packing and eventually detachment are responsible for this effect" [22] since diffusion reaches steady state relatively quickly. Consequently, a hysteresis effect or 'memory effect' was observed. In addition, he found that "the exact value of the Tafel slope depends on the extent of the bubble layer and is a function of surface roughness and the anion present in the solution" [22]. In the present research the Tafel slope is also expected to vary with cerium(IV) concentration due to possible gel formation. This dependency of the Tafel slope and the transfer coefficient on the electrode potential is due to the inhibiting effect of the hydrogen bubbles on the charge transfer reaction. A gel on the electrode surface is expected to have a similar inhibiting effect.

2.5 The Cerium(III) Oxidation Reaction

Oxide formation at highly anodic potentials is a well known occurrence at platinum electrodes. Two oxides have been distinguished [38], [39], [31] commonly known as oxides I and II or oxides α and β.

Oxide I forms at around 1.0 Volt SHE and reaches a limiting value upon continued oxidation corresponding to a monolayer of PtO_2 in dilute sulfuric acid (< 1.0 molar). At higher concentrations this limiting value decreases, yet the oxide coverage does not seem to be affected by the presence of cerium. The specific conductance of oxide I is the same as for platinum metal and, consequently, the oxide does not inhibit the cerium reaction kinetics. On the other hand, the oxygen evolution reaction, the anode's secondary reaction, is strongly inhibited and for this reason it is important to maintain the nature and the thickness of oxide I well defined.

At potentials of 2.0 Volts SHE and higher, oxide II begins to form upon prolonged oxidation [39] and its thickness increases indefinitely with time. A current inhibiting effect is experienced even at sub-monolayer amounts and a decrease in exchange current densities and transfer coefficients of the cerium redox reaction is observed. In addition, oxide II catalyzes the oxygen evolution reaction and it is, therefore, beneficial to avoid its formation by keeping the electrode potential below 2.0 Volts SHE.

In order to obtain a constant oxide layer, Kuhn and Randle [38], [39], [31] followed a potential program in which the electrode was initially cleaned and polarized negatively to remove any existing oxides. It was then kept at a positive oxidation potential for a cerain constant time period to create a reproducible oxide layer. The oxidation voltammogram was subsequently obtained starting at the most anodic limit of the potential scanning range which is still cathodic to the potential of oxide formation. Since the oxygen reduction reaction has a large hysteresis effect, the oxide was not reduced and no further oxide growth was observed.

Repeated formation and reduction of oxides, especially oxide II, causes extensive

electrode roughening. To obtain valid exchange current densities it is important that the area is constant throughout a particular run. The area should, therefore, be measured before and after each run to note any changes. This can be done using the method of Biegler [5], [6]. This method consists of a potential program which is initially the same as the one previously described. After the oxidation potential, the potential is lowered and the solution is purged with nitrogen to eliminate any interference from dissolved oxygen. The adsorbed oxygen is, subsequently, reduced during a cathodic sweep between the potentials 1.440 Volts SHE and 0.040 Volts SHE followed by a triangular potential cycle. The latter is included to assure that all of the oxygen has been reduced before hydrogen adsorption begins at the most cathodic potentials. The total charge passed to reduce the oxygen, Q_{ox}, and the charge required to form a monolayer of hydrogen, Q_h, can be obtained from the areas underneath the peaks of the cathodic current-potential curves. Q_h is a measure of the effective surface area whereas $Q_{ox}/2Q_h$ gives an impression of the oxide thickness (see Figure 2.1).

The method of Biegler was used to determine the increase in surface roughness over the duration of the present research project. The surface roughness was found to have increased by a factor of three. Yet, there did not seem to be a corresponding change in current-potential values. This might be attributed to the much higher cerium concentrations of this work which may lead to significant adsorption of cerium sulfate complexes onto the electrode. Kuhn and Randle [31] did suspect the adsorption of cerium(III) species at higher potentials to suppress the oxygen evolution reaction, in particular negative cerium(III) complexes such as $Ce(SO_4)_2^-$. Their work involved a rotating platinum disc electrode in 0.15 molar sulfuric acid and cerium concentrations of the order of 10-20 mmol/l at room temperature. In this project the acid concentration is threefold higher whereas the cerium(III) concentration is approximately 0.2 - 0.3 molar and the cerium(IV) concentration varies from 0 to 0.5 molar. The process temperature is 50 degrees Celsius. The kinetic parameters obtained by the previous authors can, therefore,

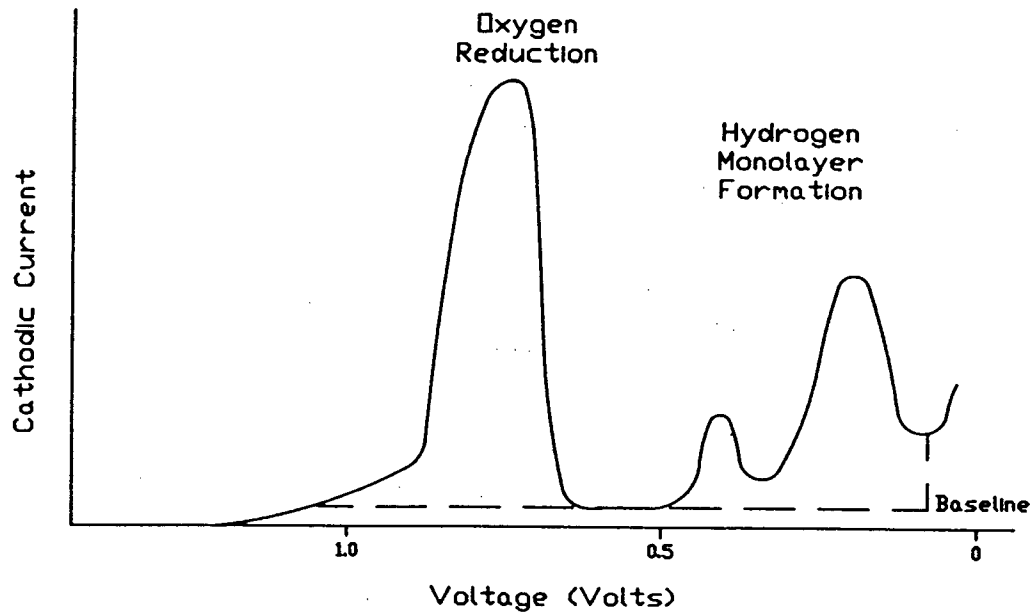

Figure 2.1: Method of Biegler for determining surface roughness of platinized titanium or platinum electrodes.

not be extended to this project due to solution composition changes with acid, cerium, and sulfate concentrations and a possible identity change of the electroactive species at the high concentrations involved. Kinetic data of the cerium reaction at these high concentrations and temperature are not available in the literature.

Chapter 3

Experimental Techniques

3.1 The Current Interrupter Technique

The use of a reference electrode with a Luggin capillary placed close to the working electrode largely compensates for the iR-drop of the electrochemical cell. The remaining voltage drop is often small but not negligible and needs to be accounted for. Positive feedback is a widely used compensatory technique when the resistance is a constant value. At gas evolving electrodes this resistance is far from constant as it increases with increasing current densities and gas volumes.

The principle of the current interrupter technique is simple [10], [23]. As soon as the cell current is interrupted the potential difference between the working electrode and the reference electrode drops instantaneously by a value equal to iR after which it decays with a time constant RC characteristic of the cell (see Figure 3.2). Figure 3.3 shows the principle components of the circuit with the equivalent electrical analogue for the electrochemical cell. A mercury wetted contact relay was used as the switch and could be triggered manually using a toggle switch on the function generator. The latter would trigger the oscilloscope simultaneously. The storage oscilloscope could store several time frames before as well as after its triggering time so that the entire iR-drop was recorded. This same technique was used by Shibata [42] to measure the concentration overpotential of hydrogen molecules at a hydrogen evolving electrode. It was reasoned that the remaining polarization after current interruption consisted of concentration overpotentials of the hydrogen ions and hydrogen molecules. Furthermore, at high acid concentrations the hydrogen ion concentration overpotential could be considered negligible and

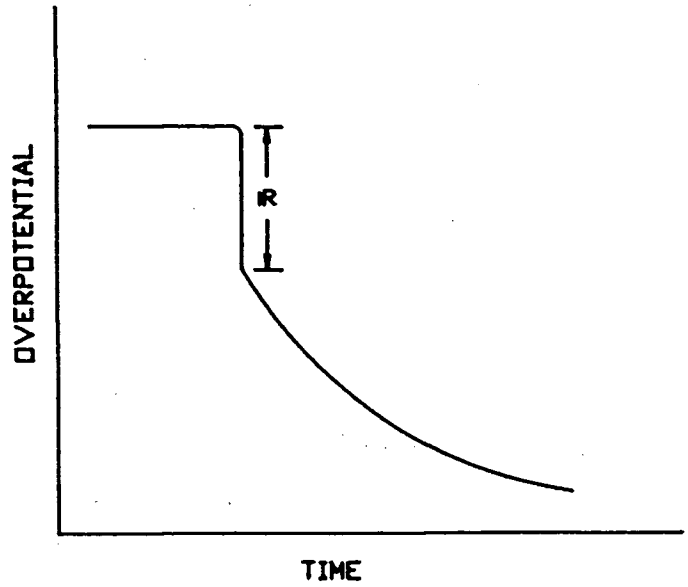

Figure 3.2: A drop in overpotential as a result of current interruption

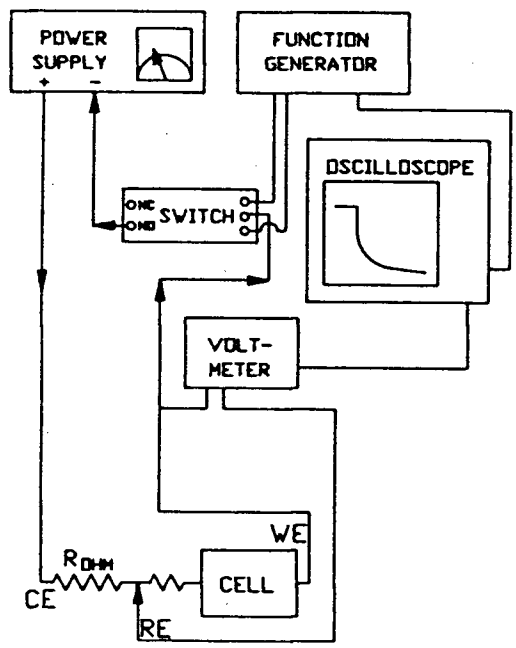

Figure 3.3: Circuit of the current interrupter technique

was consequently disregarded. The overpotential is related to the supersaturation level of hydrogen by

$$\eta_c = \frac{-RT}{2F} ln\, p^* \tag{3.9}$$

where p^* is the supersaturation ratio.

3.2 The Rotating Disc Electrode - experimental determination of the kinetic characteristics of an electrode reaction

The method of the rotating disk electrode is a popular electrochemical research technique owing to the relative simplicity of the technique and the availability of a rigorous quantitative theory permitting the determination of a wide variety of kinetic characteristics of electrochemical reactions. For a complete, in depth discussion see Pleskov and Filinovsky [16], [37].

The kinetic parameters that might be obtained by this technique are i_{lim}, D, i_o, α, the reaction order μ, and the electrochemical rate constant k_{rxn}. This rate constant is a function of the chemical rate constant, $k_{chem.rxn}$, and the potential difference between the metal and the outer Helmholtz plane. It can be written as

$$k_{rxn} = k_{chem.rxn} \exp(-\alpha VF/RT) \text{ or } k_{rxn} = k_{chem.rxn} \exp((1-\alpha)VF/RT)$$

In most cases, the limiting current density can be obtained experimentally by increasing the overpotential. The diffusion coefficient can then be determined from

$$i_{lim} = 0.62nFD^{2/3}C_b v^{-1/6}\omega^{1/2} \tag{3.10}$$

where n is the number of electrons consumed in the reaction. The above equation is the solution of the convective diffusion equation to a homogeneous disk surface.

The reaction kinetics can generally be described by

$$i = nFk_{rxn}C_s^{\mu} \tag{3.11}$$

where C_s is the reactant concentration at the surface. If there were no current limitations imposed by mass transfer the resulting 'kinetic current density' is given by

$$i_k = nFk_{rxn}C_b^{\mu} \tag{3.12}$$

Also, in the presence of excess supporting electrolyte

$$i_{lim} = \frac{nFDC_b}{\delta} \tag{3.13}$$

From Fick's law for the rate of mass transfer

$$\frac{D}{\delta} = \frac{i}{nF(C_b - C_s)} \tag{3.14}$$

Substituting 3.14 into equation 3.13 gives

$$i_{lim} = i\frac{C_b}{C_b - C_s} \tag{3.15}$$

$$C_b = \frac{i_{lim}C_s}{i_{lim} - i} \tag{3.16}$$

By substituting 3.16 into 3.12 and dividing 3.12 by 3.11 one obtains

$$\frac{i}{i_k} = \left[1 - \frac{i}{i_{lim}}\right]^{\mu} \tag{3.17}$$

The reaction order can then be determined from the ratio of measured current densities taken at two different electrode rotational speeds at the same potential.

$$\mu = ln\left[\frac{i^{(1)}}{i^{(2)}}\right] \Big/ ln\left[\frac{(i_{lim}^{(1)} - i^{(1)})i_{lim}^{(2)}}{(i_{lim}^{(2)} - i^{(2)})i_{lim}^{(1)}}\right] \tag{3.18}$$

Superscript 1 refers to one set of data taken at ω_1 whereas superscript 2 refers to the set of data taken at ω_2.

If equation 3.16 is substituted into equation 3.11 an expression for the rate constant is obtained

$$k_{rxn} = i[nFC_b^{\mu}(1 - i/i_{lim})^{\mu}]^{-1} \tag{3.19}$$

A well known general kinetic equation taking into account both the forward and backward reaction is the Butler-Volmer equation:

$$i = i_o \left\{ \left[\frac{C_{Os}}{C_{Ob}}\right]^{\mu} exp[-\alpha nF\eta/RT] - \left[\frac{C_{Rs}}{C_{Rb}}\right]^{\mu} exp[(1-\alpha)nF\eta/RT] \right\} \tag{3.20}$$

At pure kinetic control, which is approached experimentally at an infinite rotation speed, the surface concentration equals the bulk concentration and the kinetic equation reduces to

$$i_k = i_o \left\{ \frac{1 - exp(nF\eta/RT)}{exp(\alpha nF\eta/RT)} \right\} \tag{3.21}$$

By obtaining experimental data at various angular velocities a plot of 1/i versus $1/\omega^{1/2}$ can be extrapolated to give an intercept of $1/i_k$ at an infinite rotation speed. From this intercept the exchange cd as well as the transfer coefficient can be determined if the above is repeated for different overpotentials.

When the overpotential is greater than about 0.1 Volt, the assumption is often made that the reverse reaction is negligible. In the region of kinetic control the Butler-Volmer equation is then reduced to the Tafel equation

$$\eta = \frac{RT}{\alpha nF} ln\, i_o + \frac{-2.303RT}{\alpha nF} log\, i \tag{3.22}$$

which can now be used to evaluate i_o and α.

Chapter 4

Apparatus and Methods

The experimental portion of this work consists of a kinetic study, aimed at finding anodic and cathodic kinetic parameters on a rotating disc or wire electrode, followed by a series of runs on a labsize differential area electrochemical cell. The apparatus and methods employed in the kinetic study will be described separately from work on the laboratory cell.

4.1 Apparatus and Procedures of Kinetic Experiments

4.1.1 Anode Kinetic Study

Figure 4.4 represents a line diagram of the electrical equipment and its arrangement for the anode and cathode kinetic study. Photographs of the equipment and the cell are presented in Figure 4.5.

In the anode kinetic study a rotating disc electrode was used with a platinised titanium disc inserted at the bottom of a Teflon sleeved stainless steel shaft which in turn was connected to a rotator. The superficial active electrode area was 1.23 cm^2. The reference electrode, a saturated calomel electrode, was inserted in a pyrex glass tube with a luggin cappillary which was placed close to the working electrode ($\sim$2 mm). The counter electrode consisted of platinised titanium about 4 cm^2 in area. These electrodes were all positioned in a 1 liter pyrex glass vessel which contained the cerium solution and which was kept at 50 degrees Celsius by a heating tape and a temperature controller. Since the electrolyte was often in the form of a slurry the solids were kept suspended by a magnetic stirrer. The effect of this stirrer was found to be insignificant in the experimental range

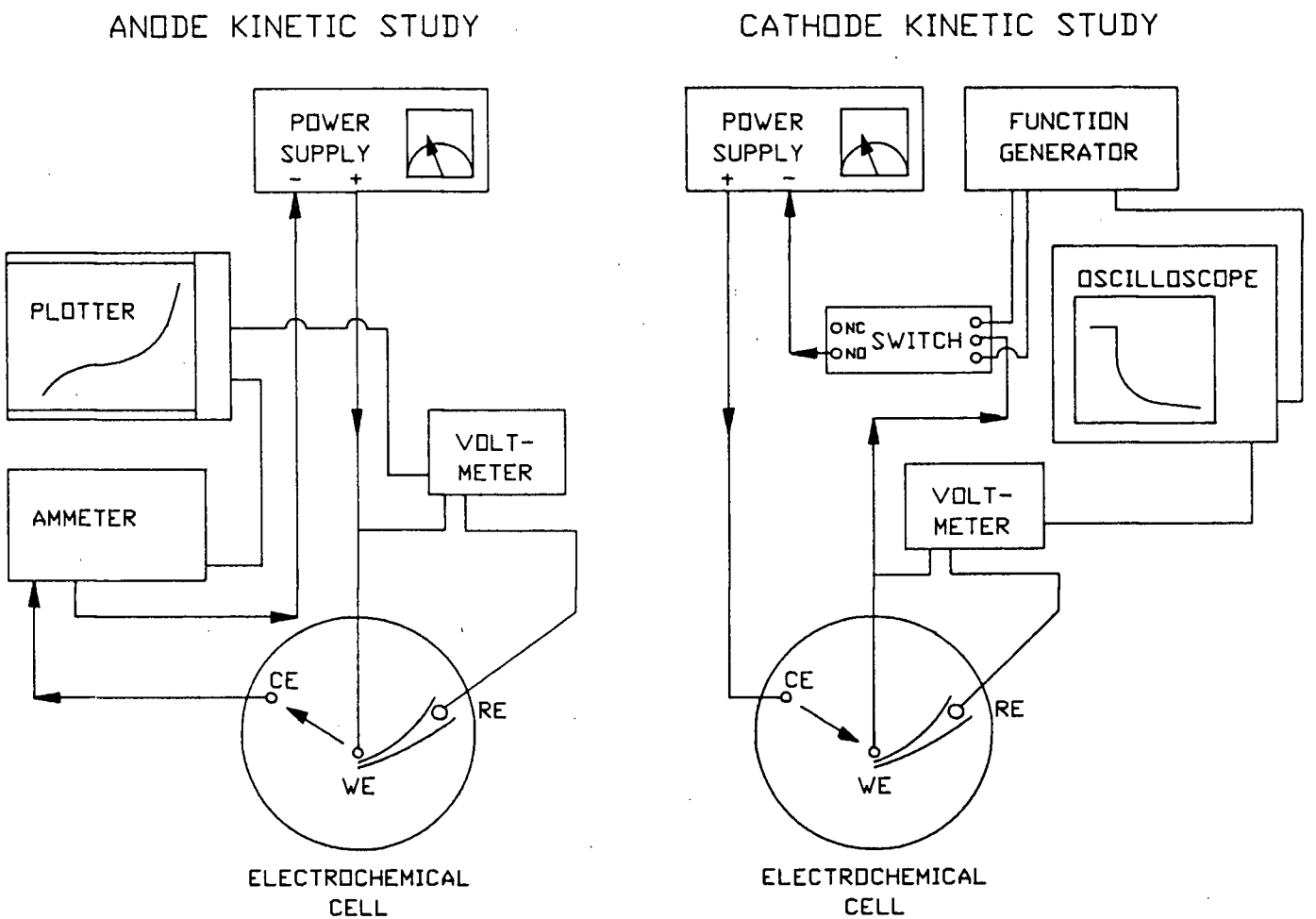

Figure 4.4: Apparatus for the Kinetic Studies

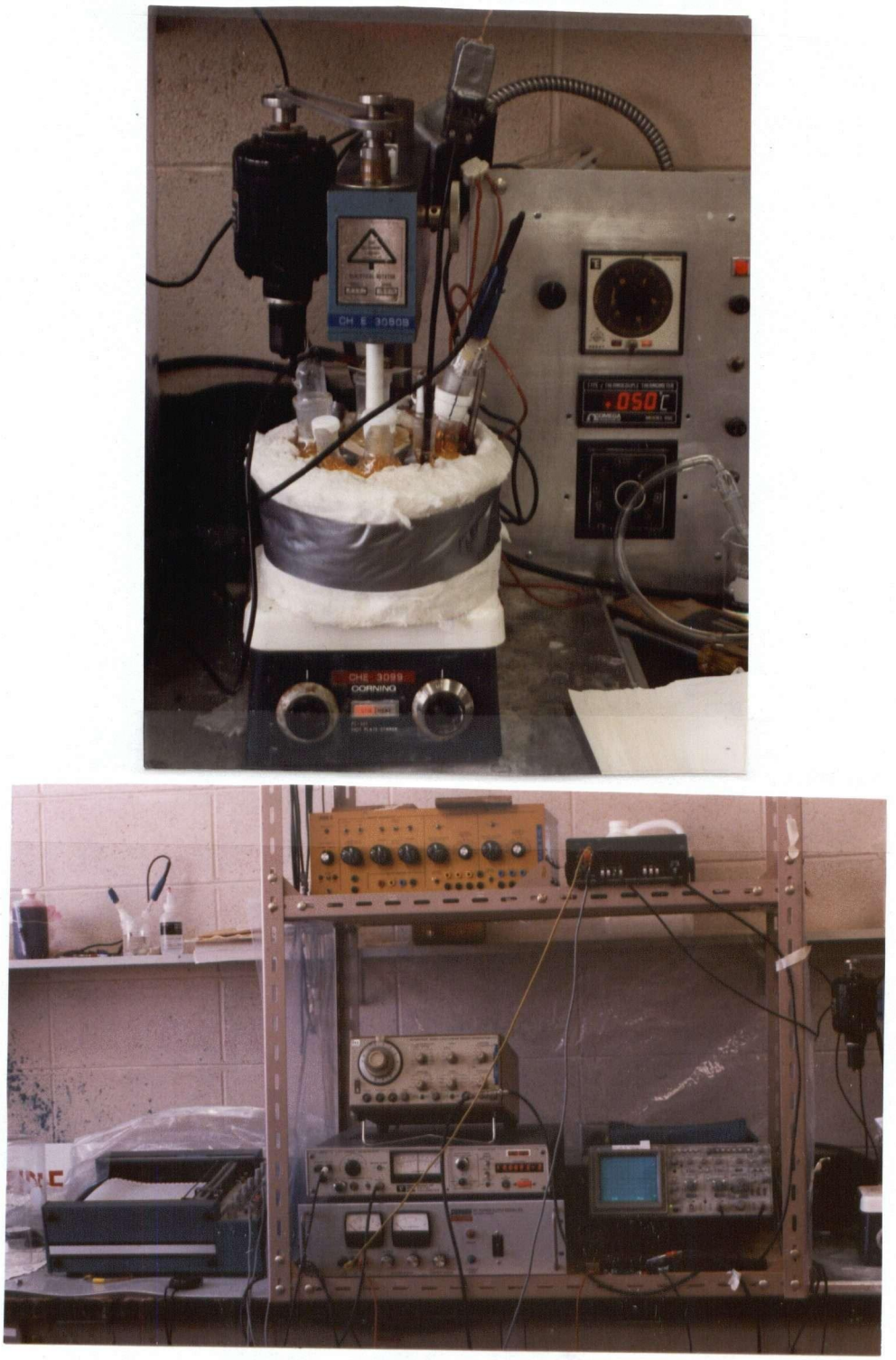

Figure 4.5: Photographs of the cell(above), and the apparatus for the kinetic studies(below).

of rotational speeds.

The distance between the working electrode, WE, and the luggin capillary was measured carefully in a clear solution of distilled water upon which this position was marked on both the reference and the working electrode. Using these markings, subsequently, to place the electrodes in the vessel gave an average distance between the WE and the luggin cappillary of 2mm $\pm$ 0.5mm. This procedure permitted proper positioning of the electrodes in the opaque cerium slurry.

A current density of 300 mAmps/cm^2 gives a total current which is outside the range of the available potentiostat and, consequently, an ordinary DC power supply was used[1]. A potential was applied to the cell between the working electrode and the counter electrode. The potential between the reference electrode and the working electrode was measured by a high impedance voltmeter. The current was passed through an ammeter with a current/voltage converter. This potential as well as the potential from the voltmeter was plotted by the XY recorder.

The current-interrupter technique was used to observe the iR-drop up to current densities on the WE of 300 mAmps/cm^2. In slurry A, the iR-drop was ~zero Volts whereas at 300 mAmps/cm^2 it was ~0.1 Volts with an anode potential of 2.4 Volts. The iR-drop appeared to be negligible and, consequently, was ignored in subsequent runs.

A total of twelve different slurries were used, characterized by different cerium(IV) and total cerium concentrations. These slurries A through L are listed in Table C.4, Appendix C, and contain dissolved Ce^{III} and Ce^{IV} as well as suspended cerous sulfate solids. The sulfuric acid concentration is 1.6 molar. Prior to inserting the working electrode in the electrolyte, it was soaked in nitric acid for 5 minutes after which it was thoroughly rinsed with distilled water. In each slurry, the rotational speed was varied from 1000 to 3000, 4000, 5000, and 7000 rpm. At each rotational speed, the WE-potential was initially held at 0.040 Volts(SHE) for 30 seconds after which the potential was increased until the

[1] A smaller disc could not be platinised whereas machining the platinised disc could lead to extensive damage of the platinum coating.

current density was approximately 325 mAmps/cm^2. After 60 seconds, the potential was decreased slowly at a rate of 0.12 Volts/min returning to the potential of 0.040 Volts. This was done manually in small steps. Since the kinetic behavior of the reactions varied from one slurry to the next, a constant oxidation potential, for example 2.5 Volts(SHE), would give very high currents in some slurries such as D, E, and F which could lead to permanent changes of the electrode surface due to, for instance, oxide II formation. Consequently, a constant oxidation current density of 325 mAmps/cm^2 was used. The results are plotted in Appendix C, Figures C.21-C.32.

4.1.2 Cathode Kinetic Study

In the cathode kinetic study a rotating wire electrode was used. The superficial electrode area was 1.26 $\pm$ 0.03 cm^2 and the rod was 0.47 cm in diameter. The electrode area was on both sides bounded by a glass seal. The remainder of the shaft was covered with three to four layers of Teflon tape to prevent corrosion of the shaft in the acidic vapor leaving the vessel at high current densities. For a photograph of the electrode see Figure 4.6.

Positioning of the working electrode(WE) and the reference electrode(RE) was calibrated in a similar manner as for the anode rotating disc electrode. Again, the distance between the luggin cappillary and the WE was on the average 2 mm with a somewhat larger uncertainty of 1 mm.

As shown in Figure 4.4, the power supply is again used to apply a potential between the WE and the counter electrode(CE). The currents in this study are generally much higher, up to 4.5 Amperes, and, consequently, the Ammeter with a maximum current capacity of one Ampere cannot be used. The current indicator on the power supply is thus used for current values. Potential values are obtained from the voltmeter which reads the potential difference between the WE and the RE. High iR-drops were expected and observed using the current-interrupter technique. A mercury wetted contact relay was installed in the circuit which could be triggered manually using the function generator.

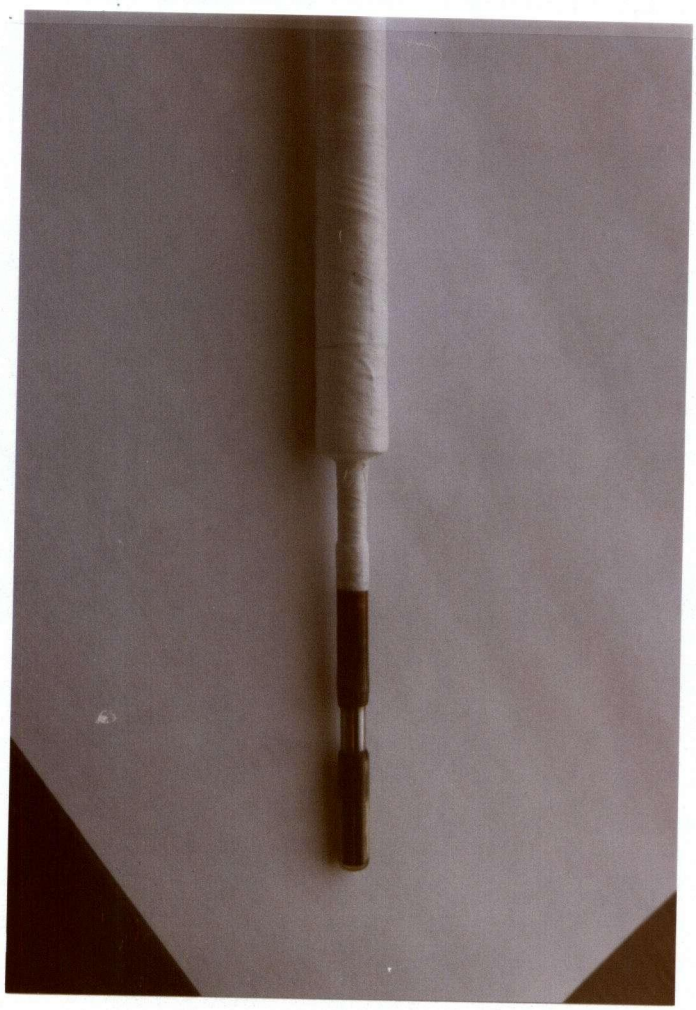

Figure 4.6: Rotating wire electrode

The latter would trigger the storage oscilloscope simultaneously. The oscilloscope had the nice feature that it could store several time frames before its triggering time in addition to several time frames after its triggering time. This assured that the entire iR-drop was recorded which was then photographed and analyzed.

The area of the counter electrode was reduced to approximately 1 cm^2 to limit the cerium oxidation reaction in an attempt to maintain the concentrations constant throughout the duration of the experiment.

The same slurries as for the anode study were used with one additional slurry, slurry M. Before installing the electrode and placing it in the electrolyte, it was sanded with fine emery paper until it had a shiny appearance. It was then soaked in nitric acid for about 5 minutes after which it was rinsed thoroughly with distilled water. Once in the electrolyte, the current was increased from 0.5 Amperes to 4.5 Amperes stepwise in increments of 0.5 Amperes followed by a stepwise decrease returning to 0.5 Amperes. Apparently stable potential values were recorded for each current value. This sweeping was repeated several times and at different rotational speeds, generally 1000 rpm, 3000 rpm and 6000 rpm. The readings of 5 to 8 sweeps were averaged and used for further data analysis. For average readings the current was interrupted and the iR-drop recorded. In some slurries, measurements were hindered by a severe gel problem in which case the electrode was repeatedly removed and cleaned. For each rotational speed the Ammeter was placed into the circuit and the plotter was connected to the Ammeter and the Voltmeter. The potential was then decreased from the potential corresponding to approximately 0.7 Amps at a rate of 0.12 Volts/min until the current was zero or negative. Between the potentials of zero and -0.6 Volts(SHE) the current originates entirely from the mass transfer controlled cerium reduction reaction and, consequently, an estimate of the current efficiency is obtained if effects such as mass transfer enhancement due to increased hydrogen gas evolution at higher electrode potentials are ignored.

Analysis of the iR-drop photographs was difficult. Generally, this technique is used

at much lower currents at which the switching action can be considered instantaneous. At the high currents of this project the switching time is of the order of 50 microseconds which is represented by the initial curved drop in potential. In addition, high frequency noise was observed in the capacitive decaying portion of the potential curve. Based on dummy circuits two different methods for finding the iR-drop were identified both of which are illustrated in Figure 4.7. These two methods were used interchangeably and often supplementary to each other in an attempt to produce fairly reliable results. Nevertheless, analysis of these photographs is still open to a great deal of personal interpretation. For this reason two sets of data were compared both of which were obtained in 1.6 molar sulfuric acid. One set was obtained prior to the runs in the cerium slurries and one set was obtained afterwards. The iR-corrected potential of both sets of data is plotted as a function of log(i) in Figure 4.8 where i is the current density in Amps/cm^2. Agreement between the potentials of the two runs is within ten percent, however, the presence of conceivable systematic errors should be kept in mind. The results are tabulated and plotted in Appendix C, Tables C.6-C.10.

The rotating wire electrode was also used in an empirical approach to obtain the effect of gas evolution on the conductivity (see Chapter 2, Equation 2.8). The distance between the rotating cathode and the Luggin capillary was varied and the Ohmic drop was determined as a function of the distance from the electrode using the current interrupter technique. Uncertainties in the current interrupter technique readings as well as other errors with respect to electrode positioning in an opaque cerium slurry, concentrations and current densities, made it impossible to measure the effect of the gas on the conductivity. As a result, the effect was ignored in the reactor model.

4.2 Apparatus of the Laboratory Electrochemical Cell

Figure 4.9 represents a flowsheet of the laboratory unit used to study the oxidation of cerium(III) in a differential area tube and wire cell. Figure 4.10 shows a photograph

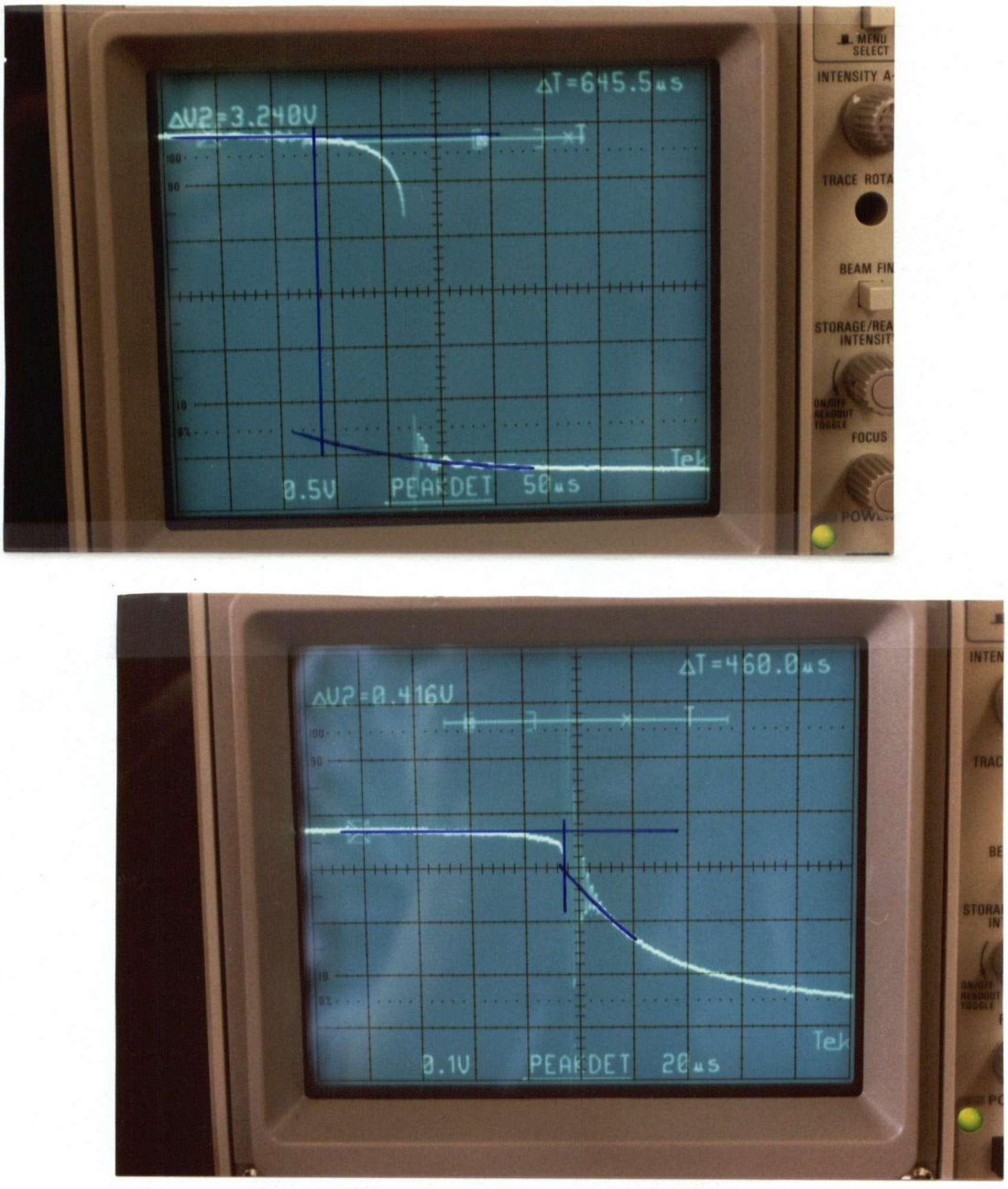

Figure 4.7: Methods for finding the iR-drop

	Top	*Bottom*
Potential	-3.64 Volts	-1.20 Volts(SCE)
Current	3.5 Amps	0.5 Amps
iR-drop	2.8 Volts	0.07 Volts
iR-corr.Pot.	-0.84 Volts	-1.13 Volts(SCE)

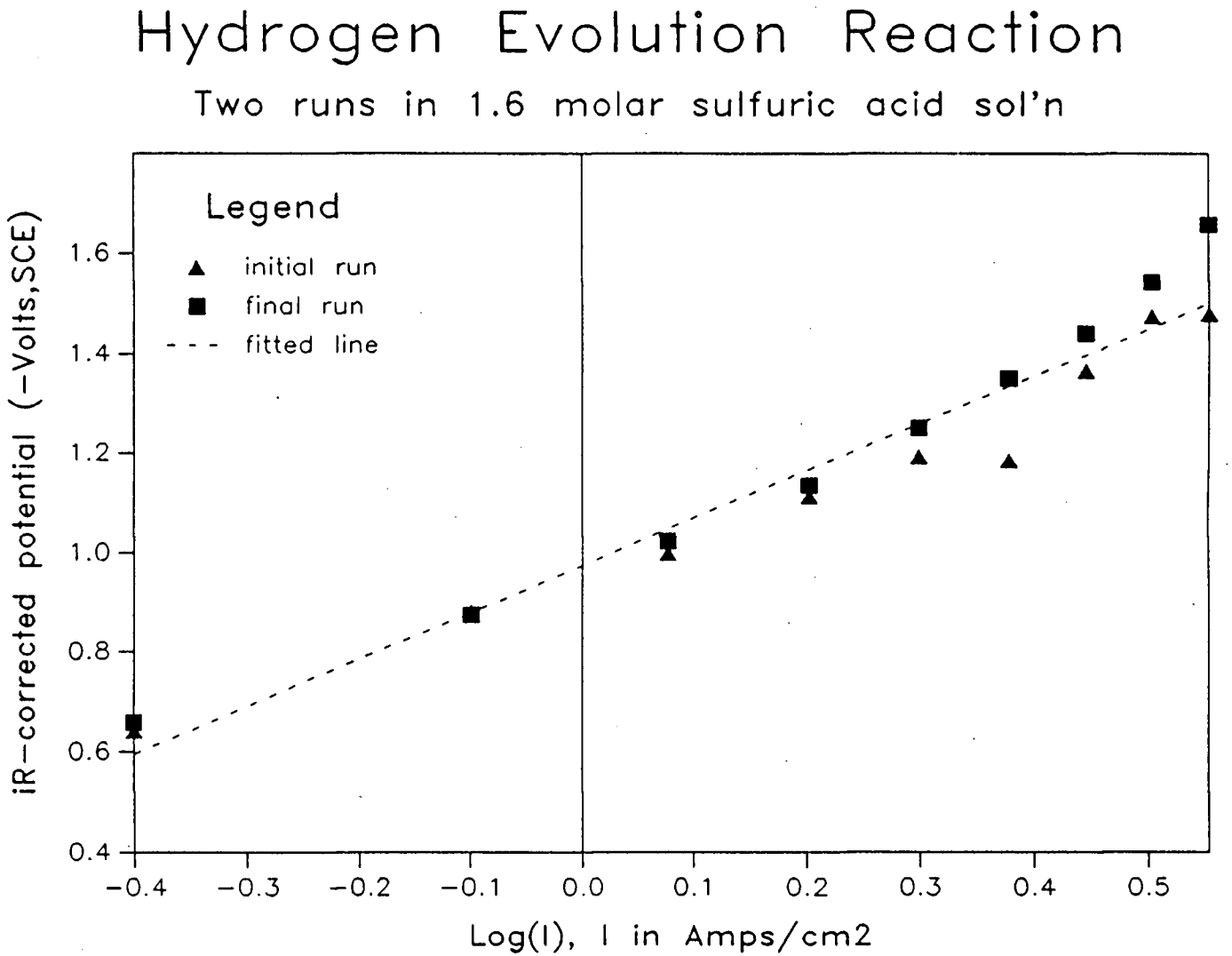

Figure 4.8: iR-corrected potential data for two runs in 1.6 molar sulfuric acid

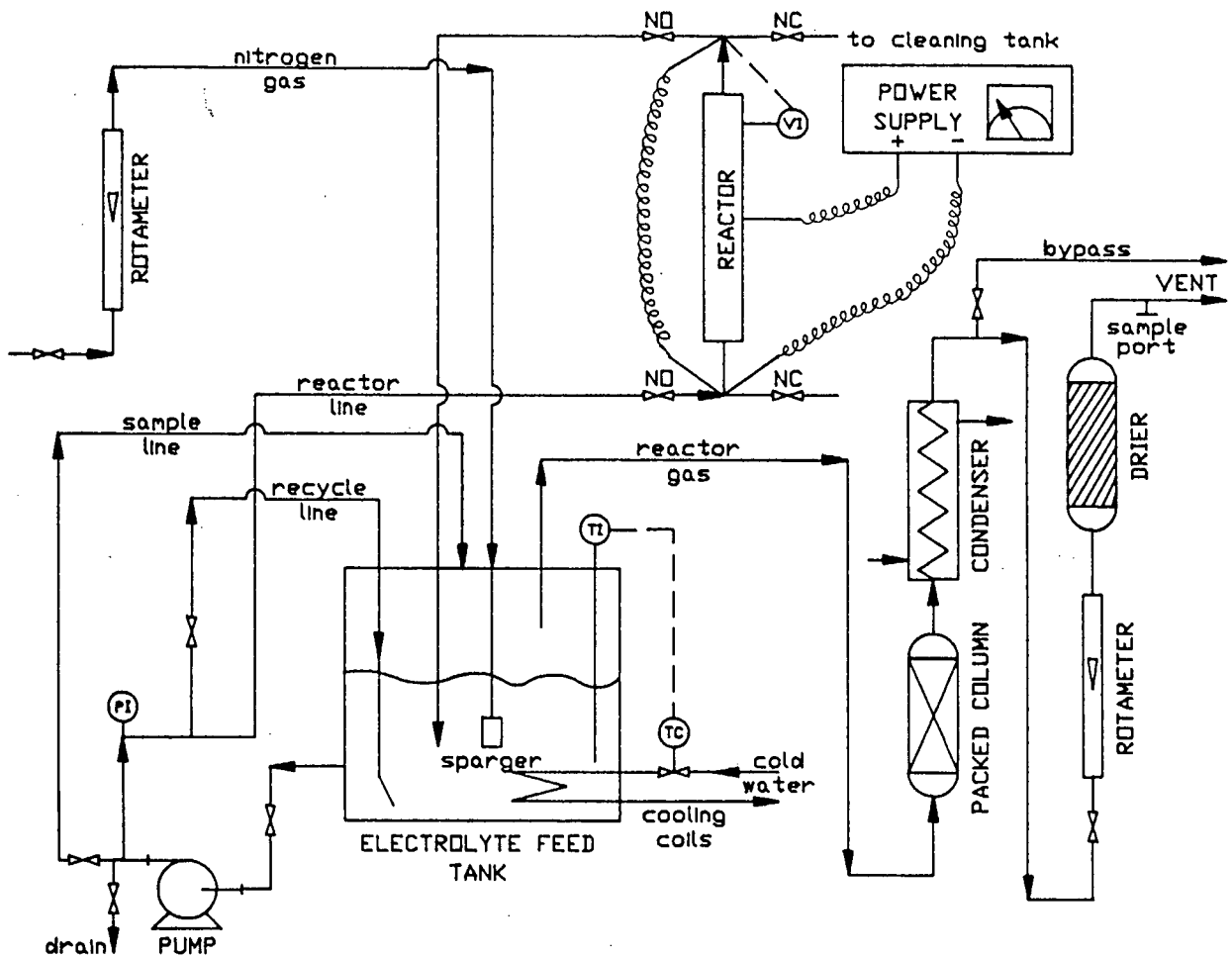

Figure 4.9: Apparatus of the laboratory electrochemical cell

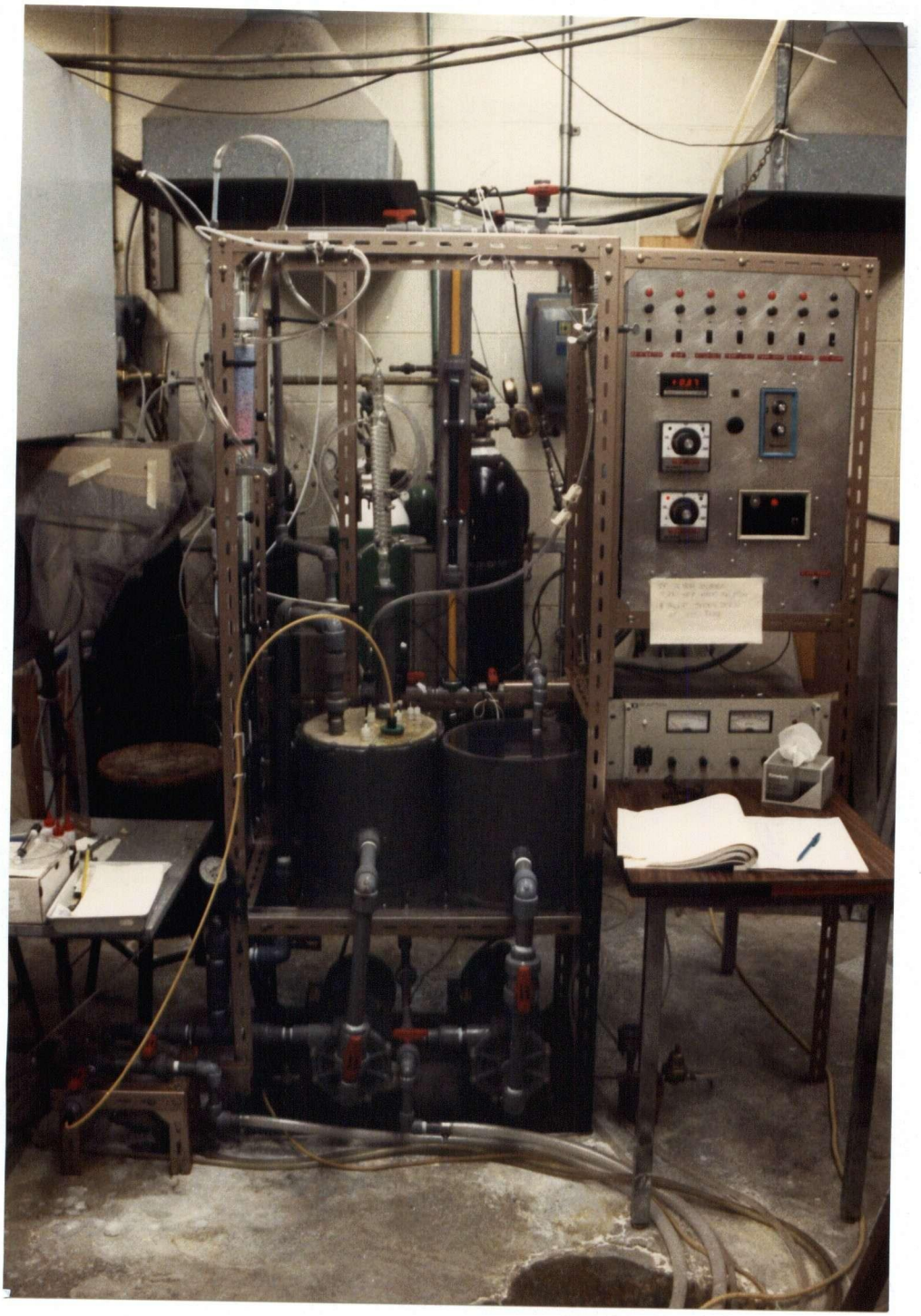

Figure 4.10: Photograph of the electrochemical cell

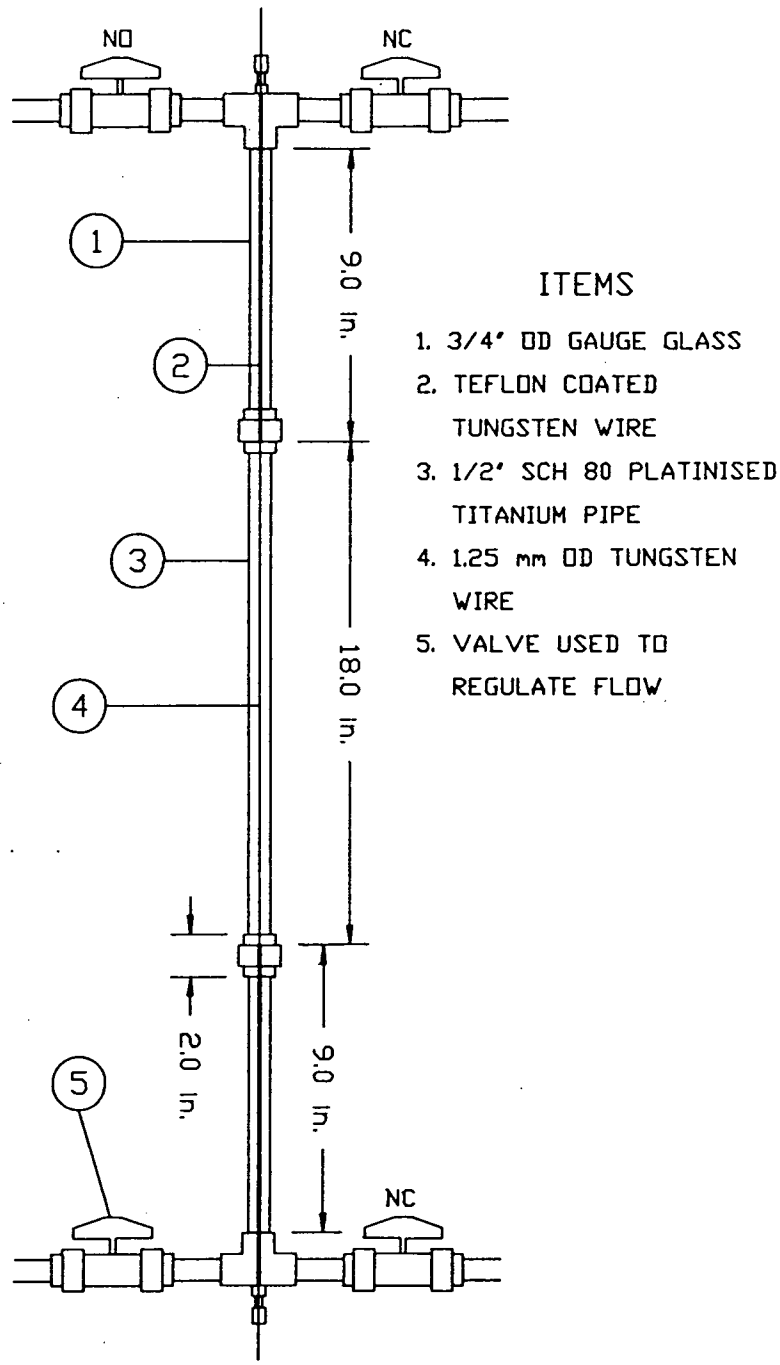

Figure 4.11: Construction of the cell

of the apparatus. The reactor itself is diagrammatically presented in Figure 4.11 and consists of a platinised titanium pipe as the anode with 4 microns of platinum along the inside, 18 inches in length and with a inside diameter of 1.387 cm. Through the center of this pipe runs a tungsten wire which is 1.25 mm in diameter and approximately one meter long. The active electrode portion of the wire is also 18 inches long as the ends outside the reactor pipe are covered with three to four layers of Teflon tape. The anode to cathode area ratio is, consequently, eleven to one. The reactor is fed from the bottom with the electrolyte which consists of a cerium sulfate slurry in H_2SO_4.

The electrolyte is pumped from a 20 litre tank. The electrolyte leaving the feed tank divides into three streams; one is recycled back to the feed tank using 1 inch piping, one is fed to the reactor using 1/2 inch piping, while a small third stream using 1/4 inch polypropylene tubing is used as a sample line and enters the tank through an easily removable stopper. The recycle stream enters the tank through a 45 degree elbow and maintains the slurry well-stirred. Since the process is run batchwise the reactor stream also returns to the feedtank. During the first two runs, nitrogen was added to the tank through a sparger and the gas flow was measured with a rotameter. However, the sparger was found to become plugged affecting the upstream pressure and rotameter reading. The reason for the nitrogen addition was to enable calibration of the hydrogen and oxygen flows from the reactor by sampling the gas mixture leaving the feed tank. From the kinetic study (see Table C.5, Appendix C) as well as from the first two runs, it was established that the cathode current efficiency with respect to the production of hydrogen was very high and could be approximated by 100 percent in most cases. As a result the nitrogen flow was eliminated from subsequent runs.

The pump was found to heat the electrolyte to well past 50 degrees Celsius. As a result cooling coils were installed inside the tank and a temperature controller with a thermocouple sensor regulated the temperature through a solenoid valve in the cooling coil line. Cold tap water was the cooling liquid.

The entrained gases separate from the liquid slurry in the feed tank upon which the gas is passed through a packed column, a spiral condenser, a gas flow rotameter and a drierite drying column. The now completely dry gas is sampled, analyzed and, subsequently vented.

Power for the reactor is supplied by a direct current power supply capable of supplying a DC current of 50 Amperes. In connecting the power supply to the reactor a third cable was run between the two cathode ends to obtain a more uniform current distribution.

Since gel formation had been a serious problem at times in the kinetic studies a cleaning tank was installed (not shown in Figure 4.9) which was to contain a sulfuric acid solution. With a separate pump this system would be able to clean the reactor without the need of its disassembly. As no significant gel problem was experienced this cleaning system was not used.

All parts in contact with the electrolyte are made of either polyvinylchloride, chloro-polyvinylchloride, polypropylene, glass or Teflon.

The specifications of the parts for this apparatus are given in Appendix A.

4.3 Procedure for Obtaining Data from the Laboratory Electrochemical Cell

First the nitrogen and the reactor gas rotameters were calibrated. The calibration curves are presented in Appendix B. The electrolyte flow was regulated manually by opening and closing the valve to the reactor. Two valve positions were used: fully open and half open. These positions were calibrated using distilled water. Even though the density is much greater when dealing with a slurry so is the viscosity. Data [3] obtained from BC research regarding densities and viscosities of cerium sulfate solutions indicated that the kinematic viscosity could be approximated by that of water. The fully open valve corresponds to a velocity of 2.8 m/s through the tube and wire reactor whereas the half open valve corresponds to 1.1 m/s.

The electrolyte slurry was prepared from a sulfuric acid solution through the addition

of cerous carbonate. The cerous carbonate reacts with the sulfuric acid to form cerous sulfate releasing carbon dioxide gas in the process:

$$Ce_2(CO_3)_3 + 3H_2SO_4 \Longrightarrow Ce_2(SO_4)_3 + 3H_2O + 3CO_2$$

The acid concentration was then adjusted to 1.6 molar and the electrolyte was left to equilibrate overnight. Throughout the preparation and equilibrium periods the electrolyte was circulated to prevent settling of the solids and plugging of the lines.

Experimentation consisted of a series of runs in which the current was set with the power supply. The electrolyte flow rate to the cell was determined by the position of the valve located at the bottom of the reactor and checked against the downstream pressure. An increase in the pressure gauge reading would be an indication of an obstruction within the pipes which would have an immediate effect on the flow velocity. Measurements involved current and cell potential values which were taken every 15 to 20 minutes as well as nitrogen and reactant gas flow rates. The temperature was kept constant at 50 degrees Celsius.

During a run, a liquid sample and two gas samples were taken at the end of each hour. The liquid sample was generally analyzed for total cerium concentration (including solids), dissolved cerium(III) concentration, and cerium(IV) concentration. The methods used to analyze for the above are listed in Appendix B [47]. The gas leaving the drying column was sampled through a tee with a gas tight syringe and analyzed for hydrogen, oxygen, and nitrogen using a gas chromatograph with a thermal conductivity detector. The carrier gas was Argon. The gas chromatograph used two columns in series; one containing molecular sieve followed by 2 meters of another column, 1/8 inch in diameter, containing Porapak N 80/100. The entire volume of the syringe, ten cubic centimeters, was injected.

The finish of a run was determined by either the cerium(IV) concentration or the current efficiency. Even though the objective was to obtain a final cerium(IV) concentration of 0.5 moles per liter, the current efficiency approached such low values in some cases

that the run was terminated at lower concentrations. At the end of the run the slurry was regenerated through the addition of 30 percent hydrogen peroxide which reduces cerium(IV) to form cerium(III) thereby releasing oxygen gas:

$$2Ce^{+4} + H_2O_2 \Longrightarrow 2Ce^{+3} + O_2 + 2H^+$$

The acid concentration was adjusted to 1.6 molar through the addition of concentrated sulfuric acid to account for the slight increase in volume. The slurry was, subsequently, left to equilibrate overnight. Since H_2O_2 is not stable at 50 degrees Celsius in turbulent solutions, any excess H_2O_2 had decomposed into water and oxygen gas by the next day. This was indicated by the slurry color which returned from a milky-white with a brownish tint to a milky-white with a yellowish tint. In addition, the open cell potential returned to 0.39 Volts, a value which was also observed in the original slurries to which no H_2O_2 had been addded.

A total of 8 runs was performed. The ranges of the operating variables covered in these studies are given in Table 4.1. Six out of the eight runs were conducted at a high liquid velocity (2.8 m/sec), giving a full factorial design with high (0.75-0.8 mol/l) and low (0.5-0.6 mol/l) total cerium concentrations and three levels of current density (18, 34, and 50 Amps total current). Two additional runs were performed at a low liquid velocity (1.1 m/sec) in order to obtain some measure of the effect of velocity. No runs were repeated under the same conditions. This appeared to be unfortunate as no estimate of the standard deviation between runs was now available. In addition, the two-effect and the three-effect interactions were of the same order of magnitude as the main effects and could, therefore, not be used as a measure of the standard deviation between runs.

Table 4.1: Ranges of the dependent and independent operating variables of the tube and wire reactor runs.

Variable	*Range*	*Accuracy*
Temperature	50 Celsius	5%
Pressure	1.5 atm	20%
Anode Current Density	0.09-0.25 A/cm^2	~5%
Cathode Current Density	1.0-2.8 A/cm^2	~5%
Cell Potential	2.8-5.2 Volts	$\pm$0.05 Volts
Reactor Flow Velocity	1.1-2.8 m/s	~20%
Reactor Volume	17.5-19.0 l	$\pm$0.5 l
Dissolved Cerous Sulfate	0.06-0.4 molar	$\pm$0.02 molar
Ceric Sulfate	0-0.5 molar	$\pm$0.02 molar
Total Cerium Sulfate	0.5-0.8 molar	$\pm$0.02 molar
Sulfuric Acid	1.6 molar	~5%
Current Efficiency from conc. analysis	0-100%	~10-20%
Current Efficiency from gas analysis	0-100%	~5%
Reactor Gas Composition		
H_2	20-100 molar %	$\pm$2-3 molar %
O_2	0-32 molar %	$\pm$1 molar %

Chapter 5

Results and Discussion

The aim of this project is to develop a satisfactory model based on kinetic studies which will predict current efficiencies as well as cell potentials of a laboratory electrochemical reactor and, subsequently of commercial cells. The chapter starts with a discussion of the dissolved cerium(III) concentration followed by a discussion of the kinetic data leading to the formation of a semi-empirical, semi-mechanistic model. The results of the model are compared to the actual results of the electrochemical reactor. The bad fit of this model resulted in the development of an entirely empirical model for the prediction of current efficiency. In conclusion, the fit, or lack of fit, of both models is discussed including posssible explanations for the observed behavior.

5.1 The Dissolved Cerium(III) Concentration

During the course of the kinetic experiments it became apparent that the solubility of cerous sulfate was not only a function of the ceric ion concentration, as had been assumed by BC Research. Instead, it also seemed to depend on the total cerium concentration, including the solids. Consequently, in the runs on the laboratory reactor the dissolved cerous sulfate concentration was also measured at the end of each hour in addition to the cerium(IV) and total cerium concentration. At high cerium(IV) concentrations the solubility of the cerous sulfate seemed to be limited by the total cerium concentration. For example, at a total cerium concentration of 0.75 molar and a cerium(IV) concentration of 0.5 molar, the dissolved cerium(III) concentration would typically be $\sim$0.25 molar. The solids that were still observed to be present at these concentrations consisted of less than

0.03 moles per litre, within the error of the analytical technique. From the data gathered in these runs a data subset was formed containing only those concentrations that did not seem to be limited by physical constraints such as the total cerium concentration. From this subset an empirical equation was derived relating the dissolved cerium(III) concentration to the cerium(IV) concentration and the total cerium concentration, including solids.

Analysis of balanced factorials of otherwise randomly chosen observations revealed that there was no apparent interactive effect between the ceric ion and the total cerium concentration whereas each had a definite main effect of comparible magnitude on the dissolved cerous sulfate concentration (see Appendix D, Sample Calculation Two). Consequently, a linear model seemed to give the best fit. Using a non-linear least squares method[1] the parameters and their uncertainties were determined resulting in the equation:

$$Ce^{+3}_{dissolved} = 0.08 + 0.36Ce^{+4} + 0.28Ce_{total} \tag{5.23}$$

with a standard deviation of 0.032 molar. This equation is valid for cerium(IV) concentrations between zero and 0.38 moles per liter and total cerium concentrations between 0.5 and 0.8 moles per liter. The predicted and actual dissolved cerous sulfate concentrations are included with the reactor results in Appendix C, Tables C.11-C.18.

An increase in the solubility of cerous sulfate with an increased ceric ion or sulfated ceric ion concentration might be the result of the interionic forces resulting from the increase in the total ion concentration in the slurry, even though no chemical reaction occurs. In other words, the activity coefficients in the solubility product(s) are not equal to unity and depend on the total ionic strength of the slurry. Another reason might be that an increase in the more strongly sulfated cerium(IV) concentration, predominantly $Ce(SO_4)_3^{-2}$, and a consequent decrease in the sulfate ion concentration pushes the equilibrium reaction to the right increasing the dissolved cerous sulfate concentration. In

[1] A statistical analysis system from SAS Institute Inc., North Carolina was used for all least squares fitting in this thesis. Generally, the non-linear Marquardt method was used.

acidic sulfuric acid solutions cerium(III) exists primarily as Ce^{+3} and $CeSO_4^+$. Dissociation of $Ce_2(SO_4)_3$ results, therefore, in an increased SO_4^{-2} concentration. If no $Ce(SO_4)_2^-$ is formed, the equilibrium reaction is

$$Ce_2(SO_4)_3 \rightleftharpoons nCe^{+3} + (2-n)CeSO_4^+ + (1+n)SO_4^{-2} \tag{5.24}$$

More difficult to explain is the effect of solids and the presence of solids at all times even when the total cerium concentration appears to impose a physical limitation on the dissolved cerous sulfate concentration. Solids are generally inert but, here, they are suggested to play an active role. They can only do so by either changing the ionic environment and, hence, activity coefficients or by changing the slurry sulfate concentration, thereby pushing the equilibrium reaction to the right. And they can only have the above effects if the actual nature of the solid changes either by reaction or by solvation.

At least five different hydrates have been found to occur at temperatures between 0 and 100 degrees Celsius ranging from dodecahydrate to tetrahydrate [2]. BC Research reported the observation of temporary supersaturation of electrolyte upon mixing of two electrolytes containing dissolved cerous sulfate obtained from different hydrated forms of solids. This suggests that the nature of the solid is definitely important, whereas the present study suggests that it may have a more permanent effect than was first thought. The extent of hydration may depend, for example, on the chemical environment in which the cerous sulfate was formed or on the process through which it was formed or even on the impurities present in the solution. In addition, temperature and the time of equilibration may have an effect. Finally, a mixture of hydrates may be present some of which may be more soluble than others. The latter may explain the presence of a small amount of solids at all times. If other ions, such as the sulfate ion, or other polar molecules show an affinity for the solid then the effect of the presence of solids is expected to increase as the amount of solids increases.

In all, it is uncertain how the solids or the total cerium concentration affects the dissolved cerous sulfate concentration. Some other interesting observations are given

below, all at 50 degrees Celsius.

- A 1.0 molar total cerium slurry in 1.6 molar sulfuric acid prepared from cerous carbonate and electrolyzed to 0.54 molar cerium(IV) was found to contain less than 0.03 molar solids and, consequently, 0.46 molar dissolved cerium(III) after an equilibration period of 24 hours. Ten days later, at room temperature, the concentrations were still the same.

- Ceric sulfate solutions in 2.2 to 2.5 molar sulfuric acid prepared from ammonium ceric nitrate and, subsequently, reduced with hydrogen peroxide to cerium(IV) concentrations varying from 0.8 to 0 molar behaved in the same way as the reactor slurries. When solids were present the cerous sulfate solubility was predicted very well by equation 5.23. The total cerium concentration varied from 0.6 to 0.82 molar.

- A very concentrated solution with a total cerium concentration of 1.37 molar was prepared in 1.6 molar sulfuric acid from ammonium ceric nitrate and a small amount of cerous carbonate. At a cerium(IV) concentration of 0.52 molar the dissolved cerium(III) concentration was found to be 0.85 molar, higher than expected from equation 5.23. Several days later, at room temperature, it was still at this high concentration.

5.2 Anode Kinetics on the Rotating Disc Electrode

It is believed that two reactions are taking place on the anode simultaneously. The primary reaction is the oxidation of cerous sulfate to form ceric sulfate which is mass transfer limited at increased potentials. The secondary reaction is the oxygen evolution reaction which is kinetically controlled:

$$Ce^{+3} \Longrightarrow Ce^{+4} + e^{-} \tag{5.25}$$

$$2H_2O \Longrightarrow O_2 + 4H^{+} + 4e^{-} \tag{5.26}$$

Since a rotating disc electrode was used in the experiment the limiting current was expected to increase with the square root of the rotational speed. The partial current density of the oxygen evolution reaction was assumed to be constant in any particular slurry. In addition, it was assumed that Stephan and Vogt's model regarding mass transfer enhancement due to gas evolution would hold [45]. In the absence of better data, the oxygen bubble diameter was taken to be 40 micrometers. The pressure was atmospheric and the temperature was 50 degrees Celsius. In addition, the kinematic viscosity was taken to be constant at 0.01 cm^2/s.

Since data was obtained at five different rotational speeds in each cerium sulfate solution, it was expected that a series of mathematical equations such as the Tafel equation for the oxygen evolution reaction, the mass transfer limited Tafel equation for the cerium oxidation reaction, the equation relating the limiting current density to the rotational speed (Equation 3.10) and Stephan and Vogt's model (Equation 2.2) could be solved to obtain the partial current densities as well as the diffusion coefficient and cerium(III) bulk concentration. Unfortunately, experimental error and nonideality prevented a converged solution.

Consequently, a different approach was needed. The oxygen evolution reaction is not present at potentials lower than 1.6 or 1.5 Volts SCE. Therefore, at lower potentials, the potentiometric curve represents the cerium oxidation reaction and these points were least squares fitted to the mass transfer limited Tafel equation:

$$V = a + b\log(i_{ce}) - b\log\frac{(i_{lim} - i_{ce})}{i_{lim}} \tag{5.27}$$

i_{ce} is the current density in $Amps/cm^2$.

i_{lim} is the limiting current density in $Amps/cm^2$.

b is the Tafel slope.

a is the Tafel intercept and includes the reversible potential.

V is the potential with respect to the standard calomel electrode in Volts.

The fitting parameters were a, b, and i_{lim}.

At the higher potentials the oxygen evolution reaction becomes increasingly important. The upper portion of the potentiometric curve is now least squares fitted to the above equation with the previously determined parameters as constants and the Tafel equation for the oxygen evolution reaction:

$$V = a + b\log(i_{O_2}) \tag{5.28}$$

where i_{O_2} is the partial current density of the oxygen evolution reaction in Amps/m^2. The fitting parameters are again b, the Tafel slope, and a, the Tafel intercept which includes the reversible potential.

In the above fitting procedure those data points for which the oxygen partial current density was less than 10 mAmps/cm^2 were ignored. In addition, the iR-drop seemed to become noticeable at the higher currents and as a result data points with currents greater than 250 mAmps/cm^2 were also ignored. Some personal judgement is involved in choosing the data intervals to be fitted which does affect the fitting parameters of the cerium oxidation reaction to a small extent($<$10%) and of the oxygen evolution reaction to a greater extent. The Tafel slope of the latter was affected by less than 10 percent, but the intercept could be affected by as much as 100 percent. In determining current efficiencies only the partial current density of the cerium reaction and the total current density is required and the uncertainty in the oxygen evolution reaction kinetics is not important. However, it does play a role in the determination of cell potentials. Other sources of error are experimental errors, noisy signals to the plotter (more so at the lower frequencies), and digitization errors. The curves were digitized using a Kurta Corporation graphics tablet connected to a personal computer. This method also leaves room for human error. The best fitting parameters are recorded in Appendix C, Figures C.21-C.32, with the experimental results.

In order to model the kinetic process, the limiting current density needs to be predicted from the rotational speed, the cerium(III) bulk concentration as well as possibly from the ceric sulfate concentration and the amount of solids. Equation 5.23, which relates the dissolved cerous sulfate concentration to the ceric sulfate and the total cerium concentration, was used in a variety of models including all of the above variables in linear and non-linear combinations. These models were least squares fitted to the limiting current density data and it was found that the ceric sulfate concentration and the amount of solids had a statistically insignificant effect on the limiting current. This doesn't necessarily mean that the solids had no effect on the mass transfer at the electrode.

Mass transfer at rotating disc electrodes in the presence of solids is a complicated process and involves the interaction of many parameters such as, among others, rotational speed, current density, size and nature of the electrode, size, nature, and size distribution of the particles, diffusing species and viscosity of the medium [15]. In the present studies, solids were observed to be present at all times and typically comprised about 7 to 10 percent of the total volume at low ceric sulfate concentrations, regardless of the total cerium concentration, and 1 to 3 percent of the total volume at high ceric sulfate concentrations. Consequently, the mere presence of the solids may have had an effect on the limiting current density but the effect was statistically not noticeable. Even though, generally, solids enhance mass transfer at the electrode, mass flux can also be decreased depending on the conditions. This, in some cases, can be attributed to an affinity of these solids to adhere to the electrode. Cerous sulfate is easily hydrated indicating that it must be a fairly polar molecule and that it could very well have an affinity to adhere to the electrode. An enhancement in mass transfer is illustrated by a slope greater than 0.5 of a plot of log(i) versus log(ω) where ω is the rotational speed. A slope smaller than 0.5 shows an inhibition in mass transfer.

The least squares fitted model that fitted the experimental data the best was

$$i_{lim} = 0.046\omega^{0.31}C_b^{0.69} \tag{5.29}$$

where ω is the rotational speed in rpm and C_b is the dissolved cerous sulfate concentration in mol/l. The standard deviation is 0.021 Amps/cm^2 which is about 20 percent of the average limiting current value. This may seem fairly large but no greater accuracy can be expected considering the assumptions and the experimental errors involved in obtaining the limiting current density data as well as the dissolved cerous sulfate concentration values. The latter was never actually measured in the kinetic studies, but found from equation 5.23.

Equation 5.29 indicates inhibited mass transfer. In addition, the reaction order seems to be less than one in Ce^{III}. Randle and Kuhn [38] found, in their work, that at Ce^{III} concentrations greater than 20 mmol/l the reaction order became less than one. They attributed this to the adsorption of an inactive Ce^{III} species, possibly $Ce(SO_4)_2^-$ and/or $Ce(SO_4)_3^{-3}$, on the electrode, thereby, decreasing the effective electrode area. They observed the oxidation reaction to be zero order in Ce^{IV}. Even though their solutions were much more dilute, the general observations are the same and the theory of the adsorption of either inactive anionic or polar cerous sulfate species seems to be supported.

In order to obtain an estimate of the diffusion coefficient the ideal case in which i_{lim} varies with the square root of the rotational speed and the reaction order is equal to one was also fitted to the data. The resulting best fit equation is:

$$i_{lim} = 0.0202\omega^{0.5}C_b \tag{5.30}$$

with a standard deviation of 0.026 Amps/cm^2. From the coefficient, 0.0202, the diffusion coefficient, D, was calculated to be $\sim 2 \times 10^{-6}$ cm^2/s. The value for $D_{Ce^{III}}$ obtained by Randle [38] is 5.2×10^{-6} cm^2/s at 25 degrees Celsius in 0.5 molar sulfuric acid and relatively dilute cerium solutions. Using the Stokes-Einstein equation and considering only the effects of temperature and viscosity, the diffusion coefficient in the slurries of this work should be about the same, since the increase in temperature is of the same

magnitude as the increase in viscosity, i.e.

$$\frac{D\mu}{T} = \text{constant} \tag{5.31}$$

where μ is the viscosity and T is the absolute temperature. However, this equation is applicable only in dilute solutions and its validity in slurries is debatable. Equation 5.29 is used for further modelling.

The slopes and the intercepts of the cerium oxidation and the oxygen evolution reaction were also modelled as functions of Ce^{IV} and Ce^{III} concentrations. Since the accuracy of the best fit equations wasn't much better than that of the average values, the latter were used for further modelling. The average values are:

Reaction		*Average*	*Stand.Dev.*
Ce oxidation	slope	0.36	0.04
Ce oxidation	intercept	1.7	0.2
O_2 evolution	slope	0.44	0.05
O_2 evolution	intercept	0.9	0.2

5.3 Cathode Kinetics on the Rotating Wire Electrode

The two simultaneously occurring reactions on the cathode are predominantly the evolution of hydrogen gas and, to a lesser extent, the reduction of Ce^{+4} to form Ce^{+3}.

$$2H^+ + 2e^- \Longrightarrow H_2 \tag{5.32}$$

$$Ce^{+4} + e^- \Longrightarrow Ce^{+3} \tag{5.33}$$

It is obvious from the results, which are illustrated in Figures 5.12 and 5.13, that the hydrogen evolution reaction is far from ideal as the Tafel equations are far from straight lines. As mentioned before in Chapter 2, Harrison found that the inhibiting effect of a hydrogen bubble layer results in a change of the Tafel slope, or the transfer coefficient [22]. In this study, the adsorption of cerium sulfate species is expected to play an even greater role affecting not only potential values but also cathode current efficiencies.

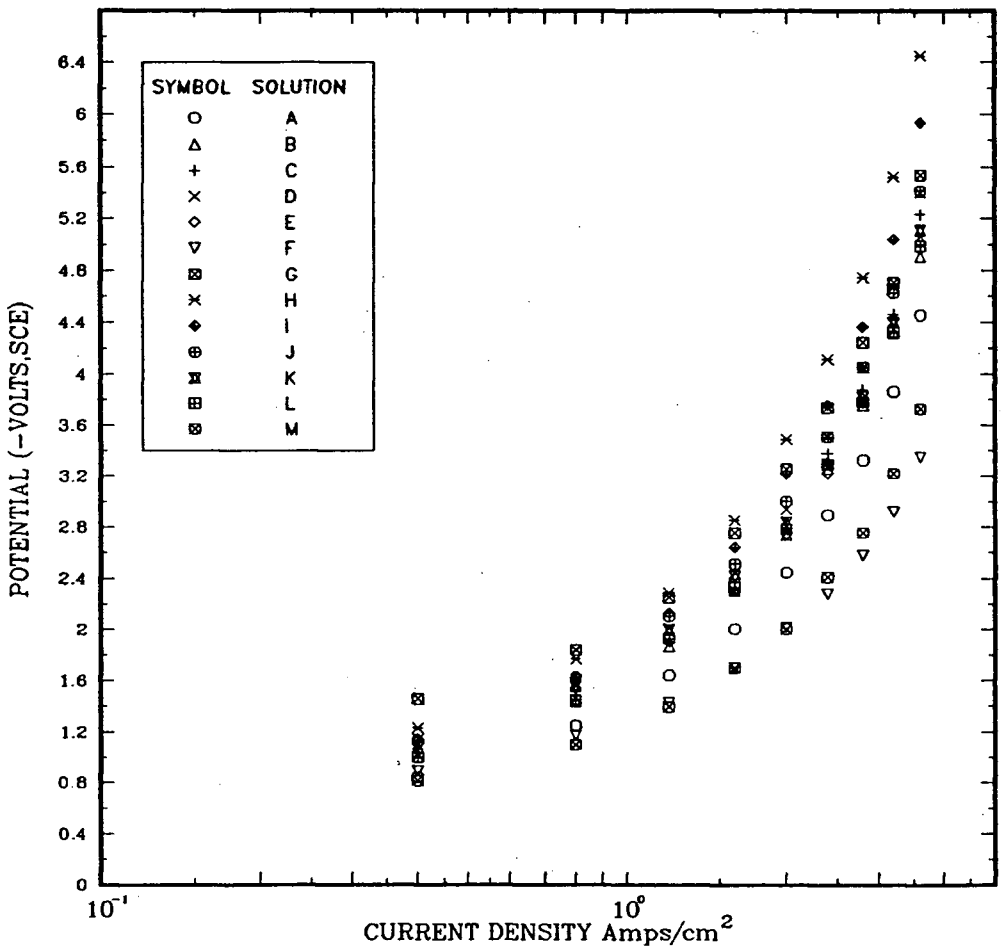

Figure 5.12: Potential versus total current density data from the rotating wire cathode

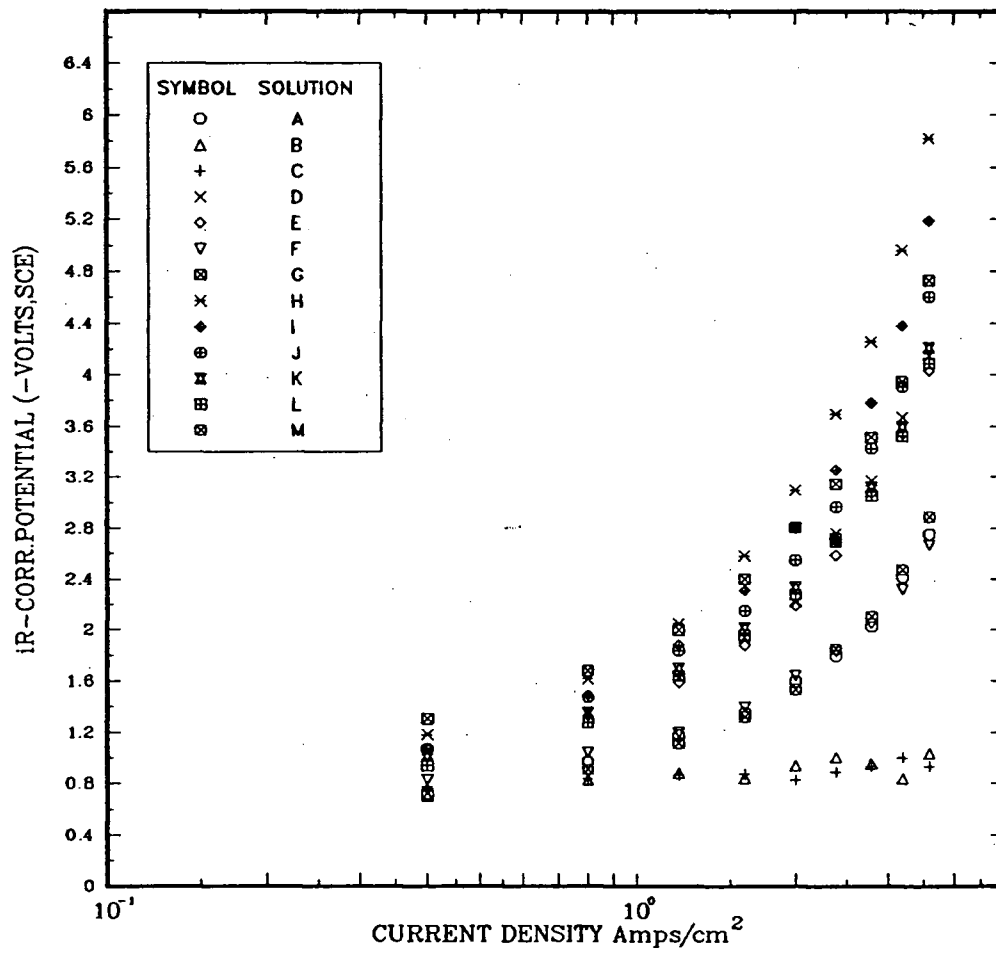

Figure 5.13: iR-corrected potential versus total current density data from the rotating wire cathode

As mentioned in the previous chapter, the extent of the secondary reaction, the cerium reduction reaction, was investigated at the lower potentials (see Table C.5, Appendix C). From these results it appears that even in the worst case of a low current density, 1 Amp/cm^2, and a high Ce^{IV} concentration, the electrode current efficiency for hydrogen is still greater than 94 percent. The presence of a mass transfer inhibiting coating is indicated by the insensitivity of the current density to rotational speed. Most of the data were obtained immediately after cleaning the electrode but in many cases the current density was much lower after a period of five to ten minutes.

These high electrode current efficiencies for hydrogen are also supported by the first two flow reactor runs in which the hydrogen gas could be determined from the constant nitrogen flow. Even though the flow rates are questionable for reasons mentioned earlier they did show a constant hydrogen production rate from the beginning to the end of the run. In the second run, for example, the standard deviation from the average was random and only six percent which is easily attributed to experimental error. In the remainder of the runs, the reactor gas flow was measured and seen to increase as current efficiency decreased, i.e. as the oxygen production rate increased. Finally, assuming a 100 percent cathode current efficiency for the gas analysis gave overall current efficiencies that were in very good agreement with the current efficiencies based on the concentration analysis (see Appendix C, Tables C.11-C.18).

High current efficiencies for hydrogen seem to suggest that the presence of an electrode coating overshadows any effect gas evolution may have on mass transfer. In addition, some type of adsorption seems to occur in all slurries and not only in those in which gel formation is observed.

No single satisfactory model could explain all potential-current data in the rotating wire experiments. Consequently, four different regions were identified based on the Ce^{IV} and dissolved Ce^{III} concentrations in mol/l.

Region	Ce^{IV}	Ce^{III}	*Model*
i	<0.15	<0.29	$V_c = -0.71 - 0.32i^{1.43}$
ii	<0.15	>0.29	$V_c = -0.87 - 0.8(Ce^{III})^{0.3}i^{1.34}$
iii	>0.15	<0.15	$V_c = -1.554(Ce^{IV})^{0.51}(Ce^{III})^{0.10}i^{0.11}$
iv	>0.15	>0.15	$V_c = -1.00 - 2.3(Ce^{IV})^{0.46}(Ce^{III})^{0.70}i^{1.40}$

where i is the cathode current density in Amps/cm^2 and V_c is the cathode potential with respect to the calomel reference electrode. The standard deviation of V_c in the above regions are 0.06, 0.056, 0.049, and 0.136 Volts respectively.

The above equations lead to the interesting observation that the potential is also dependent on the Ce^{III} concentration, especially, when this concentration is high. When both concentrations are low the potential is merely a function of current density. At low Ce^{IV} and high Ce^{III} the potential is a function of the current density as well as Ce^{III}. When both concentrations are high all three variables are important. Solutions A,F, and M belong to region (i), K and L to region (ii), B and C to region (iii), and solutions D, E, G, H, I, and J belong to region (iv).

In all slurries belonging to region (iv) gel formation was observed on the cathode whereas no indication of gel formation was found in any of the other slurries. This indicates that gel formation is promoted by high Ce^{III} and Ce^{IV} concentrations. The following consists of a series of hypotheses which attempt to explain the occurence of gel formation based on experimental observations.

In solutions with a low Ce^{III} concentration, <0.15 molar, the potential values as a function of the current are high but so is the iR-drop upon current interrruption resulting in fairly low iR-corrected potential values. Even though the Ce^{IV} concentration was high no gel formation was observed over the duration of the experiment. This might be explained by an accumulation of inactive sulfated cerium complexes in the Stern diffusion layer resulting in high potential values, mass transfer impedance, but low iR-corrected potentials as this layer disperses instantaneously upon current interruption. Inactive

complexes might be large in size and have a low charge density.

As the dissolved Ce^{III} concentration increases, the concentration of the Ce^{+3} ion also increases. Because of its small size and high positive charge density this ion is capable of adhering to the cathode and may even serve as a link between the cathode and the further removed sulfated cerium species. The iR-corrected potentials are now much higher as the double layer capacitance has increased due to a more permanent adsorbed layer.

As the Ce^{IV} concentration increases more $Ce(SO_4)_3^{-2}$ ions will approach the electrode through Ce^{+3} and react in an electron transfer step preceded or followed by a chemical reaction. Cerous sulfate complexes are formed which remain adhered to the electrode forming the so-called gel. The overall reaction might be

$$Ce^{+3} + Ce(SO_4)_3^{-2} + e^- \Longrightarrow Ce_2(SO_4)_3 \tag{5.34}$$

Gel formation is promoted by surface roughness, as indicated by the stratified appearance of the gel along the grooves of a rough tungsten wire and the noticeable decrease of gel formation on a smoothly etched tungsten surface. The reason for this might be that gas nucleation occurs more frequently at these locations enhancing local fluid circulation and, consequently, gel deposition by facilitating the transport of Ce^{IV} to the surface in the presence of Ce^{III}. An increase in local disturbances can also explain the increased rate of gel formation at the higher current densities. Even the effect of temperature is believed to be mainly kinetic as an increase in temperature increases the molecular kinetic energy near the metal surface and, consequently, promotes gel formation.

At high flow rates, the diffusion boundary layer near the electrode is very thin. The result is a lower concentration of sulfated complexes, which accumulate within the diffusion boundary layer, near the metal surface. Consequently, gel formation is much less. It still might occur but at a much lower rate.

A tungsten wire coated with a heavy layer of gel through electrolysis was rinsed lightly with distilled water upon which the gel was dissolved in sulfuric acid. The resulting

solution was found to contain only Ce^{III} and no Ce^{IV}. This result supports the above hypothesis that the gel consists of cerous sulfate complexes.

Since the cathode current density is very high and, thus, the amount of hydrogen produced is significant, it has been suggested that a high local pH may enhance or even initiate gel formation. The formation of such a pH gradient would be promoted by low velocities and high current densities. Consequently, a worst case scenario at the rotating wire electrode would be at a current density of 3000 mAmps/cm^2 and a rotational speed of 1000 rpm. The sulfuric acid bulk concentration was 1.6 molar. For these values, and ignoring the effect of hydrogen bubbles, the hydrogen ion concentration at the electrode surface was calculated to be 1.25 molar (see Sample Calculation 6, Appendix D). This indicates that the solution next to the electrode is still very acidic. Whereas the small increase in pH may contribute to gel formation, it is not expected to play a major role in gel initiation and formation.

5.4 Modelling

The results of the kinetic studies can now be integrated into a model for predicting cell potentials and cell current efficiencies in a laboratory size reactor. The algorithm of this model, which is referred to as 'the model', is listed in Appendix D and the results are tabulated in Appendix C with the experimental results in Tables C.11-C.18.

Unfortunately, the abililty of the model to predict the experimental data isn't very good. Throughout the first part of each run the predicted current efficiencies are generally much too low (see Figure 5.14). The effect of gas evolution on mass transfer had not been accounted for in the kinetic studies because of the presence of too many unknown variables such as the diffusion coefficient, bubble diameter and, last but not least, the effect of adsorption processes on gas evolution and vice versa. If assumptions are made regarding these parameters and if the nature and extent of adsorption processes in the flow reactor vary significantly from the kinetic studies, an enhancement in mass transfer

due to gas evolution on the anode might explain the much higher actual numbers. This increase can be as high as 50 percent at the lower velocities (see Sample Calculation 4, Appendix D). However, the difference is often greater than 50 percent and sometimes as high as 100-150 percent. In addition, the predicted current efficiencies are much too high at the end of the run which would be subjected to an even greater effect of gas evolution since more oxygen gas is evolved at the lower Ce^{III} concentrations.

An entirely mechanistic approach was attempted. The partial current densities were determined from the observed reactor current efficiencies. The modelling equations included Vogt's model and the Tafel equations for the cerium oxidation reaction and the oxygen evolution reaction. The parameters to be determined were the diffusion coefficient and two parameters which were combinations of the slopes and intercepts of the Tafel equation as a result of equation simplification. These equations were then least squares fitted to the data. The results of this approach weren't very satisfying either and are, therefore, not included in this thesis. The diffusion coefficient was again of the same order of magnitude, $2 - 5 \times 10^{-6}$ cm^2/s. The other parameters depended to a large extent on the weight given to the variables. If emphasis was placed on the first part of the run, this part was fitted better than the first model, however, the predicted current efficiencies for the last part would be much too high, worse than the first model. If emphasis was placed on the second part of the run, the opposite was observed.

The cell potentials as predicted by 'the model' and based on the kinetic data are generally higher than the actual potentials (see Figure 5.14). These differences are largest at the highest current density where they can be up to 50 percent higher. Also, the transition from one region of the model to the next is very noticeable in the modelled values whereas only subtle changes are noticed in the measured reactor potentials. There was also no indication of gel formation which would have led to higher potentials. This might be explained by the much higher velocities in the reactor as compared to the rotational speeds in the kinetic study. A velocity of 280cm/sec corresponds to approximately

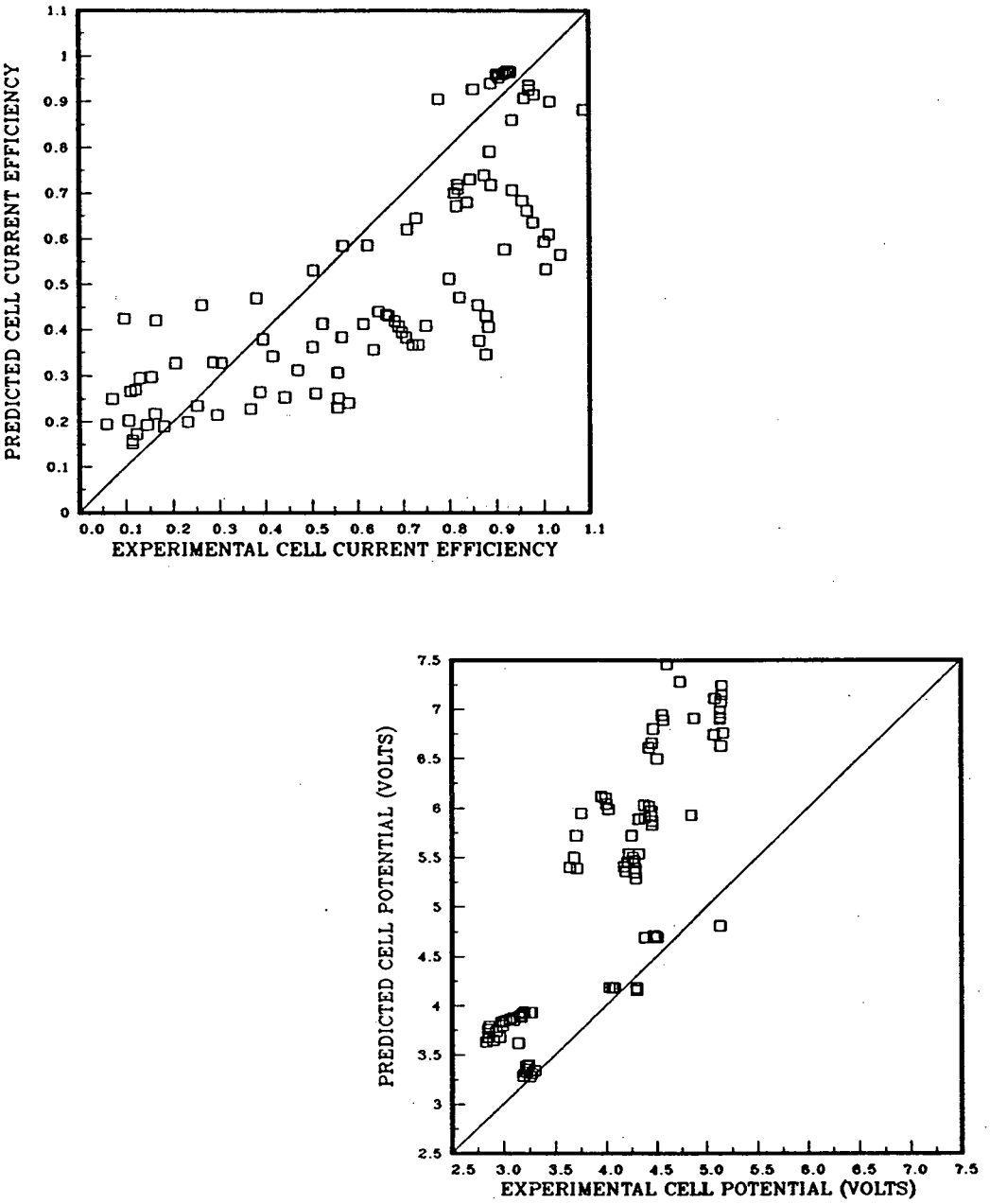

Figure 5.14: Predicted cell current efficiencies and cell potentials by 'the model' versus the experimental values obtained from the laboratory flow reactor.

17,500 rpm using the equation of Eisenberg, Tobias, and Wilke (see Sample Calculation 5, Appendix D). As was discussed in the previous section, gel formation is expected to be less at higher velocities.

The deviation between the modelled and predicted potentials may partially be attributed to the methods employed to determine the iR-drop. Equipment is available nowadays that can perform many iR-drop determinations by current interruption in a matter of milliseconds. The applied potential is then corrected by positive feedback during the course of obtaining electrochemical data. Human error, as well as systematic errors, might be introduced in the analysis of the oscilloscope photographs. In the case of a systematic error, the error is expected to increase with increasing current and increasing cell potentials.

Linear sweep voltammetry is a transient technique. Even at the low sweep rate employed in the kinetic studies (0.12 volts/min) the electrode processes may not have reached stability. The cell current efficiency is mostly determined by the anode current efficiency. If adsorption of cerous sulfate complexes onto the anode impedes the oxygen evolution reaction and if this adsorption process is slower than the scan rate, the current efficiencies determined from the kinetic experiments are expected to be lower than those measured in the tube and wire reactor. Chemical adsorption processes are often also a function of current density. At high current densities the adsorbed layer may form more quickly, whereas, at low current densities this layer may form only slowly and may have a more porous or denser nature. Finally, adsorption processes may depend on the concentration of the adsorbed or interfering species in the electrolyte slurry.

The major reason for the discrepancies between modelled and experimental cell current efficiencies and cell potentials is the presence of an unstable system.

At high ceric sulfate concentrations, negative ceric sulfate species, $Ce(SO_4)_3^{-2}$, are also attracted to the positive anode and may adsorb onto the electrode or shield it from the cerous sulfate complexes. The result might be a decrease in the effective surface area as

well as a reduction in the resistance to the oxygen evolution reaction and, consequently, a decrease in cell current efficiency. Again, the above may occur at a lower rate than the scan rate resulting in relatively higher predicted current efficiencies.

Adsorption in the form of a gel layer was observed on the cathode. The presence of a gel layer and, possibly, a packed diffusion boundary layer near the electrode surface leads to a very unstable system. Also, the kinetic experiments on the rotating wire were performed at lower equivalent velocities than those in the flow loop. This may have led to incomparable experiments as no gel formation was observed in the tube and wire cell. As a result, the derived concentration regimes may not apply in the flow loop and the experimental cell potentials are, generally, lower than the predicted cell potentials.

The only alternative seemed to be to empirically model the data from the tube and wire reactor runs. The effects of all the variables ignoring any interactions, could be determined qualitatively from the following least squares fitted linear equation:

$$CE = 0.49 + 0.0014Veloc + 1.8Ce^{III} - 1.1Ce^{IV} - 0.3Ce_{solids} - 1.6i_{total} \quad (5.35)$$

CE is the overall differential current efficiency for the production of Ce^{IV}.

$Veloc$ is the velocity of the reactor slurry in cm/s.

Ce^{III} and Ce^{IV} are the dissolved cerous and ceric sulfate concentrations in mol/l.

Ce_{solids} is the amount of cerium solids in mol/l obtained by subtracting Ce^{III} and Ce^{IV} from the total cerium concentration.

i_{total} is the total current density in Amps/cm^2.

The standard deviation is 0.11 in the current efficiency (see Figure 5.15).

From these parameters it is seen that the velocity and the cerous sulfate concentration have a positive effect on the current efficiency. The ceric sulfate concentration and the

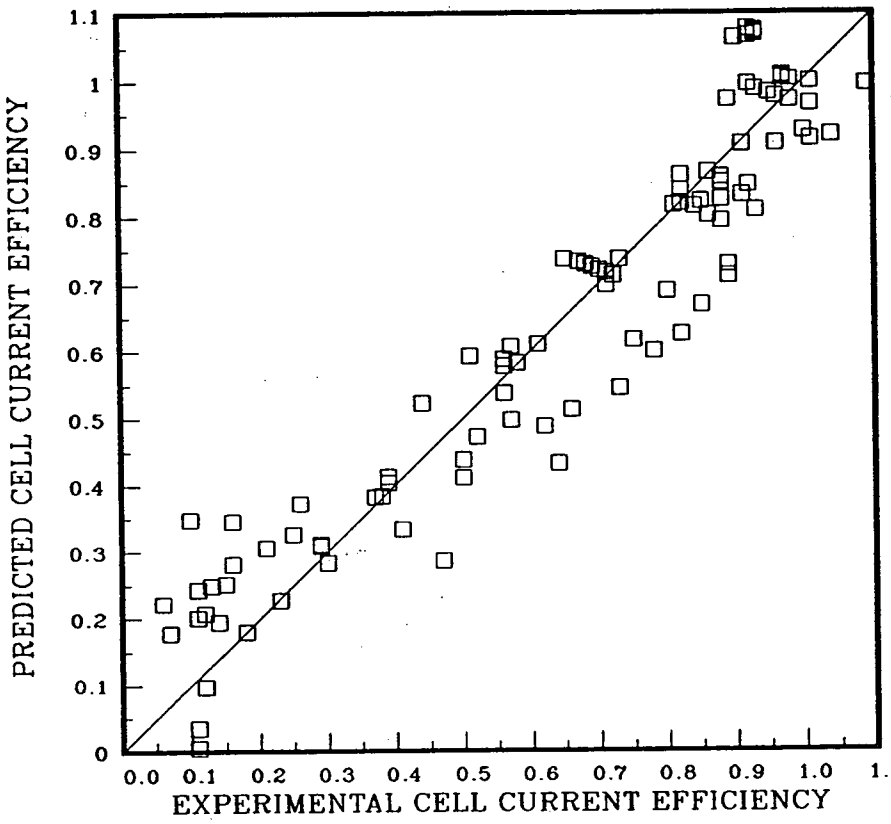

Figure 5.15: Predicted cell current efficiencies by the empirical model versus the experimental values obtained from the laboratory flow reactor.

current density have, as expected, a negative effect. Probably the most puzzling variable is the solids concentration which has, contrary to conventional standards, a negative effect on current efficiency. However, as pointed out previously in this chapter, cerium solids may not be inert. Experimental results indicate the presence of adsorption onto the electrodes, possibly of the solids.

The effect of velocity is illustrated by Figure 5.16. The other conditions for tube and wire reactor runs 5 and 6 are 34 Amps total current and a high total cerium concentration of 0.82 and 0.75 molar, respectively. Throughout the entire Ce^{IV} concentration range, the overall current efficiency for Ce^{IV} is ~30% higher in run 5 with a velocity of 2.8 m/sec as compared to run 6 at 1.1 m/sec. Runs 2 and 4 were conducted at 50 Amps total current and total cerium concentrations of 0.51 and 0.6 molar, respectively. The initial difference in current efficiency between the two runs is also ~30%. However, at increasing Ce^{IV} concentrations it is suspected that the effect of the decreasing dissolved cerous sulfate concentration becomes more important leading to a steeper decline in current efficiency in run 2.

Figure 5.17 shows the effect of the total cerium concentration of runs 2 and 8 on the current efficiency. Both runs were conducted at high velocities, 2.8 m/sec, and a high total current, 50 Amps. At low Ce^{IV} concentrations the measured current efficiencies are the same. As the Ce^{IV} concentration increases, the dissolved Ce^{III} concentration is soon limited by the total cerium concentration and the current efficiency drops sharply as is seen in run 2. Run 8 has a higher total cerium concentration and, consequently, the current efficiency does not drop significantly until much higher Ce^{IV} concentrations.

In Figure 5.18, the effect of current density on current efficiency is nicely illustrated by runs 1 and 2. The total cerium concentration is low with 0.52 molar for run 1, 0.51 molar for run 2, and 0.59 molar for run 3. In all three runs the flow velocity was ~2.8 m/sec. Run 2, with a total current of 50 Amps, has a consistently lower current efficiency than run 1, which had a total current of 18 Amperes. Even though the total current in

run 3 was 34 Amps, which is almost twice the current of run 1, the current efficiency values are approximately the same as those for run 1. One possible explanation might be that the slightly higher total cerium concentration of run 3 counteracts the effect of the higher current density.

In further statistical analysis, the inclusion of interaction effects raises doubts as to the statistical significance of an interaction. A factorial analysis of the effects and interaction effects of current density, ceric sulfate concentration, and total cerium concentration on current efficiency was not possible since the three-factor effect was of the same magnitude as the single effects. Consequently, no estimate of the error or standard deviation of current efficiencies between the runs was available. It, therefore, does not seem justifiable to continue modelling with the present data.

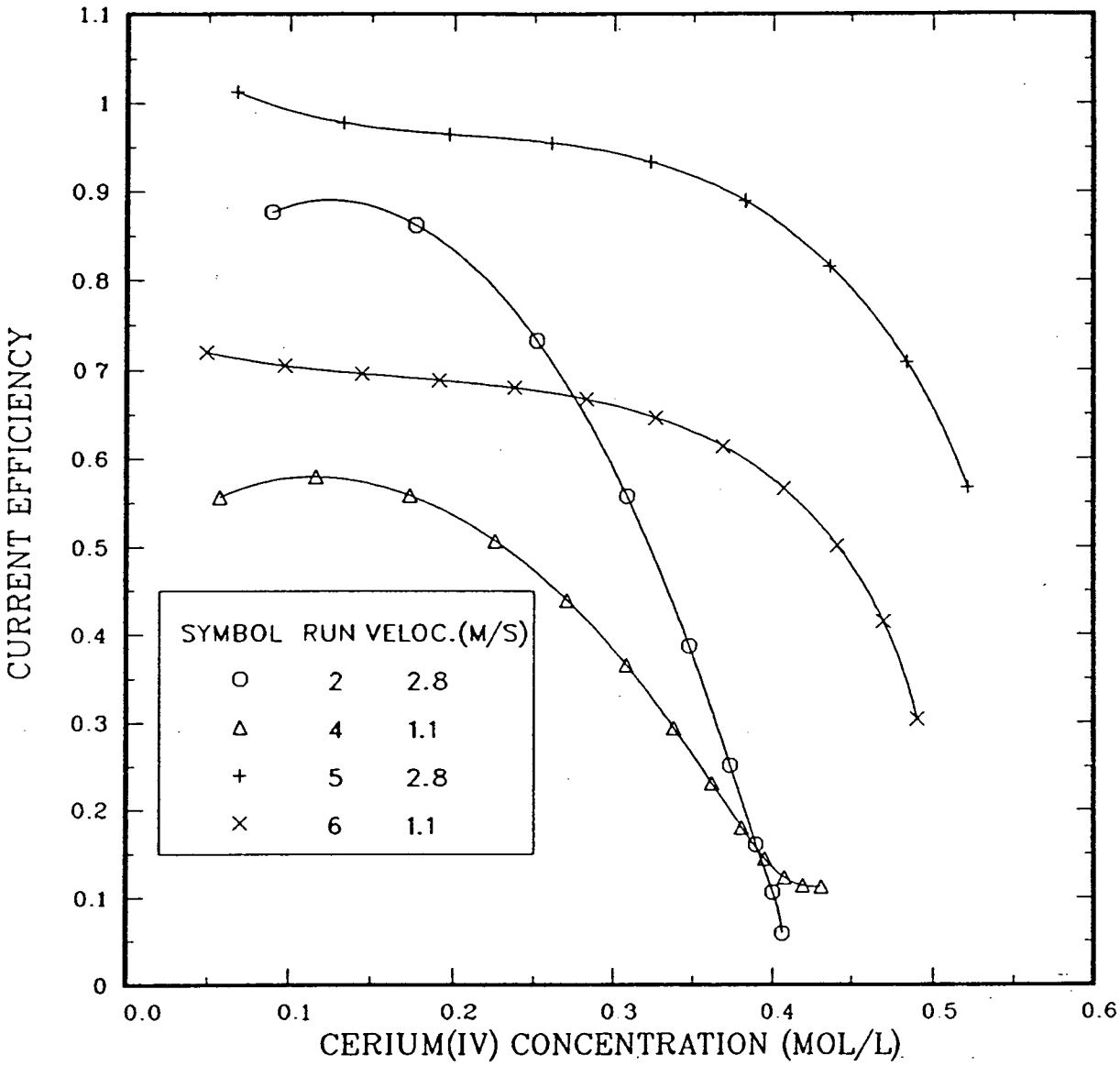

Figure 5.16: The effect of velocity on current efficiency

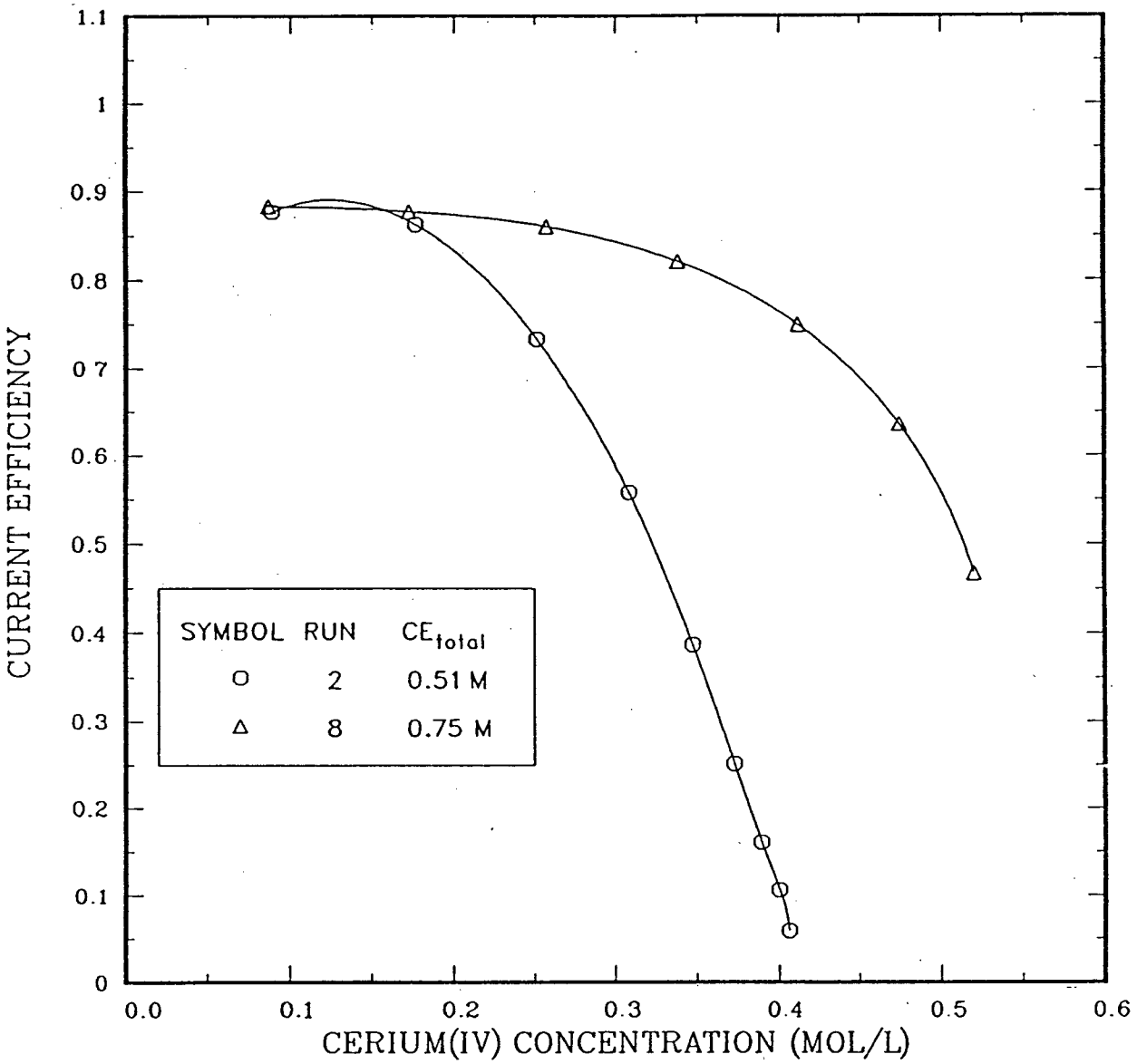

Figure 5.17: The effect of total cerium concentration on current efficiency

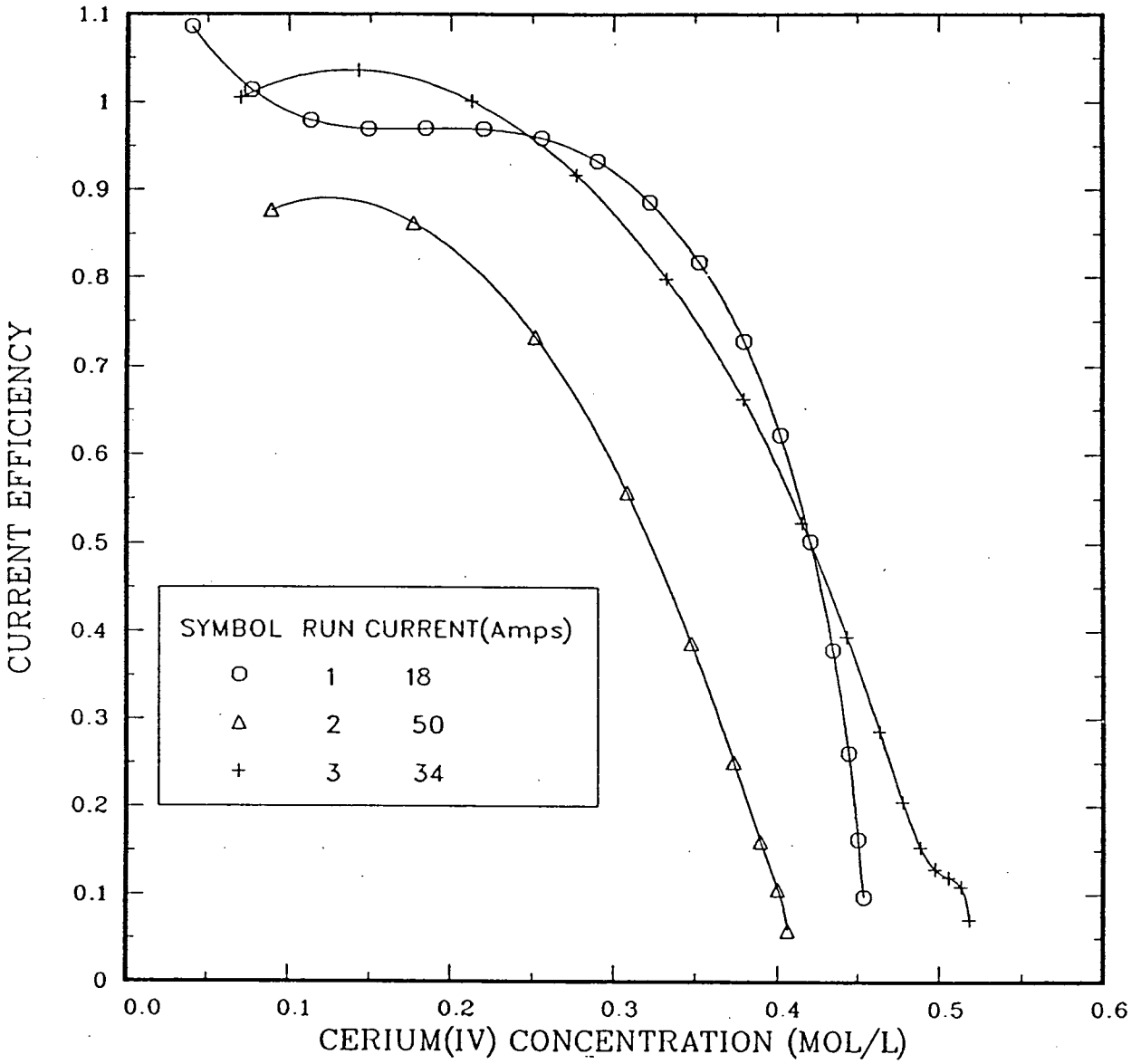

Figure 5.18: The effect of current density on current efficiency

Chapter 6

Conclusions, Recommendations

6.1 Conclusions

Ceric sulfate slurries were regenerated electrochemically from cerous sulfate slurries in sulfuric acid using a labsize tube and wire electrochemical cell. The cell consisted of a platinised titanium tube as the anode and a tungsten wire as the cathode. The reactor was run in a batchwise fashion.

Kinetic experiments at a rotating platinised titanium disc as the anode or a rotating tungsten wire as the cathode were conducted to obtain the electrode kinetics. Unfortunately, an entirely mathematical approach to obtain the electrode kinetics failed at both electrodes. In addition to significant experimental uncertainties, the presence of an unstable system through the presence of adsorption processes is expected to be the main reason for an equally unsatisfactory semi-empirical, semi-mechanistic reactor model. However, many worthwhile observations were made throughout the course of this thesis.

- The dissolved cerous sulfate concentration was found to be a function of the dissolved ceric sulfate concentration as well as the total cerium concentration. A linear relationship was developed for the conditions of the experimental runs.

- Both, the anode kinetic studies and the flow reactor runs, indicate an inhibition of mass transfer at the anode by the presence of solids. This may be attributed to an affinity of these solids to adhere to the electrode. Adsorption of inactive anionic or polar cerous sulfate species may be the reason for a reaction order in cerium(III) of less than one.

- The diffusion coefficient of cerium(III) near the rotating disc anode was determined to be of the order of $\sim 2 \times 10^{-6} cm^2/sec$.

- In the rotating wire cathode kinetic studies, adsorption of cerium sulfate species and subsequent gel formation is expected to have resulted in increased potential values but also in higher current efficiencies for the production of hydrogen and, subsequently, for the production of cerous sulfate. The presence of a mass transfer inhibiting coating led to very small partial current densities of the cerium reduction reaction. The electrode current efficiency for hydrogen was never observed to be lower than 94 percent. These high electrode current efficiencies for hydrogen were supported by the flow reactor runs.

- It is suspected that the transport of ceric sulfate anions to the cathode surface is facilitated by the much smaller Ce^{+3} ions. Subsequent chemical and electrochemical reactions are believed to result in a cerous sulfate gel formation. This process is promoted by high cerous and ceric sulfate concentrations, surface roughness, and low velocities.

An entirely empirical approach to the results of the flow reactor runs illustrated the effects of electrolyte velocity, the total cerium concentration, and superficial current density on the cell current efficiency in cerium(IV). Generally, an increase in reactant velocity and total cerium concentration and a decrease in the superficial anode current density gave an increase in the cell current efficiency in cerium(IV).

6.2 Recommendations

The following recommendations are suggested for future work in the regeneration of ceric sulfate:

- Kinetic studies should be performed on a small differential area flow reactor using a potentiostat that can handle the reactor currents and, preferably, one that corrects for the iR-drop continuously. AC impedance spectroscopy should be considered as it may indicate the presence and growth of gel layers.

- Kinetic studies should be performed continuously or at different time intervals to study and observe the effect of time.

- Experiments should be performed over a wider range of total cerium concentrations as it is suspected that high current efficiencies may be achieved at high total cerium concentrations even if the ceric sulfate concentration approaches 0.5 molar.

- A magnetic or sonic flow meter should be used to obtain accurate electrolyte velocities. A metering pump may work as well.

- The feasibility of running the process continuously, as opposed to batchwise, should be investigated.

Chapter 7

Nomenclature

A	electrode area
C_b	bulk concentration
C_s	surface concentration
C_{Os}	surface concentration of O
C_{Ob}	bulk concentration of O
C_{Rs}	surface concentration of R
C_{Rb}	bulk concentration of R
	where O and R refer to the redox reaction
	$O + ne^- \rightleftharpoons R$
Δc	concentration difference of dissolved gas
C_{dl}	double layer capacitance
D	diffusion coefficient
d	bubble departure diameter
d_{eq}	equivalent diameter
d_i	rotating electrode diameter
d_{wm}	distance between the working electrode and the
	counter or reference electrode
F	Faraday constant
f_g	efficiency of gas evolution
f	void fraction of gas

f_o	gas void fraction at the electrode surface
f_b	gas void fraction in the bulk electrolyte
g	acceleration due to gravity
i_o	exchange current density
i_f	current density of formation of dissolved gas
i_t	total current density
i_{lim}	limiting current density
i_k	kinetic current density
K	equilibrium constant, or otherwise defined constant
K_m	dimensionless conductivity $= \kappa_e/\kappa$
k	overall mass transfer coefficient
k_{mc}	macroconvective mass transfer coefficient
k_c	microconvective mass transfer coefficient
k_{rxn}	rate constant
n	charge number of the electrode reaction
p^*	supersaturation ratio i.e. the supersaturation level/saturation level
P	pressure
R	gas constant
R_Ω	Ohmic resistance
R_{ct}	charge transfer resistance
S	rotational speed, rpm
T	temperature (K)
v	velocity
V_G	volumetric flow rate of evolved gas

Re	Reynolds number, $= \frac{d_{eq}v}{\nu}$
Sc	Schmidt number, $= \frac{\nu}{D}$
Sh	Sherwood number, $= \frac{k_{mc}d_{eq}}{D}$
α	transfer coefficient
δ	diffusion layer thickness
ν_D	stoichiometric number (refers to reaction product)
ν	kinematic viscosity
κ_e	conductivity of electrolyte with gas present
κ	conductivity of pure electrolyte
η	overpotential
η_c	concentration overpotential
σ	Warburg coefficient
Θ	fractional surface coverage
ω	frequency
μ	ionic strength, reaction order in R.D.E.

Bibliography

[1] Bard, A. J., and L. Faulkner. Electrochemical Methods. New York: John Wiley, 1980.

[2] B.C. Research. Manufacture of Naphthoquinone, tetrahydroanthtraquinone, and anthraquinone. Reports prepared for B.C. Science Council, 1981-1983.

[3] B.C. Research. THAQ and NQ design engineering handbook. 1985.

[4] Bendrich, G., W. Seiler, and H. Vogt. "Experimental investigation of combined mass transfer at gas-evolving electrodes with superposition of electrolyte flow." International Journal of Heat and Mass Transfer 29 (11, 1986): 1741-1745.

[5] Biegler, T., R. Woods. "Limiting oxygen coverage on smooth platinum anodes in acid solution." Journal of Electroanalytical Chemistry and Interfacial Electrochemistry 20 (1969): 73-78.

[6] Biegler, T., D. A. J. Tand, and R. Woods. "Limiting oxygen coverage on platinized platinum; relevance to determination of real platinum area by hydrogen adsorption." Journal of Electroanalytical Chemistry and Interfacial Electrochemistry 29 (1971): 269-277.

[7] Bird, R. B., W. E. Stewart, and E. N. Lightfoot. Transport Phenomena. New York: John Wiley, 1960.

[8] Blatz, L. A. "The use of a cation-exchange resin to study the cerous and sulfate ion complexes." Journal of Physical Chemistry 66 (1962): 160-164.

[9] Bongenaar-Schlenter, B. E., L. J. J. Janssen, S. J. D. Van Stralen, and E. Barendrecht. Journal of Applied Electrochemistry 15 (1982):329-337.

[10] Britz, D., and W. A. Brocke. "Elimination of iR-drop in electrochemical cells by the use of a current-interruption potentiostat." Electroanalytical Chemistry 58 (1975): 301-311.

[11] Butler, J. N. Ionic Equilibrium a mathematical approach. New York: Addison-Wesley Publishing Company, 1964.

[12] Cotton, F. A., and G. Wilkinson. Advanced Inorganic Chemistry. New York: John Wiley, 1980.

[13] Dees, D. W., and D. W. Tobias. "Mass transfer at gas evolving surfaces." Journal of the Electrochemical Society 134 (7, 1987): 1702-1713.

[14] Eisenberg, M., D. W. Tobias, and C. R. Wilke. "Ionic mass transfer and concentration polarization at rotating electrodes." Journal of the Electrochemical Society 101 (6, 1954): 306-319.

[15] de Ficquelmont-Loizos, M. M., L. Tamisier, and A. Caprani. "Mass transfer in laminar flow at a rotating disk electrode in suspensions of inert particles." Journal of the Electrochemical Society 135 (3, 1987): 626-634.

[16] Filinovsky, V. Yu., and Yu. V. Plevskov. "Rotating disk and ring-disk electrodes in investigations of surface phenomena at the metal-electrolyte interface." Progress in Surface and Membrane Science 10 (1976): 27-116.

[17] Hanna, S. B. "Planning a kinetic and mechanistic study with cerium(IV)." Journal of Chemical Education 53 (8, 1976): 524-527.

[18] Hardwick, T. J., and E. Robertson. "Association of ceric ions with sulphate [a spectral study]." Canadian Journal of Chemistry 29 (1951): 828-837.

[19] Harrison, J. A. "Automation of electrode kinetic measurements - 7." Electrochimica Acta 27 (8, 1982): 1113-1122.

[20] Harrison, J. A., and A. T. Kuhn. "The role of gas bubble formation in the electrocatalysis of the hydrogen evolution reaction." Surface Technology 19 (1983): 249-259.

[21] Harrison, J. A. "A note on the use of the impedance to investigate parallel redox reactions and indicator redox reactions during gas evolution." Electrochimica Acta 29 (6, 1984): 703-709.

[22] Harrison, J. A., and A. T. Kuhn. "The effect of bubbles on the measured electrochemical parameters during hydrogen evolution on nickel." Journal of Electroanalytical Chemistry and Interfacial Electrochemistry 184 (1985): 347-356.

[23] Hayes, M., and A. T. Kuhn. "Techniques for the determination of ohmic drop in half-cells and full cells: a review." Journal of Power Sources 2 (1977/78): 121-136.

[24] Hubbard, D. W., and E. N. Lightfoot. "Correlation of heat and mass transfer data for high Schmidt and Reynolds numbers." Industrial & Engineering Chemistry Fundamentals 5 (3, 1966): 370-379.

[25] Janssen, L. J. J., and J. G. Hoogland. "The effect of electrolytically evolved gas bubbles on the thickness of the diffusion layer - II." Electrochimica Acta 18 (1973): 543-550.

[26] Janssen, L. J. J. "Mass transfer at gas evolving electrodes." Electrochimica Acta 23 (1978): 81-86.

[27] Janssen, L. J. J., and E. Barendrecht. "The effect of electrolytic gas evolution on mass transfer at electrodes." Electrochimica Acta 24 (1979): 693-699.

[28] Janssen, L. J. J., and E. Barendrecht. "Mass transfer at gas evolving electrodes." Journal of Applied Electrochemistry 15 (1985): 549-555.

[29] Krause, B., and H. Vogt. "Effect of operational parameters on gas evolution in electrolyte bulk: possibilities for lowering interelectrode resistance." Journal of Applied Electrochemistry 15 (1985): 509-515.

[30] Kuhn, A. T., and M. Stevenson. "Over-potential measurement at gas-evolving electrodes." Electrochimica Acta 27 (3, 1982): 329-337.

[31] Kuhn, A. T., and T. H. Randle. "Effect of oxide thickness on the rates of some redox reactions on a platinum electrode." Journal of the Chemical Society - Faraday Transactions I 81 (1985): 403-419.

[32] Landolt, D., R. Acota, R. H. Muller, and C. W. Tobias. "An optical study of cathodic hydrogen evolution in high-rate electrolysis." Journal of the Electrochemical Society 117 (6, 1970): 839-845.

[33] Mantell, C. L. Electrochemical Engineering. New York: McGraw-Hill, 1960.

[34] Newman, J. Electroanalytical Chemistry 6 (1973).

[35] Newton, T. W., and G. M. Archand. "A spectrophotometric study of the complex formed between cerous and sulfate ions." Journal of the American Chemical Society 75 (May, 1953): 2449-2453.

[36] Oehr, K. H. Process for preparing ceric sulphate. May 1, 1984. Canadian Patent 1,166,600.

[37] Pleskov, Yu. V., and V. Yu. Filinovsky. The Rotating Disc Electrode. New York: Consultants Bureau, 1976.

[38] Randle, T. H., and A. T. Kuhn. "Kinetics and mechanism of the cerium(IV)/cerium(III) redox reaction on a platinum electrode." Journal of the Chemical Society - Faraday Transactions I 79 (1983): 1741-1756.

[39] Randle, T. H., and A. T. Kuhn. "The influence of platinum (phase) oxide on the electrode kinetics of the manganese(III)/manganese(II) and cerium(IV)/cerium(III) redox couples in sulfuric acid." Electrochimica Acta 31 (7, 1986): 739-744.

[40] Roald, B., and W. Beck. "The dissolution of magnesium in hydrochloric acid." Journal of the Electrochemical Society 98 (7, 1951): 277-290.

[41] Schlichting, H. Boundary-Layer Theory. New York: John Wiley, 1960.

[42] Shibata, S. "The concentration of molecular hydrogen on the platinum cathode." Bulletin of the Chemical Society of Japan 36 (1, 1963): 53-57.

[43] Sides, P. J., and C. W. Tobias. "Primary potential and current distribution around a bubble on an electrode." Journal of the Electrochemical Society 127 (2,1980): 288-291.

[44] Sides, P. J., and C. W. Tobias. "Resistance of a planar array of spheres: gas bubbles on an electrode." Journal of the Electrochemical Society 129 (12, 1982): 2715-2720.

[45] Stephan, K., and H. Vogt. "A model for correlating mass transfer data at gas evolving electrodes." Electrochimica Acta 24 (1979): 11-18.

[46] Tenn, T. I. "Anthraquinone pulping of wood." Chemical Engineering 86 (Dec 3, 1979): 64-65.

[47] Vogel, A. I. Textbook of Quantitative Inorganic Analysis. New York: Longman Inc., 1978.

[48] Vogt, H. "Mass transfer at gas evolving electrodes with superposition of hydrodynamic flow." Electrochimica Acta 23 (1978): 203-205.

[49] Vogt, H. "On the supersaturation of gas in the concentration boundary layer of gas evolving electrodes." Electrochimica Acta 25 (1980): 527-531.

[50] Vogt, H. "The rate of hydrogen generation in the electrodeposition of metal powder at gas-evolving electrodes." Surface Technology 17 (1982): 301-307.

[51] Vogt, H. "Gas evolving electrodes." Comprehensive Treatise of Electrochemistry 6 (1983): 445-489.

[52] Vogt, H. "The rate of gas evolution at electrodes - I. An estimate of the efficiency of gas evolution from the supersaturation of electrolytes." Electrochimica Acta 29 (2, 1984): 167-173.

[53] Vogt, H. "The rate of gas evolution at electrodes - II. An estimate of the efficiency of gas evolution on the basis of bubble growth data." Electrochimica Acta 29 (2, 1984): 175-180.

[54] Vogt, H. "Studies on gas-evolving electrodes: the concentration of dissolved gas in electrolyte bulk." Electrochimica Acta 30 (2, 1985): 265-270.

[55] Vogt, H. "Superposition of microconvective and macroconvective mass transfer at gas-evolving electrodes - a theoretical attempt." Electrochimica Acta 32 (4, 1987): 633-636.

Appendix A

Ancillary Equipment

1. Kinetic Studies

1. Ammeter

   Princeton Applied Research Digital Coulometer, Model 379.

2. Camera

   Asahi Pentax Spotmatic

3. Function Generator

   Interstate 20 MHz Log-Linear Sweep Generator, Model F77

4. Oscilloscope

   Tektronix Digital Storage Oscilloscope, Model 2230

5. Plotter

   Watanabe XY Recorder WX446

6. Power Supply

   Sorensen DC Power Supply DCR40-10A

7. Rotator

   Pine Instrument Company analytical rotator, Model A6R2, Serial 118, speed controller range 0-10000 rpm

8. Stirrer

   Corning Hot Plate Stirrer, PC-351

9. Switch

   Midtex Mercury Wetted Contact Relay 160-151R00

10. Temperature Controller Unit

Thermo Electric Temperature Controller with an Omega digital display temperature indicator

11. Thermocouple

    Omega Iron Constantan thermocouple, PFA coated, 1/8 inch diameter probe

12. Reference Electrode

    Saturated Calomel Electrode, Schott Mainz, Jena glass

13. Voltmeter

    Dana Digital Multimeter 4600

2. Laboratory Reactor

1. Condenser

   Graham Spiral Condenser, Jacket length 400mm, $\bar{\$}$24/40 Joint Size

2. Cooling Coils

   8ft of 3/8 inch teflon tubing mounted inside the feed tank by teflon spacers

3. Drier

   Drierite Gas Drying Unit, 66mm in diameter, 289mm in heigth, filled with $\sim$ 0.57kg of 8 mesh indicating Drierite

4. Feed Tank

   20 litre CPVC tank, 11.75 inch OD, 12.5 inch in heigth, wall thickness 3/8 inch

5. Feed Tank Lid

   clear PVC, thickness 3/16 inch

6. Gas Analysis Equipment

   - Model 6000 Vista Gas Chromatograph
   - Vista 401 Chromatography Data System
   - Varian Remote Plotter/Printer

7. Gas Dispersion Tube

   Pyrex fritted cylinder, coarse porosity, 250mm in length, 12mm OD

8. Gauge Guard

   Plast-O-Matic PVC gauge guard

9. Hi-Lo Voltage Alarm

   Telmar AC operated alarm, Model 543

10. Packed Column

    10 inches of 1.5 inch CPVC pipe filled with 1/4 inch berl saddles which are supported by a teflon grid

11. Piping and Fittings

1/2 inch and 1 inch CPVC

12. Power Supply

    Hewlett Packard DC Power Supply 6261B, 0-20 Volts, 0-50 Amps

13. Pressure Gauge

    Marsh gauge, pressure range 0-30 psig

14. Pumps

    Flotec C5P8-1164SV CPVC End Suction Centrifugal Pump, 1/3 Hp, 3.75 inch impeller

15. Reagents

    - 99.5% Cerous Carbonate supplied by Rhone-Poulenc of Freeport, Texas, Molecular Weight $\sim$ 275 g/mol
    - sulfuric acid, BDH Ltd. , concentrated
    - hydrogen peroxide, BDH Ltd. , 30%
    - distilled water

16. Rotameters

    - Nitrogen, Cole-Parmer, 65mm flowtube, SS float, max. air flow rate 3942ml/min STP
    - Reactor gas, Cole-Parmer, 65mm flowtube, glass float, max. air flow rate 1350 ml/min STP

17. Syringes

    Pressure-Lok Gas Syringes, series A, 10ml capacity

18. Temperature Controllers

    Omega Analog Indicating Temperature Controllers, model 1922, range 0-300 degrees Celsius, Type J

19. Thermocouples

    Omega Iron Constantan, PFA coated, 1/8 inch probe diameter

20. Tubing and Tube fittings

    3/8 inch Teflon tubing, Swagelok and Cole-Parmer teflon fittings,

    1/4 inch polypropylene tubing and fittings

21. Valves

    - Chemkor 1/2 inch and 1 inch CPVC true union ball valves
    - Chemkor 1/2 inch CPVC single union ball valves
    - Ascolectric 1/4 inch solenoid valve, 9 Watts

22. Voltmeter

    Simpson digital display voltmeter

Appendix B

Calibration Curves and Analytical Methods

Table B.2: Calibration of the nitrogen rotameter, at STP

Float Elevation	*Flow in cm^3/min*
10	103.2
15	154.4
20	241.5
25	335.9
30	463.7
35	552.5
40	663.7
45	802.1
50	952.4
55	1067.6
60	1234.6

Table B.3: Calibration of the reactor gas rotameter, at STP

Float Elevation	Flow in cm^3/min
5	177.0
10	395.8
15	636.9
20	983.6
25	1339.3
30	1754.4
35	2158.3
40	2654.9
45	2884.6
50	3703.7

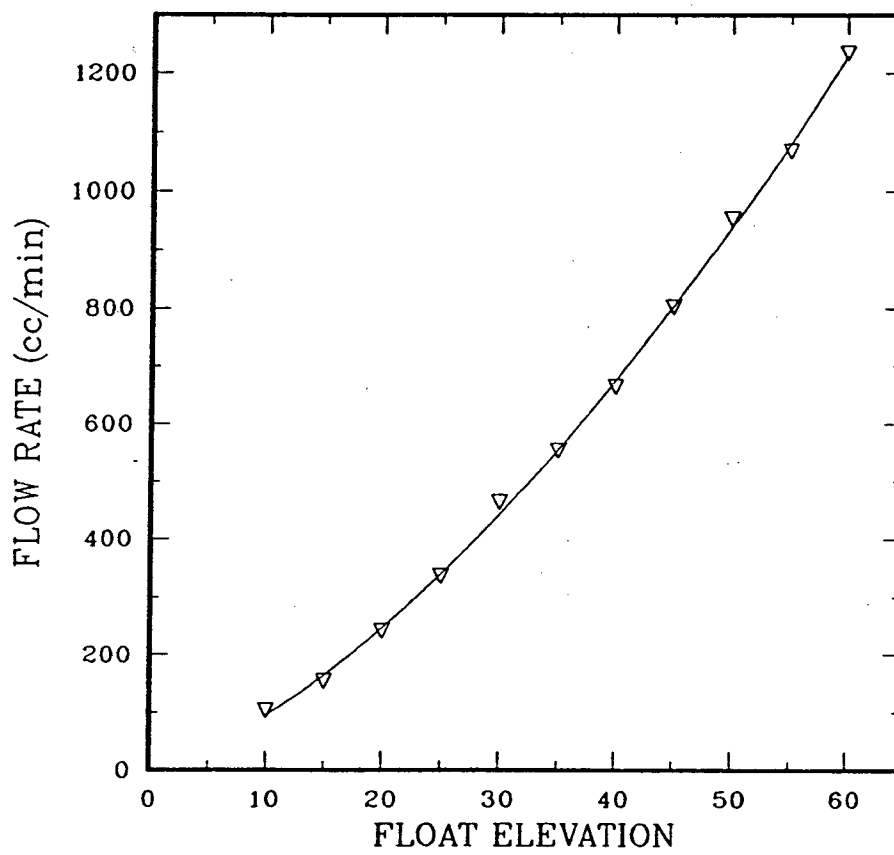

Figure B.19: Calibration curve for the nitrogen flow, at STP

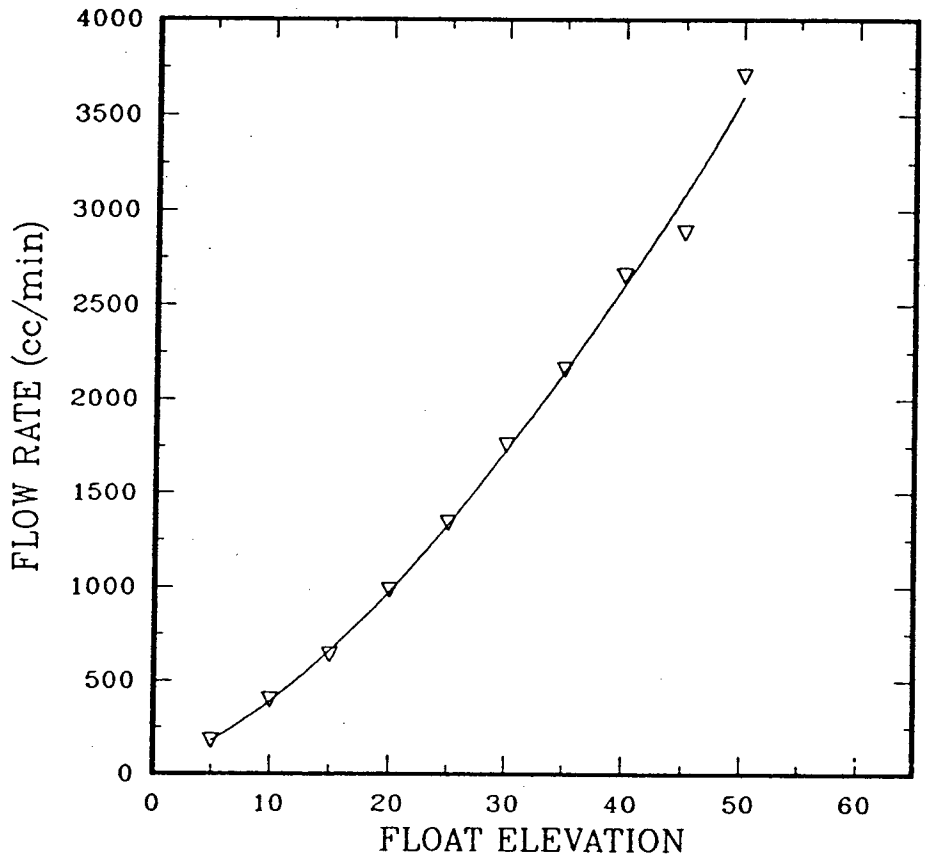

Figure B.20: Calibration curve for the reactor gas, at STP

Determination of Cerium(III)

- A 10 ml sample of the reactor suspension was taken.
- ~50 ml of 5 normal sulfuric acid was added.
- 2 to 3 grams of A.R. sodium bismuthate and 4 to 6 grams of ammonium sulphate was added.
- The mixture was boiled thoroughly until the color became somewhat lighter ensuring that all cerium(III) had been oxidized to cerium(IV). The reaction is:

$$2Ce_2(SO_4)_3 + 2NaBiO_3 + 6H_2SO_4 \Longrightarrow$$
$$4Ce(SO_4)_2 + Bi_2(SO_4)_3 + Na_2SO_4 + 6H_2O$$

- The mixture was cooled to room temperature and vacuum filtered using glass microfibre filter paper, 1.5 micrometer retention. The filter paper was washed with ~200 ml of 2 per cent sulfuric acid.
- Distilled water was added such that the total volume of the solution was 500 ml. After stirring a 50 ml sample was taken and the cerium(IV) concentration of this sample was determined by titration with ferrous ammonium sulphate(F.A.S.).

The cerium(IV) concentration in mol/l is equal to the number of milliliters of F.A.S. multiplied by the concentration in mol/l of F.A.S. The cerium(III) concentration is equal to the above determined cerium(IV) concentration minus the cerium(IV) concentration in the original sample.

Standardisation of Ferrous Ammonium Sulphate Solution and the Determination of the Cerium(IV) Concentration.

An $\sim$ 0.1 normal solution of ferrous ammonium sulphate(F.A.S.) was prepared. At the beginning of each day a $\sim$ 10 ml sample of a standard 0.1 normal ceric sulfate in dilute sulfuric acid solution was titrated with F.A.S. to determine the exact concentration of the F.A.S. solution. Two to three drops of the ferroin indicator were added to the sample to facilitate detection of the endpoint. Two to three of these titrations were generally carried out until the endpoints agreed within 0.05 ml.

A 10 ml sample of the reactor slurry with a few drops of ferroin was titrated with the F.A.S. solution. The cerium(IV) concentration in mol/l is equal to the number of milliliters of F.A.S. multiplied by the concentration in mol/l of F.A.S. divided by the sample size(10 ml).

Appendix C

Experimental Results

Table C.4: Slurries used in the kinetic studies

Solution	*Cerium(IV) Concentration mol/l*	*Total Cerium Concentration mol/l*	*Degree of Gel Formation in Cathode Studies*
A	0	0.50	none observed
B	0.48	0.56	,,
C	0.40	0.56	,,
D	0.29	0.56	some
E	0.21	0.56	some
F	0.12	0.56	none observed
G	0.51	0.76	some
H	0.39	0.76	medium
I	0.31	0.76	bad
J	0.20	0.76	medium
K	0.11	0.76	some
L	0	0.76	none observed
M	0	0.19	,,

some Only a light deposit was observed at the end of the run which did not seem to affect current-potential data.

medium At a constant current, the potential increased slowly throughout the run and the electrode needed to be cleaned once or twice each run.

bad Gel deposition was observed on both the working electrode and the reference electrode and both were cleaned every few minutes.

run One run consists of up to five current sweeps in one solution and comprises one complete set of data. Duration of the average run is approximately 1/2 hour.

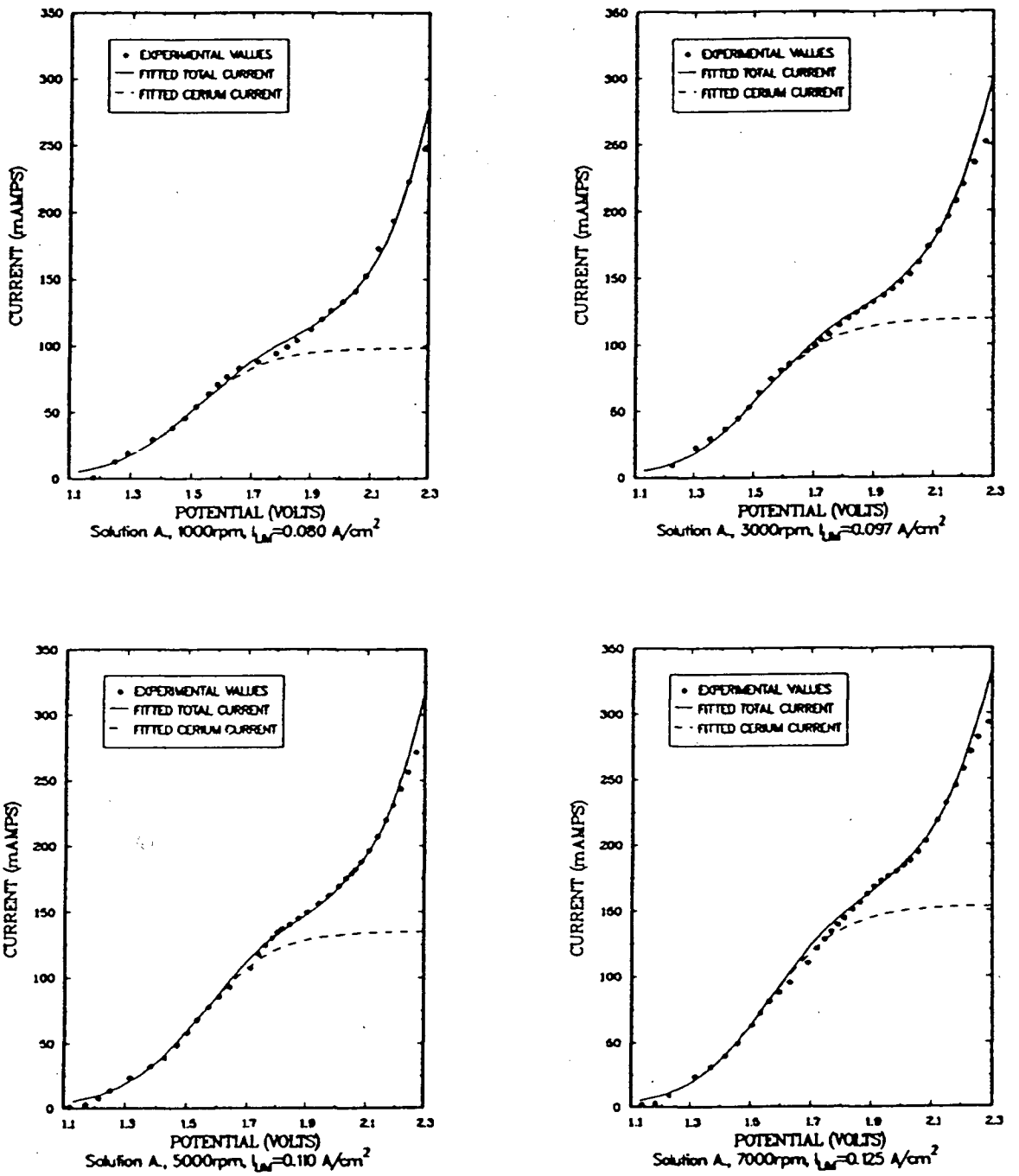

Figure C.21: Anode kinetic data in slurry A.
The Tafel parameters of the cerium reaction are: (i)slope 0.29 (ii)intercept 1.81, and of the oxygen reaction: (i)slope 0.41 (ii)intercept 1.00. The potential is with respect to the standard calomel electrode. The electrode area is 1.23 cm^2.

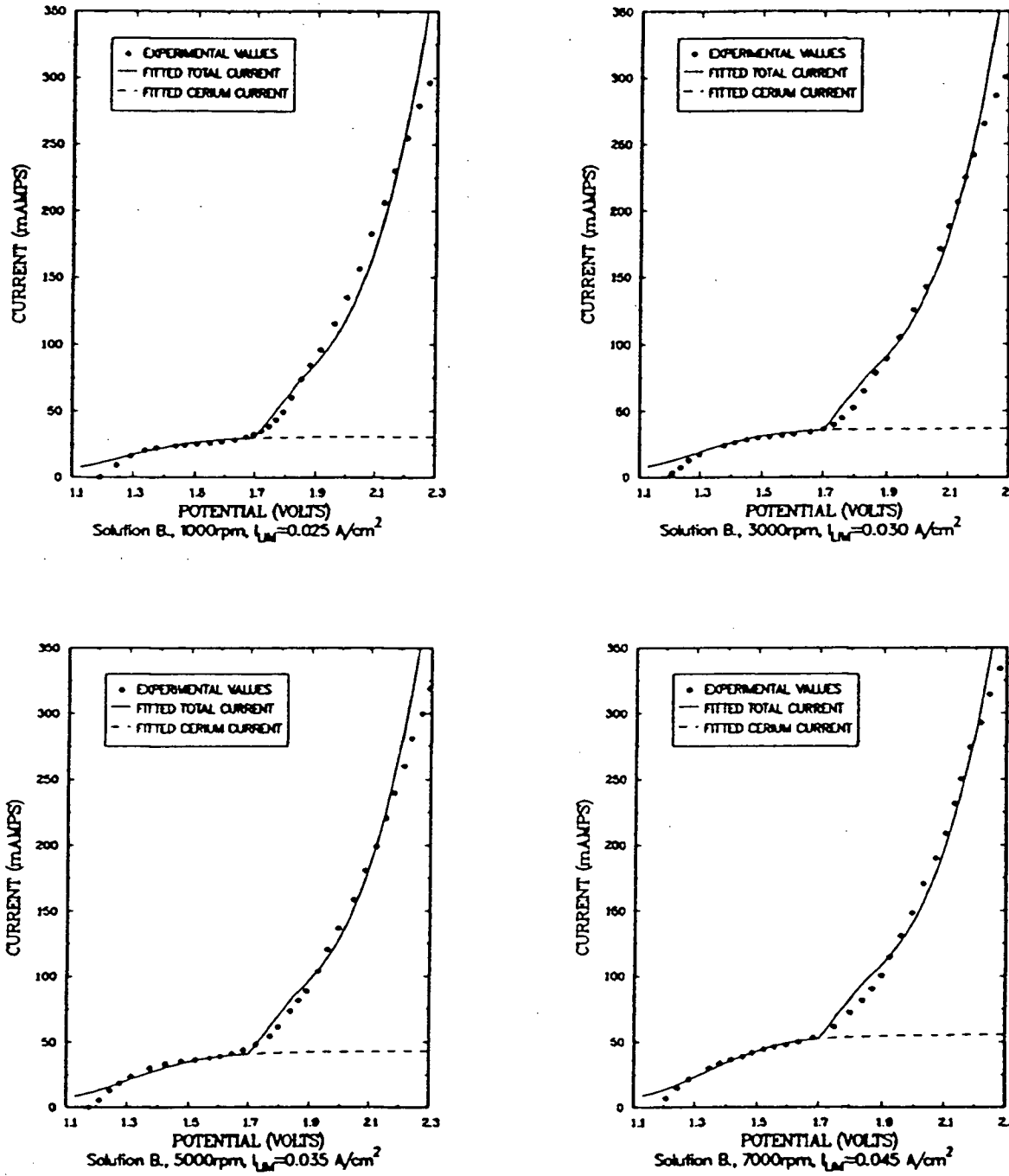

Figure C.22: Anode kinetic data in slurry B.
The Tafel parameters of the cerium reaction are: (i)slope 0.29 (ii)intercept 1.73, and of the oxygen reaction: (i)slope 0.48 (ii)intercept 0.63. The potential is with respect to the standard calomel electrode. The electrode area is 1.23 cm^2.

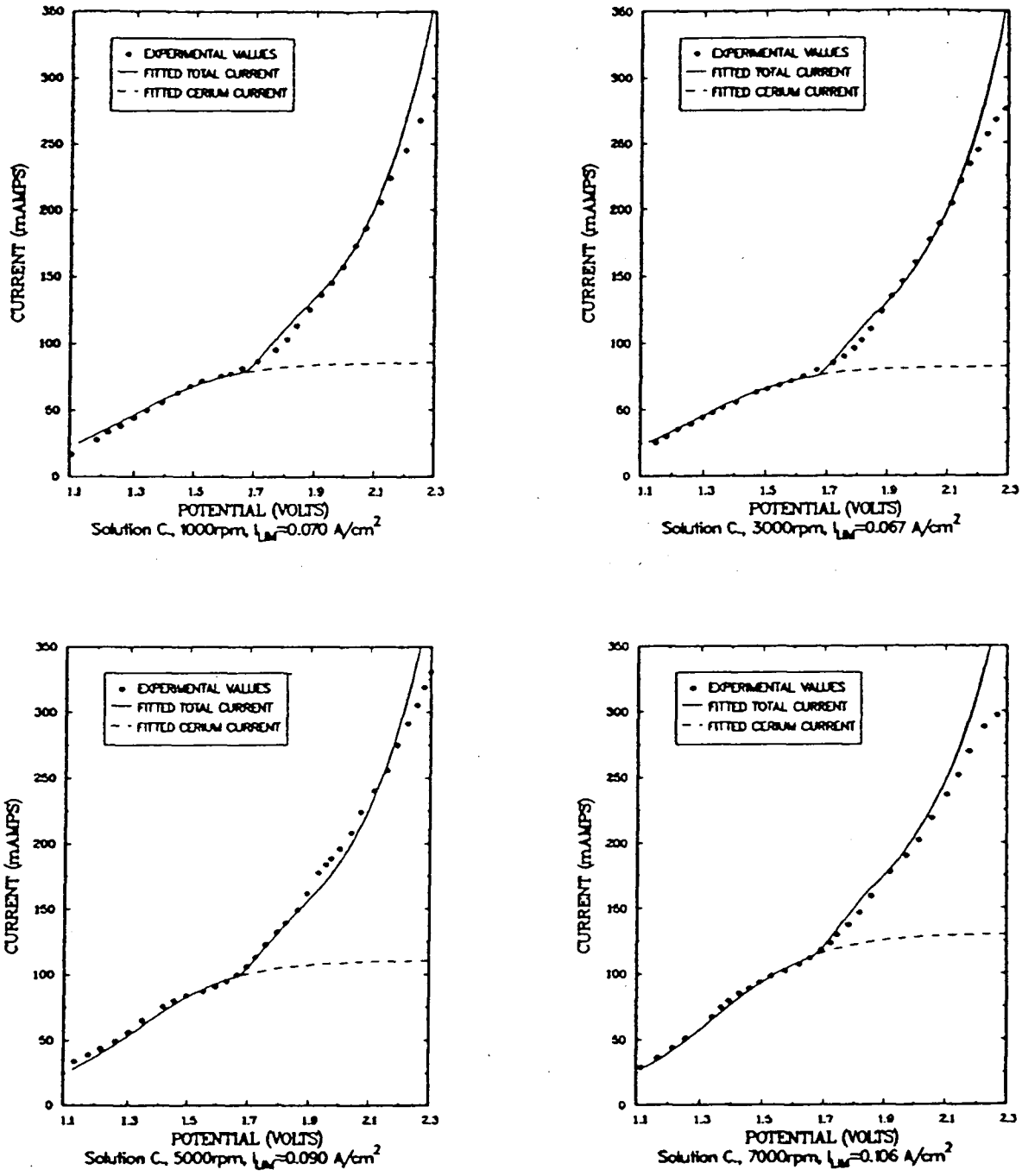

Figure C.23: Anode kinetic data in slurry C.
The Tafel parameters of the cerium reaction are: (i)slope 0.39 (ii)intercept 1.72, and of the oxygen reaction: (i)slope 0.53 (ii)intercept 0.52. The potential is with respect to the standard calomel electrode. The electrode area is 1.23 cm^2.

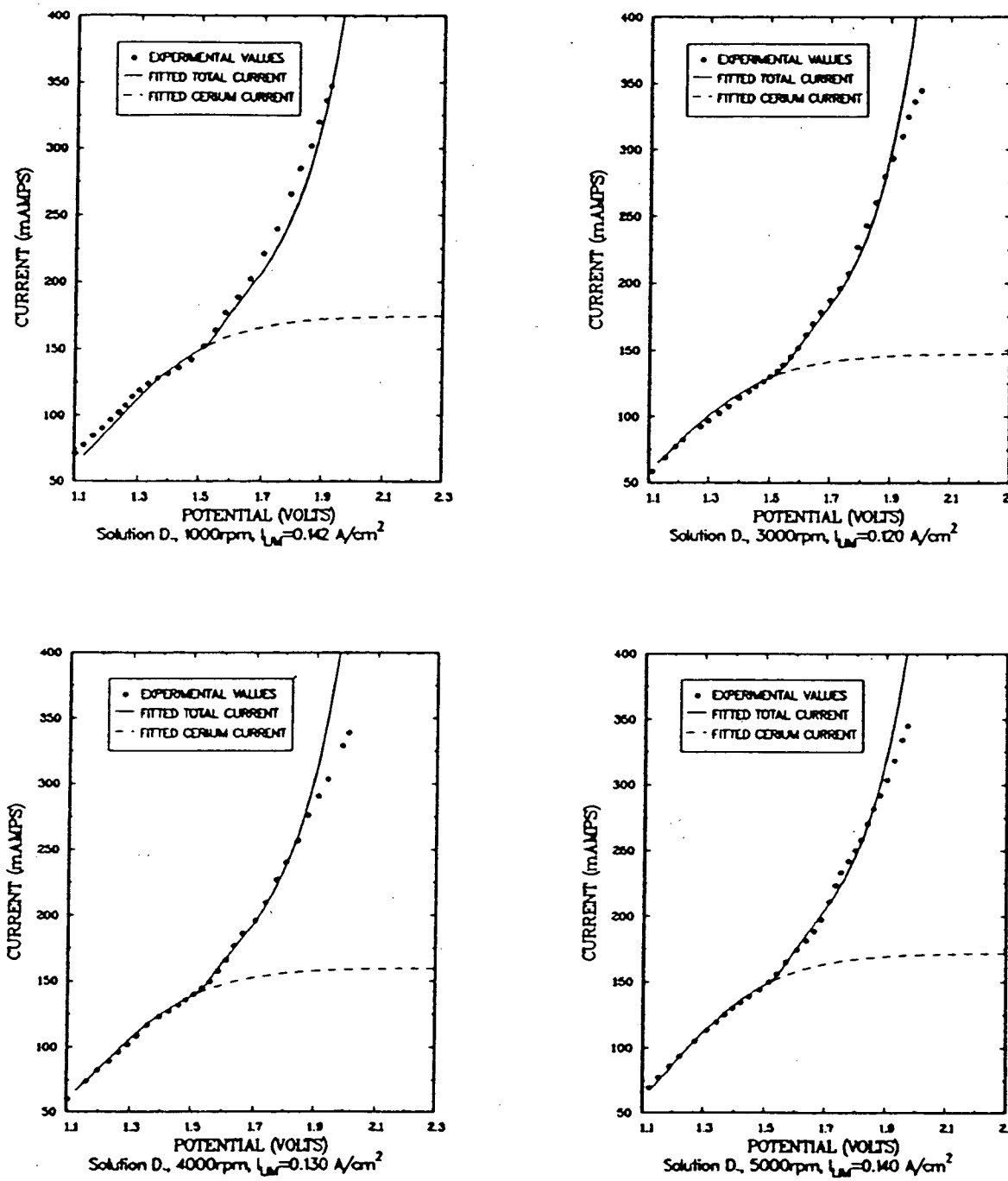

Figure C.24: Anode kinetic data in slurry D.
The Tafel parameters of the cerium reaction are: (i)slope 0.39 (ii)intercept 1.53, and of the oxygen reaction: (i)slope 0.36 (ii)intercept 0.79. The potential is with respect to the standard calomel electrode. The electrode area is 1.23 cm^2.

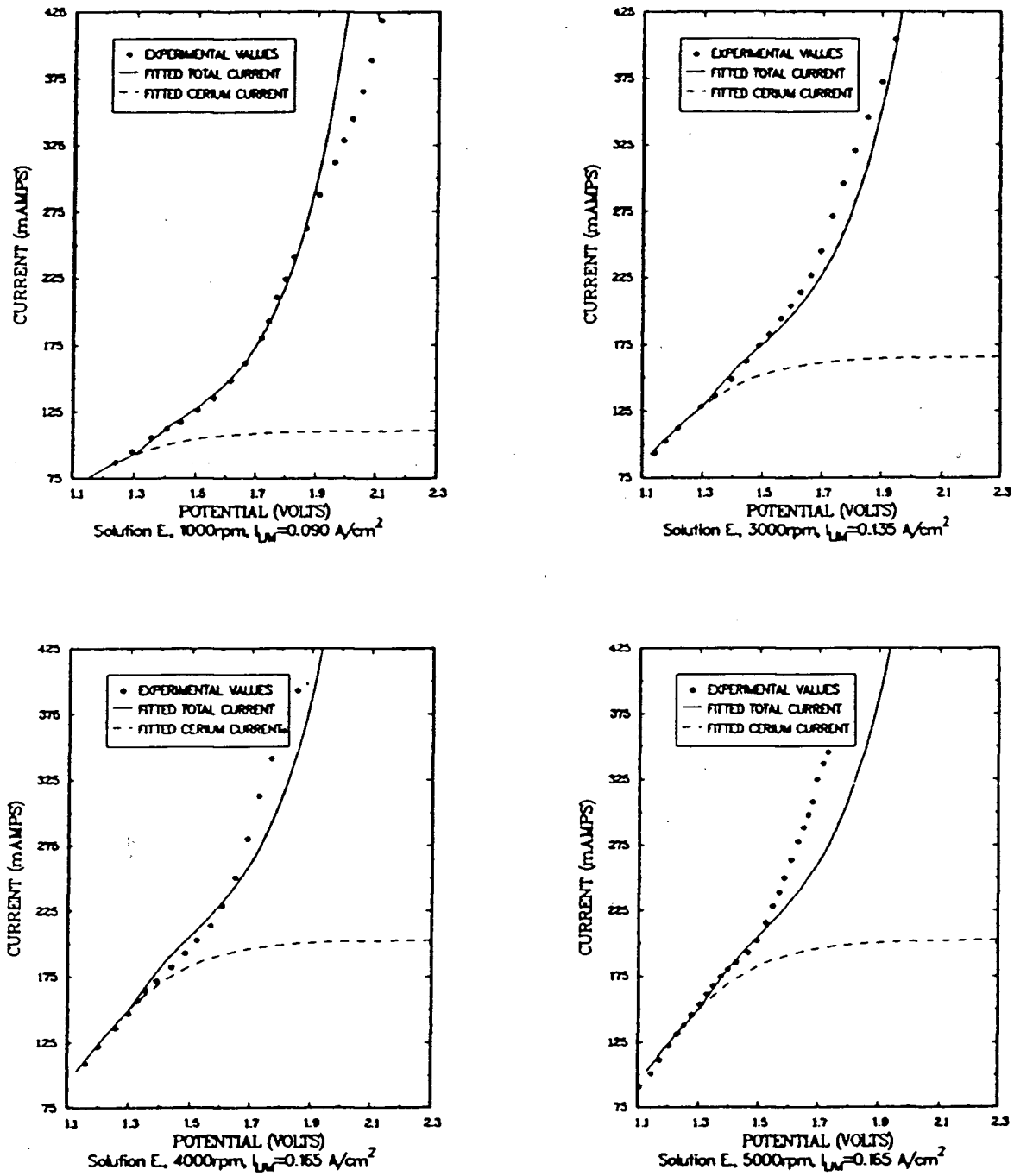

Figure C.25: Anode kinetic data in slurry E.
The Tafel parameters of the cerium reaction are: (i)slope 0.39 (ii)intercept 1.43, and of the oxygen reaction: (i)slope 0.44 (ii)intercept 0.50. The potential is with respect to the standard calomel electrode. The electrode area is 1.23 cm^2.

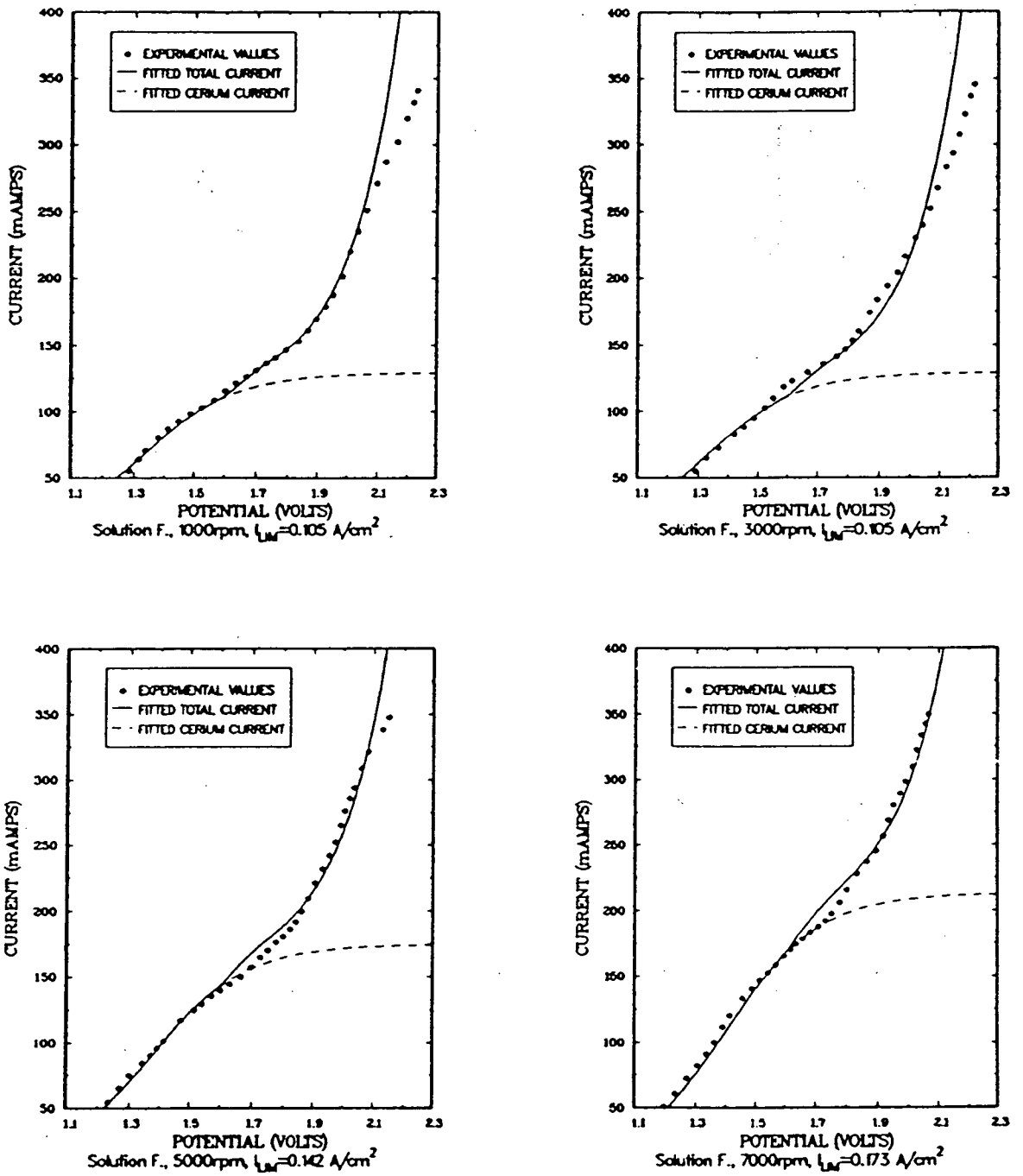

Figure C.26: Anode kinetic data in slurry F.
The Tafel parameters of the cerium reaction are: (i)slope 0.36 (ii)intercept 1.67, and of the oxygen reaction: (i)slope 0.35 (ii)intercept 1.00. The potential is with respect to the standard calomel electrode. The electrode area is 1.23 cm^2.

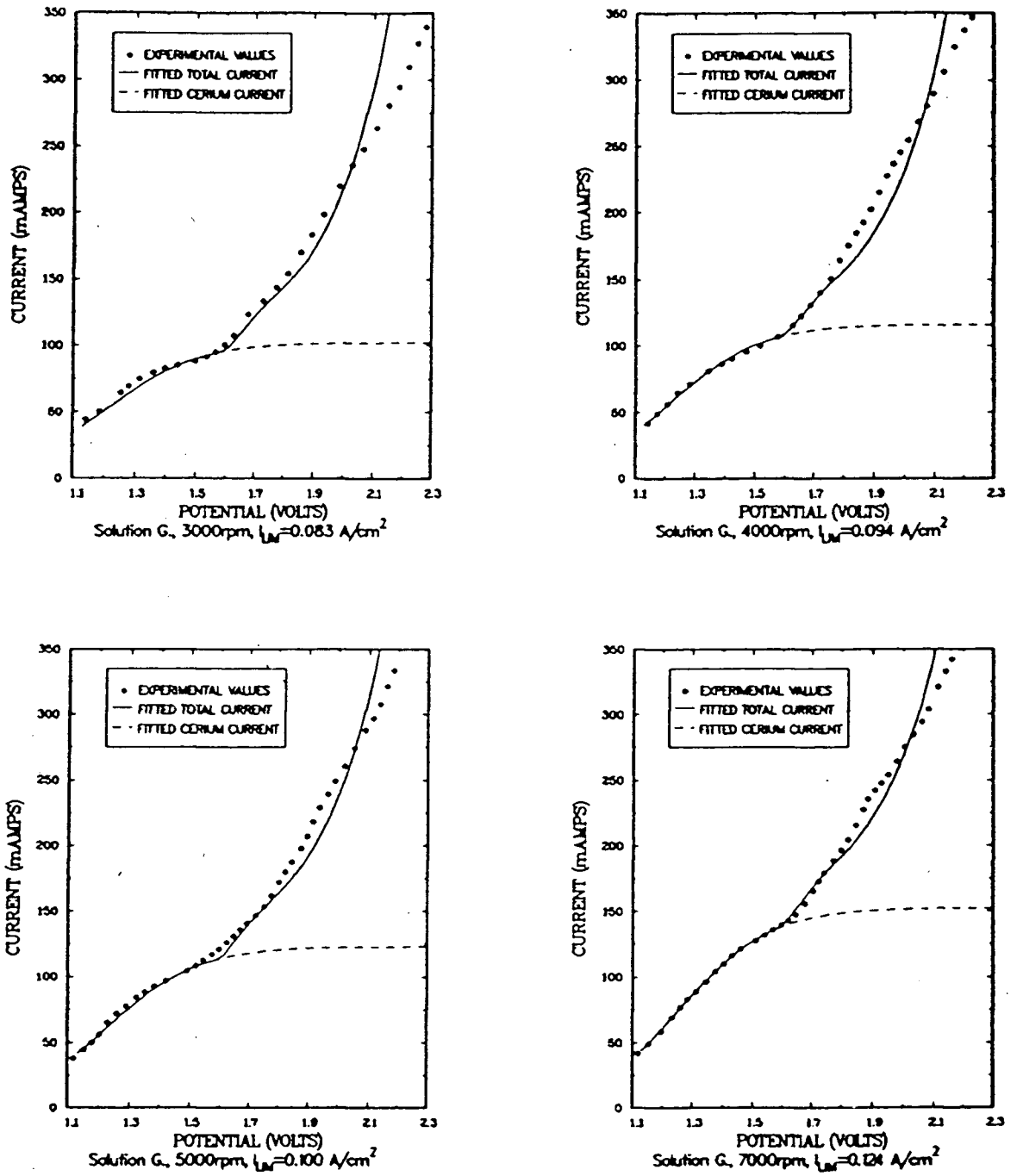

Figure C.27: Anode kinetic data in slurry G.
The Tafel parameters of the cerium reaction are: (i)slope 0.34 (ii)intercept 1.57, and of the oxygen reaction: (i)slope 0.46 (ii)intercept 0.63. The potential is with respect to the standard calomel electrode. The electrode area is 1.23 cm^2.

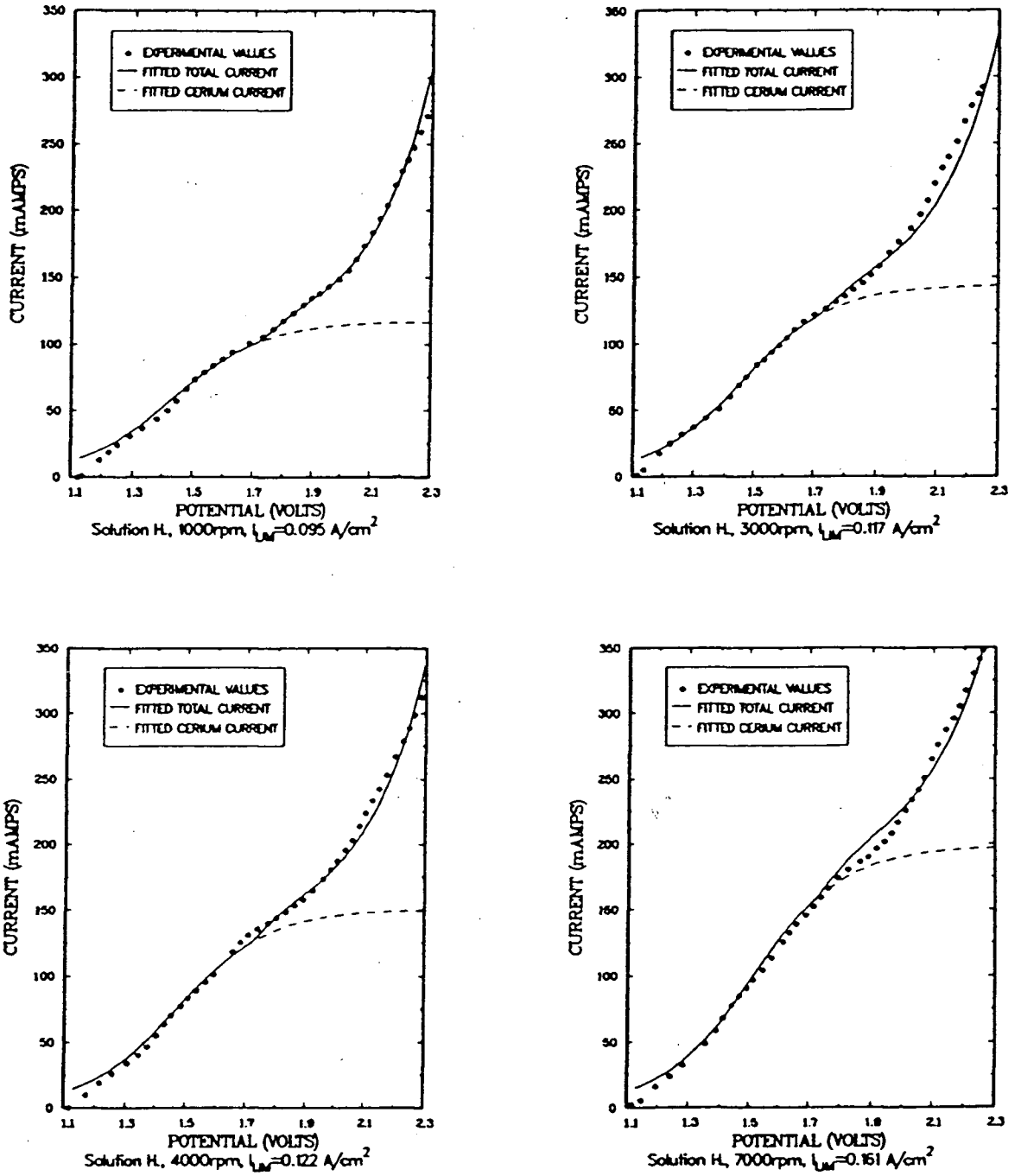

Figure C.28: Anode kinetic data in slurry H.
The Tafel parameters of the cerium reaction are: (i)slope 0.35 (ii)intercept 1.79, and of the oxygen reaction: (i)slope 0.42 (ii)intercept 0.96. The potential is with respect to the standard calomel electrode. The electrode area is 1.23 cm^2.

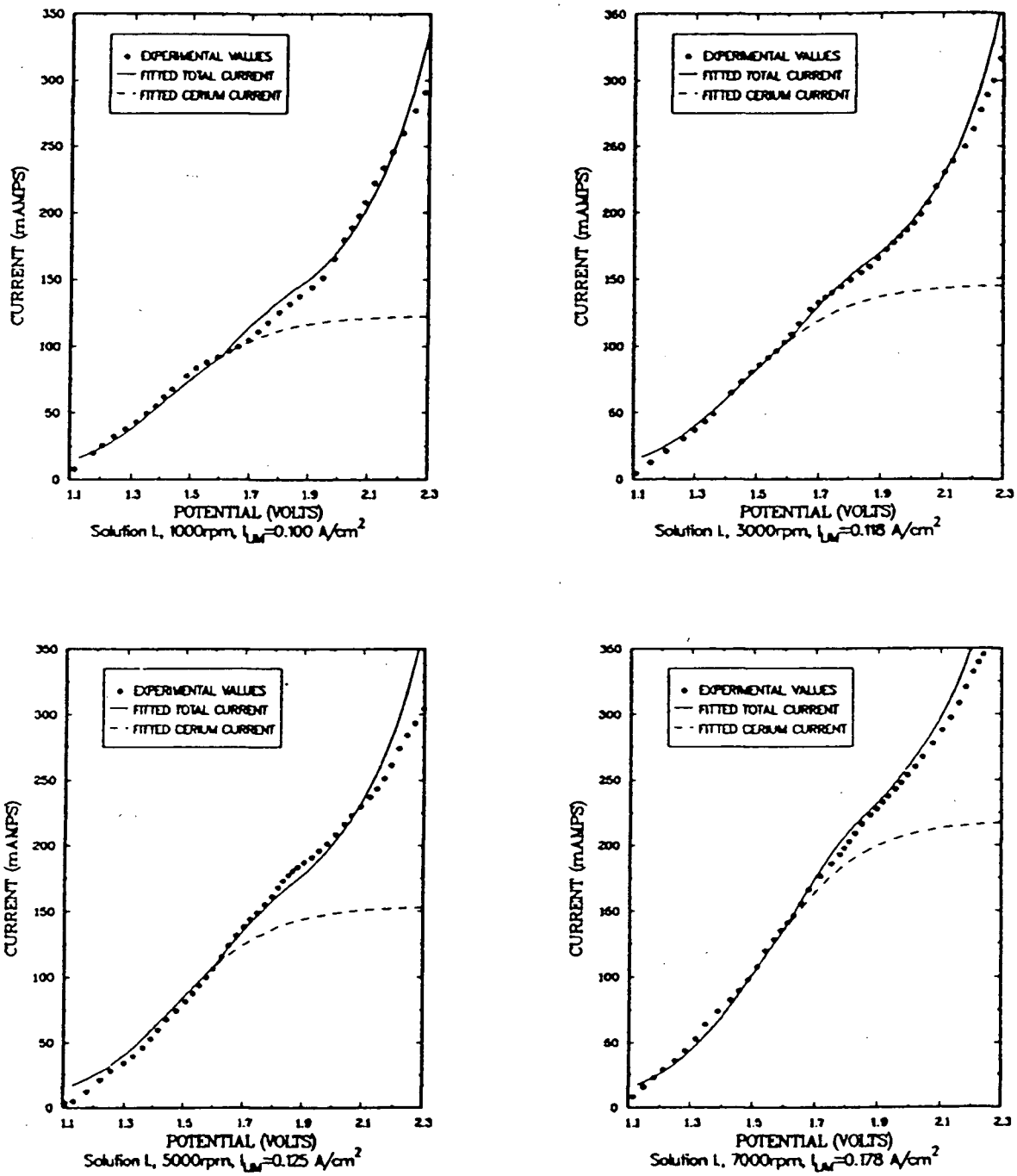

Figure C.29: Anode kinetic data in slurry I.
The Tafel parameters of the cerium reaction are: (i)slope 0.37 (ii)intercept 1.80, and of the oxygen reaction: (i)slope 0.49 (ii)intercept 0.71. The potential is with respect to the standard calomel electrode. The electrode area is 1.23 cm^2.

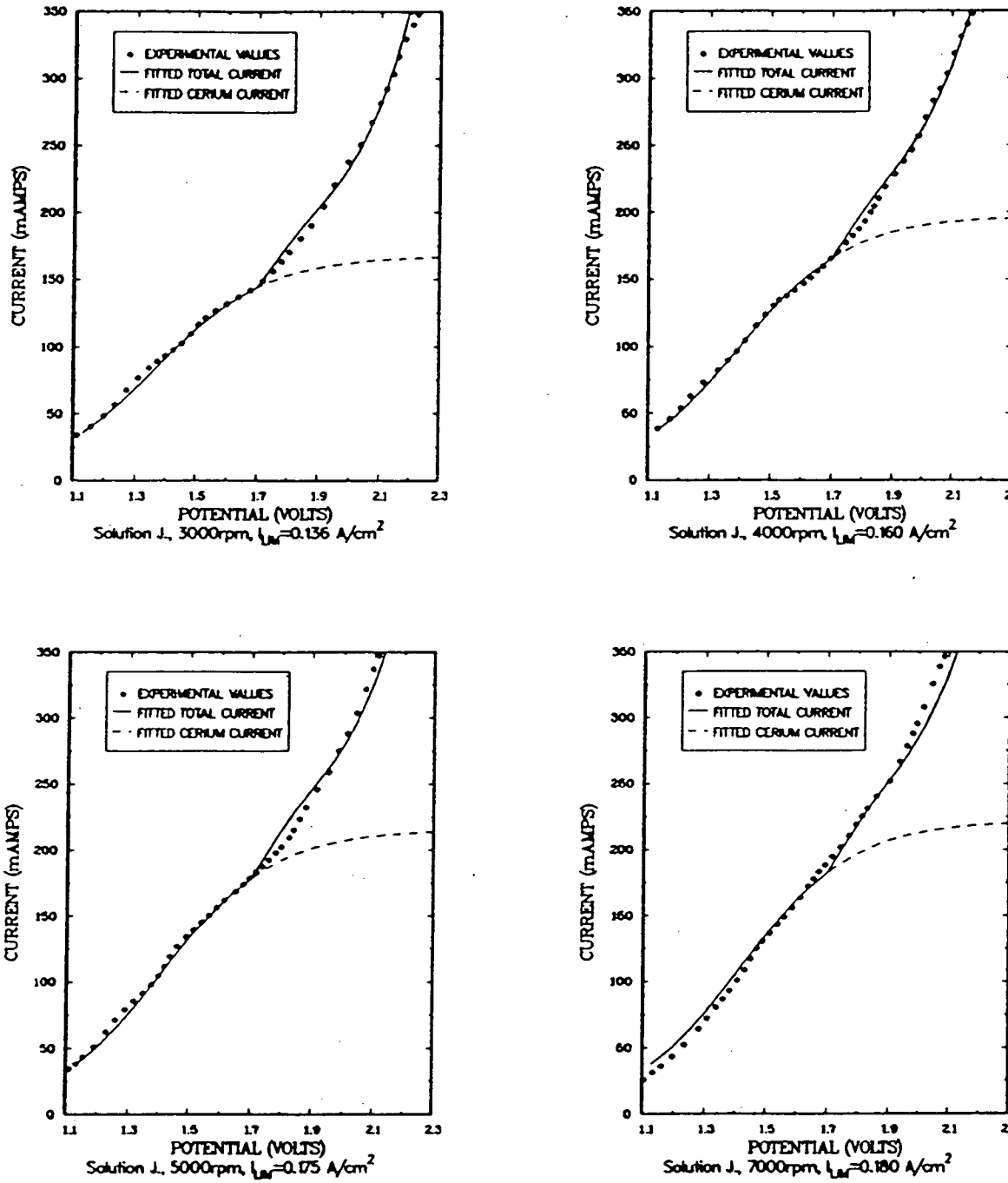

Figure C.30: Anode kinetic data in slurry J.
The Tafel parameters of the cerium reaction are: (i)slope 0.42 (ii)intercept 1.73, and of the oxygen reaction: (i)slope 0.48 (ii)intercept 0.67. The potential is with respect to the standard calomel electrode. The electrode area is 1.23 cm^2.

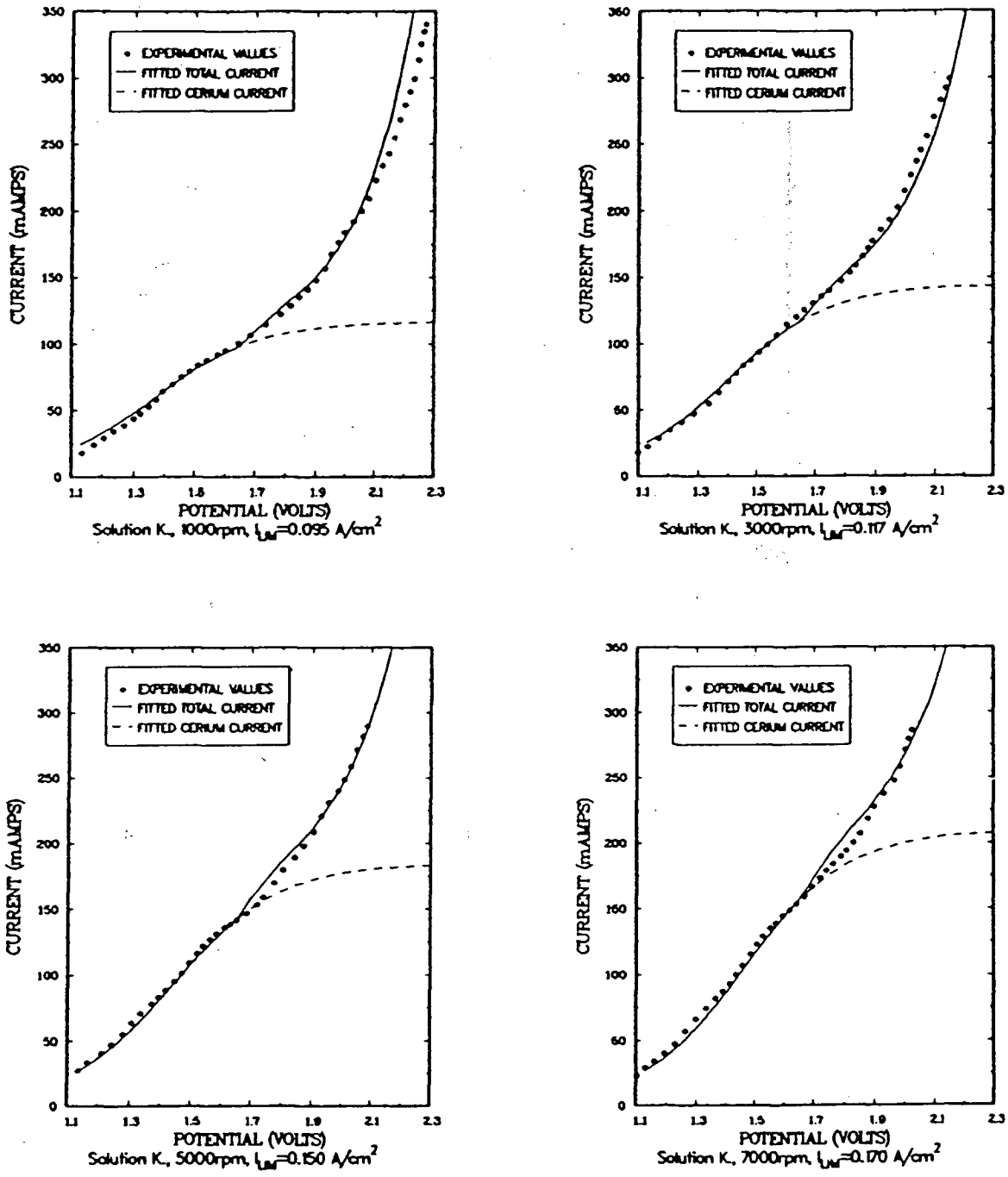

Figure C.31: Anode kinetic data in slurry K.
The Tafel parameters of the cerium reaction are: (i)slope 0.40 (ii)intercept 1.77, and of the oxygen reaction: (i)slope 0.42 (ii)intercept 0.85. The potential is with respect to the standard calomel electrode. The electrode area is 1.23 cm^2.

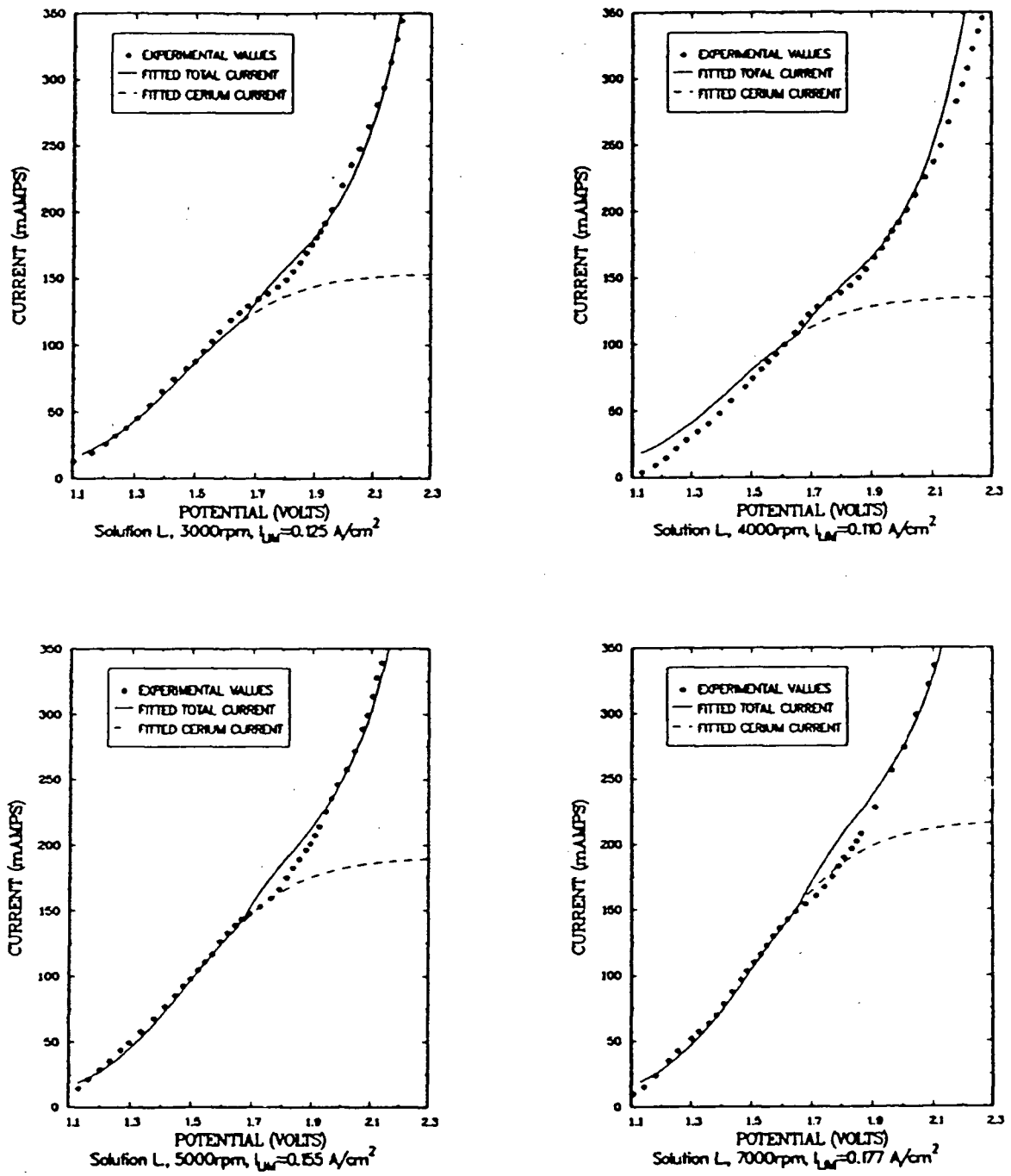

Figure C.32: Anode kinetic data in slurry L.
The Tafel parameters of the cerium reaction are: (i)slope 0.38 (ii)intercept 1.80, and of the oxygen reaction: (i)slope 0.41 (ii)intercept 0.88. The potential is with respect to the standard calomel electrode. The electrode area is 1.23 cm^2.

Table C.5: Partial current density data of the cerium reduction reaction on the rotating wire cathode, area 1.255 cm^2.

Solution	*Speed rpm*	*Current mAmps*	*Current Density Amps/cm²*
D	3000	17.5	0.014
	6000	50	0.040
	1000	15	0.012
	1000	20	0.016
	3000	19	0.015
E	3000	40	0.032
	6000	17.5	0.014
	6000	45	0.036
	1000	50	0.040
F	3000	32	0.025
	3000	38	0.030
	6000	43	0.034
	1000	50	0.040
G	3000	83	0.066
	1000	83	0.066
	6000	57.5	0.046
	6000	17.5	0.014
H	3000	75	0.060
	6000	80	0.064
	1000	75	0.060
I	3000	10	0.008
	3000	70	0.056
	6000	75	0.060
	1000	75	0.060
J	3000	25	0.020
	6000	45	0.036
	1000	45	0.036
K	3000	15	0.012
	3000	17.5	0.014
	6000	30	0.024
	1000	22.5	0.018
L	all	0	0

Table C.6: Results of cathode kinetic study, slurries A,B, and C.

Slurry	*Current (Amps)*	*Potential (-Volts)*	*iR-drop (Volts)*	*iR-corrected pot. (-Volts)*
A	0.5	0.84	0.13	0.71
	1.0	1.25	0.28	0.97
	1.5	1.64	0.46	1.18
	2.0	2.01	0.65	1.36
	2.5	2.45	0.85	1.60
	3.0	2.90	1.10	1.80
	3.5	3.33	1.30	2.03
	4.0	3.86	1.45	2.41
	4.5	4.45	1.70	2.75
B	0.5	1.00	0.30	0.70
	1.0	1.44	0.61	0.83
	1.5	1.87	0.99	0.88
	2.0	2.30	1.46	0.84
	2.5	2.74	1.80	0.94
	3.0	3.26	2.25	1.01
	3.5	3.76	2.80	0.96
	4.0	4.32	3.48	0.84
	4.5	4.91	3.87	1.04
C	0.5	1.07	0.29	0.78
	1.0	1.48	0.64	0.84
	1.5	1.90	1.04	0.86
	2.0	2.33	1.46	0.87
	2.5	2.83	2.00	0.83
	3.0	3.38	2.49	0.89
	3.5	3.88	2.95	0.93
	4.0	4.46	3.46	1.00
	4.5	5.23	4.30	0.93

The cathode area is 1.255 cm^2; temperature 50 ^{0}C, pressure 1 atm, speed 1000 - 6000 rpm.

Table C.7: Results of cathode kinetic study, slurries D,E, and F.

Slurry	*Current (Amps)*	*Potential (-Volts)*	*iR-drop (Volts)*	*iR-corrected pot. (-Volts)*
D	0.5	1.14	0.08	1.06
	1.0	1.56	0.21	1.35
	1.5	2.01	0.38	1.63
	2.0	2.44	0.50	1.94
	2.5	2.94	0.72	2.22
	3.0	3.51	0.75	2.76
	3.5	4.05	0.88	3.17
	4.0	4.67	1.00	3.67
	4.5	5.40	1.25	4.15
E	0.5	1.15	0.08	1.07
	1.0	1.54	0.21	1.33
	1.5	1.94	0.35	1.59
	2.0	2.30	0.42	1.88
	2.5	2.75	0.55	2.20
	3.0	3.22	0.63	2.59
	3.5	3.78	0.70	3.08
	4.0	4.42	0.88	3.54
	4.5	5.02	0.99	4.03
F	0.5	0.89	0.06	0.83
	1.0	1.17	0.13	1.04
	1.5	1.43	0.23	1.20
	2.0	1.70	0.30	1.40
	2.5	2.02	0.38	1.64
	3.0	2.28	0.45	1.83
	3.5	2.58	0.53	2.05
	4.0	2.92	0.60	2.32
	4.5	3.35	0.68	2.67

The cathode area is 1.255 cm^2; temperature 50 ^{0}C, pressure 1 atm, speeds 1000 - 6000 rpm.

Table C.8: Results of cathode kinetic study, slurries G,H, and I.

Slurry	*Current (Amps)*	*Potential (-Volts)*	*iR-drop (Volts)*	*iR-corrected pot. (-Volts)*
G	0.5	1.46	0.15	1.31
	1.0	1.84	0.16	1.68
	1.5	2.25	0.25	2.00
	2.0	2.75	0.35	2.40
	2.5	3.26	0.45	2.81
	3.0	3.74	0.59	3.15
	3.5	4.24	0.73	3.51
	4.0	4.71	0.76	3.95
	4.5	5.54	0.81	4.73
H	0.5	1.23	0.05	1.18
	1.0	1.76	0.15	1.61
	1.5	2.29	0.23	2.06
	2.0	2.85	0.27	2.58
	2.5	3.49	0.39	3.10
	3.0	4.12	0.42	3.70
	3.5	4.75	0.49	4.26
	4.0	5.52	0.56	4.96
	4.5	6.45	0.63	5.82
I	0.5	1.14	0.06	1.08
	1.0	1.63	0.14	1.49
	1.5	2.13	0.25	1.88
	2.0	2.64	0.33	2.31
	2.5	3.22	0.42	2.80
	3.0	3.76	0.50	3.26
	3.5	4.36	0.58	3.78
	4.0	5.04	0.66	4.38
	4.5	5.94	0.75	5.19

The cathode area is 1.255 cm^2; temperature 50 ^{0}C, pressure 1 atm, speed 1000-6000 rpm.

Table C.9: Results of cathode kinetic study, slurries J,K, and L.

Slurry	*Current (Amps)*	*Potential (-Volts)*	*iR-drop (Volts)*	*iR-corrected pot. (-Volts)*
J	0.5	1.13	0.06	1.07
	1.0	1.63	0.15	1.48
	1.5	2.11	0.27	1.84
	2.0	2.51	0.36	2.15
	2.5	3.00	0.45	2.55
	3.0	3.51	0.54	2.97
	3.5	4.06	0.63	3.43
	4.0	4.63	0.72	3.91
	4.5	5.41	0.81	4.60
K	0.5	1.08	0.06	1.02
	1.0	1.56	0.20	1.36
	1.5	2.00	0.30	1.70
	2.0	2.42	0.40	2.02
	2.5	2.84	0.50	2.34
	3.0	3.30	0.60	2.70
	3.5	3.82	0.70	3.12
	4.0	4.40	0.80	3.60
	4.5	5.11	0.90	4.21
L	0.5	1.00	0.06	0.94
	1.0	1.45	0.17	1.28
	1.5	1.93	0.29	1.64
	2.0	2.33	0.37	1.96
	2.5	2.78	0.50	2.28
	3.0	3.29	0.57	2.72
	3.5	3.78	0.73	3.05
	4.0	4.32	0.80	3.52
	4.5	4.99	0.90	4.09

The cathode area is 1.255 cm^2; temperature 50 ^{0}C, pressure 1 atm, speeds 1000 - 6000 rpm.

Table C.10: Results of cathode kinetic study, slurry M.

Slurry	*Current (Amps)*	*Potential (-Volts)*	*iR-drop (Volts)*	*iR-corrected pot. (-Volts)*
M	0.5	0.81	0.09	0.72
	1.0	1.10	0.19	0.91
	1.5	1.39	0.28	1.11
	2.0	1.69	0.37	1.32
	2.5	2.01	0.47	1.54
	3.0	2.41	0.56	1.85
	3.5	2.76	0.65	2.11
	4.0	3.22	0.75	2.47
	4.5	3.73	0.84	2.89

The cathode area is 1.255 cm^2, temperature 50 ^{0}C, pressure 1 atm, speeds 1000 - 6000 rpm.

Tables C.11 to C.18 contain the experimental results of the tube and wire reactor as well as the modelling results as predicted by 'the model' (see Chapter 5, Section Modelling, and Appendix D, Section D1).

The reactor gas composition is given in molar percent of hydrogen and oxygen. Nitrogen was added to the first two runs whereas the later runs are corrected for the presence of air through the detection of nitrogen. For these reasons the sum of the hydrogen and oxygen molar percentages may not add to one hundred percent.

The Ce^{III} concentration refers to cerous sulfate complexes dissolved in solution.

The tabulated current efficiencies are overall current efficiencies for the production of cerium(IV) and are average values over the time period of one hour between sampling times. The best fit current efficiency is a least squares fitted current efficiency of the experimental values, which are based on a concentration analysis or a gas composition analysis (see Sample Calculation 1). These current efficiencies are also plotted in Figures C.33 to C.34.

The rotameter flow is given as a rotameter reading. For actual flow rates see the calibration curve in Appendix B.

Table C.11: Experimental and modelling results of flow reactor run 1

RUN 1											
Velocity = ~2.8 m/s, Current = 18 Amps											
Total Cerium concentration(incl. solids) = 0.52 Molar											
Time	*Reactor Gas Molar %*		*Ce(IV) conc.*	*Ce(III) conc.*	*Cell Pot.*	*Current Efficiency*			*Model*		
						gas	*conc.*	*best*	*Ce(III)*	*Pot.*	*Current*
hrs	H_2	O_2	*mol/l*	*mol/l*	*Volts*	*anal.*	*anal.*	*fit*	*mol/l*	*Volts*	Eff.
1	100*	0	0.04	0.25	3.30	1.00	1.17	1.09	0.24	3.34	0.88
2	100*	0	0.08	0.24	3.27	1.00	0.98	1.01	0.25	3.31	0.90
3	100*	0	0.12	0.26	3.25	1.00	1.12	0.98	0.27	3.28	0.92
4	100*	0	0.15	0.25	3.14	1.00	0.84	0.97	0.28	3.62	0.93
5	100*	0	0.19	0.28	2.90	1.00	0.93	0.97	0.29	3.65	0.93
6	100*	0	0.22		2.96	1.00	0.90	0.97	0.30	3.68	0.94
7	100*	0	0.25		2.93	1.00	0.90	0.96	0.27	3.74	0.91
8	100*	0	0.28		2.99	1.00	0.90	0.93	0.24	3.80	0.86
9	30.3	0.5	0.32	0.20	3.10	0.97	0.90	0.89	0.20	3.85	0.79
10	24.6	1.7	0.35	0.19	3.17	0.86	0.79	0.82	0.17	3.88	0.72
11	23.7	3.2	0.37	0.16	3.19	0.73	0.73	0.73	0.15	3.29	0.64
12	23.0	4.5	0.39	0.12	3.21	0.61	0.52	0.62	0.13	3.33	0.59
13	22.6	5.7	0.41	0.09	3.22	0.49	0.46	0.50	0.11	3.36	0.53
14	22.1	6.8	0.43	0.09	3.22	0.39	0.49	0.38	0.09	3.39	0.47
15	23.0	8.1	0.43	0.08	3.23	0.30	0.11	0.26	0.09	3.39	0.45
16	22.7	8.9	0.44	0.07	3.24	0.22	0.24	0.16	0.08	3.40	0.42
17	22.4	9.4	0.44	0.06	3.24	0.16	-.03	0.10	0.08	3.40	0.42

* These concentrations are estimated since actual numbers are not availabe due to a leaky sample port.

Table C.12: Experimental and modelling results of flow reactor run 2

RUN 2 *Velocity = ~2.8 m/s, Current = 50 Amps* *Total Cerium concentration(incl. solids) = 0.51 Molar*											
Time	*Reactor Gas Molar %*		*Ce(IV) conc.*	*Ce(III) conc.*	*Cell Pot.*	*Current Efficiency*			*Model*		
						gas	*conc.*	*best*	*Ce(III)*	*Pot.*	*Current*
hrs	H_2	O_2	*mol/l*	*mol/l*	*Volts*	*anal.*	*anal.*	*fit*	*mol/l*	*Volts*	Eff.
1	90.7	3.3	0.08	0.28	4.38	0.93	0.80	0.88	0.25	5.90	0.35
2	93.3	5.2	0.18	0.28	4.42	0.89	0.95	0.86	0.29	6.61	0.38
3	87.7	10.9	0.23	0.25	4.46	0.75	0.55	0.73	0.28	6.80	0.37
4	80.1	18.7	0.30	0.19	4.45	0.53	0.66	0.56	0.21	6.66	0.31
5	74.7	24.0	0.34	0.15	4.50	0.36	0.41	0.39	0.17	6.50	0.27
6	71.6	27.3	0.37	0.13	4.50	0.24	0.29	0.25	0.14	4.69	0.23
7	69.3	29.5	0.39	0.11	4.49	0.15	0.15	0.16	0.12	4.70	0.22
8	67.9	31.0	0.40	0.09	4.47	0.09	0.13	0.11	0.11	4.71	0.20
9	67.1	31.8	0.41	0.11	4.48	0.05	0.07	0.06	0.10	4.71	0.19

Table C.13: Experimental and modelling results of flow reactor run 3

RUN 3 *Velocity = ~2.8 m/s, Current = 34 Amps* *Total Cerium concentration(incl. solids) = 0.59 Molar*												
Time	*Reactor Gas*			*Ce(IV)*	*Ce(III)*	*Cell*	*Current Efficiency*			*Model*		
	Rot.	*Molar %*		*conc.*	*conc.*	*Pot.*	*gas*	*conc.*	*best*	*Ce(III)*	*Pot.*	*Current*
hrs	*Flow*	H_2	O_2	*mol/l*	*mol/l*	*Volts*	*anal.*	*anal.*	*fit*	*mol/l*	*Volts*	Eff.
1	5	90.6	1.1	0.07	0.24	4.38	0.97	1.07	1.01	0.27	4.69	0.53
2	3-5	96.7	0.5	0.15	0.28	4.19	0.99	1.02	1.04	0.30	5.36	0.56
3	4	89.4	1.0	0.22	0.31	4.17	0.98	0.99	1.00	0.32	5.41	0.59
4	4	96.2	2.4	0.28		4.22	0.95	0.94	0.92	0.31	5.54	0.58
5	5	93.5	6.6	0.33		4.26	0.86	0.76	0.80	0.26	5.50	0.51
6	5-6	87.7	14.1	0.39		4.29	0.68	0.84	0.66	0.20	5.39	0.43
7	6	82.0	18.8	0.41	0.15	4.28	0.54	0.20	0.52	0.18	5.35	0.41
8	6-7	78.0	22.3	0.43	0.14	4.29	0.43	0.33	0.39	0.16	5.29	0.38
9	7	74.8	25.4	0.46		4.30	0.32	0.46	0.29	0.13	4.16	0.33
10	7	73.1	27.9	0.46	0.11	4.29	0.24	0.01	0.21	0.13	4.16	0.33
11	7-8	71.4	29.1	0.48		4.30	0.19	0.26	0.15	0.11	4.18	0.30
12	7-8	71.5	29.7	0.48	0.08	4.08	0.17	0.01	0.13	0.11	4.18	0.29
13	7-8	70.5	30.9	0.50		4.06	0.12	0.20	0.12	0.09	4.18	0.27
14	7-8	68.6	31.2	0.50	0.09	4.03	0.09	0.03	0.11	0.09	4.19	0.27
15	7-8	68.9	32.2	0.51		4.03	0.07	0.11	0.07	0.08	4.19	0.25

Table C.14: Experimental and modelling results of flow reactor run 4

RUN 4 *Velocity = ~1.1 m/s, Current = 50 Amps* *Total Cerium concentration(incl. solids) = 0.60 Molar*												
Time	*Reactor Gas*			*Ce(IV)*	*Ce(III)*	*Cell*	*Current Efficiency*			*Model*		
	Rot.	*Molar %*		*conc.*	*conc.*	*Pot.*	*gas*	*conc.*	*best*	*Ce(III)*	*Pot.*	*Current*
hrs	*Flow*	H_2	O_2	*mol/l*	*mol/l*	*Volts*	*anal.*	*anal.*	*fit*	*mol/l*	*Volts*	Eff.
1	10	81.8	18.8	0.07	0.25	4.84	0.54	0.64	0.56	0.27	5.93	0.23
2	10	81.7	18.8	0.12	0.28	4.87	0.54	0.50	0.58	0.29	6.91	0.24
3	10	80.7	19.9	0.18		5.07	0.51	0.58	0.56	0.31	6.74	0.25
4	10	80.8	20.1	0.23	0.33	5.08	0.50	0.57	0.51	0.33	7.11	0.26
5	10	78.4	21.9	0.28	0.31	5.15	0.44	0.48	0.44	0.32	7.24	0.25
6	10	76.4	24.6	0.33		5.15	0.36	0.46	0.37	0.27	7.15	0.23
7	11	73.5	26.4	0.35	0.21	5.14	0.28	0.23	0.29	0.25	7.08	0.22
8	11	72.5	28.3	0.38		5.13	0.22	0.27	0.23	0.22	6.97	0.20
9	11-12	71.4	29.6	0.40	0.19	5.13	0.17	0.16	0.18	0.20	6.90	0.19
10	11-12	70.3	30.5	0.39		5.13	0.13	-.05	0.14	0.21	6.92	0.19
11	11-12	70.6	31.4	0.43		5.16	0.11	0.32	0.12	0.17	6.76	0.17
12	11-12	69.7	32.0	0.45		5.14	0.08	0.21	0.11	0.15	6.63	0.16
13	11-12	69.3	32.4	0.46	0.13	5.13	0.07	0.10	0.11	0.14	4.81	0.15

Table C.15: Experimental and modelling results of flow reactor run 5

RUN 5												
Velocity = ~2.8 m/s, Current = 34 Amps												
Total Cerium concentration(incl. solids) = 0.82 Molar												
Time	*Reactor Gas*			*Ce(IV)*	*Ce(III)*	*Cell*	*Current Efficiency*			*Model*		
	Rot.	*Molar %*		*conc.*	*conc.*	*Pot.*	*gas*	*conc.*	*best*	*Ce(III)*	*Pot.*	*Current*
hrs	*Flow*	H_2	O_2	*mol/l*	*mol/l*	*Volts*	*anal.*	*anal.*	*fit*	*mol/l*	*Volts*	Eff.
1	5	88.6	1.6	0.07	0.32	3.71	0.96	1.07	1.01	0.34	5.39	0.61
2	5	95.9	1.8	0.14		3.64	0.96	0.98	0.98	0.36	5.40	0.63
3	5	97.7	1.6	0.20	0.40	3.68	0.97	1.01	0.96	0.38	5.50	0.66
4	5	97.7	1.8	0.26	0.38	3.70	0.96	0.87	0.95	0.40	5.72	0.68
5	5	97.8	2.0	0.33		3.75	0.96	0.98	0.93	0.43	5.95	0.71
6	5-6	97.4	2.4	0.38	0.38	3.95	0.95	0.84	0.89	0.44	6.12	0.72
7	6	93.7	5.8	0.43	0.32	3.99	0.88	0.68	0.82	0.39	6.10	0.67
8	6-7	89.1	10.2	0.47		4.00	0.77	0.71	0.71	0.35	6.04	0.62
9	7	83.7	14.5	0.51	0.26	4.02	0.65	0.47	0.57	0.31	5.99	0.58

Table C.16: Experimental and modelling results of flow reactor run 6

RUN 6 *Velocity = ~1.1 m/s, Current = 34 Amps* *Total Cerium concentration(incl. solids) = 0.75 Molar*												
Time	*Reactor Gas*			*Ce(IV)*	*Ce(III)*	*Cell*	*Current Efficiency*			*Model*		
	Rot.	*Molar %*		*conc.*	*conc.*	*Pot.*	*gas*	*conc.*	*best*	*Ce(III)*	*Pot.*	*Current*
hrs	*Flow*	H_2	O_2	*mol/l*	*mol/l*	*Volts*	*anal.*	*anal.*	*fit*	*mol/l*	*Volts*	Eff.
1	8	85.7	13.6	0.05	0.36	4.21	0.68	0.74	0.72	0.31	5.45	0.37
2	7-8	84.4	14.4	0.11	0.34	4.28	0.66	0.84	0.71	0.33	5.47	0.38
3	7-8	84.6	14.1	0.15		4.29	0.67	0.65	0.70	0.34	5.35	0.39
4	7-8	84.0	14.0	0.20	0.40	4.32	0.67	0.71	0.69	0.36	5.54	0.41
5	7-8	83.6	14.7	0.25		4.25	0.65	0.71	0.68	0.38	5.72	0.42
6	7-8	86.7	13.8	0.29	0.41	4.32	0.68	0.68	0.67	0.40	5.89	0.43
7	7-8	86.5	14.8	0.33	0.40	4.37	0.66	0.57	0.65	0.41	6.03	0.44
8	7-8	87.4	16.0	0.38	0.36	4.42	0.63	0.72	0.61	0.37	6.02	0.41
9	8	85.0	18.4	0.42	0.33	4.44	0.57	0.56	0.57	0.33	5.97	0.38
10	8	82.0	20.5	0.45	0.30	4.44	0.50	0.43	0.50	0.30	5.92	0.36
11	8	80.1	22.6	0.47		4.45	0.44	0.38	0.41	0.28	5.87	0.34
12	8	78.6	24.1	0.49		4.45	0.39	0.25	0.30	0.26	5.83	0.33

Table C.17: Experimental and modelling results of flow reactor run 7

RUN 7												
Velocity = ~2.8 m/s(~1.1 m/s first 5 hrs) Current = 18 Amps												
Total Cerium concentration(incl. solids) = 0.76 Molar												
Time	*Reactor Gas*			*Ce(IV)*	*Ce(III)*	*Cell*	*Current Efficiency*			*Model*		
	Rot.	*Molar %*		*conc.*	*conc.*	*Pot.*	*gas*	*conc.*	*best*	*Ce(III)*	*Pot.*	*Current*
hrs	*Flow*	H_2	O_2	*mol/l*	*mol/l*	*Volts*	*anal.*	*anal.*	*fit*	*mol/l*	*Volts*	Eff.
1	5	84.8	9.8	0.03	0.31	3.20	0.77	0.90	0.84	0.31	3.94	0.68
2	5	84.8	9.8	0.06		3.25	0.77	0.87	0.81	0.32	3.93	0.70
3	5	83.4	8.8	0.10	0.38	3.25	0.79	0.90	0.82	0.33	3.93	0.71
4	4-5	89.0	8.6	0.13	0.37	3.25	0.81	0.84	0.85	0.34	3.93	0.73
5	5	86.9	8.3	0.15	0.36	3.27	0.81	0.81	0.88	0.35	3.93	0.74
6	4	91.4	1.6	0.19	0.43	2.83	0.97	0.95	0.90	0.36	3.63	0.96
7	3	91.2	0.2	0.22	0.42	2.85	0.99	0.90	0.92	0.37	3.68	0.96
8	0-5	91.4	0.0	0.25	0.41	2.85	1.00	0.87	0.93	0.38	3.72	0.96
9	3	84.4	0.0	0.28	0.41	2.85	1.00	0.87	0.93	0.39	3.76	0.97
10	3	91.1	0.0	0.31	0.43	2.86	1.00	0.67	0.93	0.40	3.79	0.97
11	0-5	88.9	0.1	0.34	0.39	2.98	1.00	0.95	0.92	0.41	3.83	0.97
12	0-5	90.6	0.0	0.37	0.36	3.00	1.00	0.87	0.92	0.39	3.84	0.96
13	0-5	93.7	0.0	0.40	0.34	3.02	1.00	0.84	0.91	0.36	3.85	0.96
14	0-5	91.5	0.1	0.43		3.06	1.00	0.70	0.91	0.33	3.86	0.95
15	0-5	92.4	0.2	0.46		3.09	1.00	0.98	0.89	0.30	3.88	0.94
16	0-5	91.2	0.6	0.48	0.27	3.15	0.99	0.56	0.85	0.28	3.90	0.93
17	0-5	90.8	2.1	0.50		3.18	0.95	0.64	0.78	0.26	3.92	0.90

Table C.18: Experimental and modelling results of flow reactor run 8

RUN 8												
Velocity = ~2.8 m/s, Current = 50 Amps												
Total Cerium concentration(incl. solids) = 0.75 Molar												
Time	*Reactor Gas*			*Ce(IV)*	*Ce(III)*	*Cell*	*Current Efficiency*			*Model*		
	Rot.	*Molar %*		*conc.*	*conc.*	*Pot.*	*gas*	*conc.*	*best*	*Ce(III)*	*Pot.*	*Current*
hrs	*Flow*	H_2	O_2	*mol/l*	*mol/l*	*Volts*	*anal.*	*anal.*	*fit*	*mol/l*	*Volts*	Eff.
1	6.5	92.3	7.9	0.09	0.28	4.55	0.83	0.95	0.88	0.32	6.94	0.41
2	7	93.9	6.5	0.18	0.30	4.56	0.86	0.88	0.88	0.35	6.89	0.43
3	7-8	93.8	6.5	0.27	0.36	4.60	0.86	0.88	0.86	0.39	7.46	0.45
4	7-8	92.7	7.7	0.34	0.38	4.64	0.83	0.78	0.82	0.41	7.91	0.47
5	7.5	88.7	12.3	0.42	0.32	4.69	0.72	0.83	0.75	0.33	7.75	0.41
6	7-8	83.5	17.3	0.49	0.25	4.71	0.59	0.63	0.64	0.26	7.52	0.36
7	10	79.7	21.8	0.54	0.23	4.73	0.45	0.50	0.47	0.22	7.28	0.31

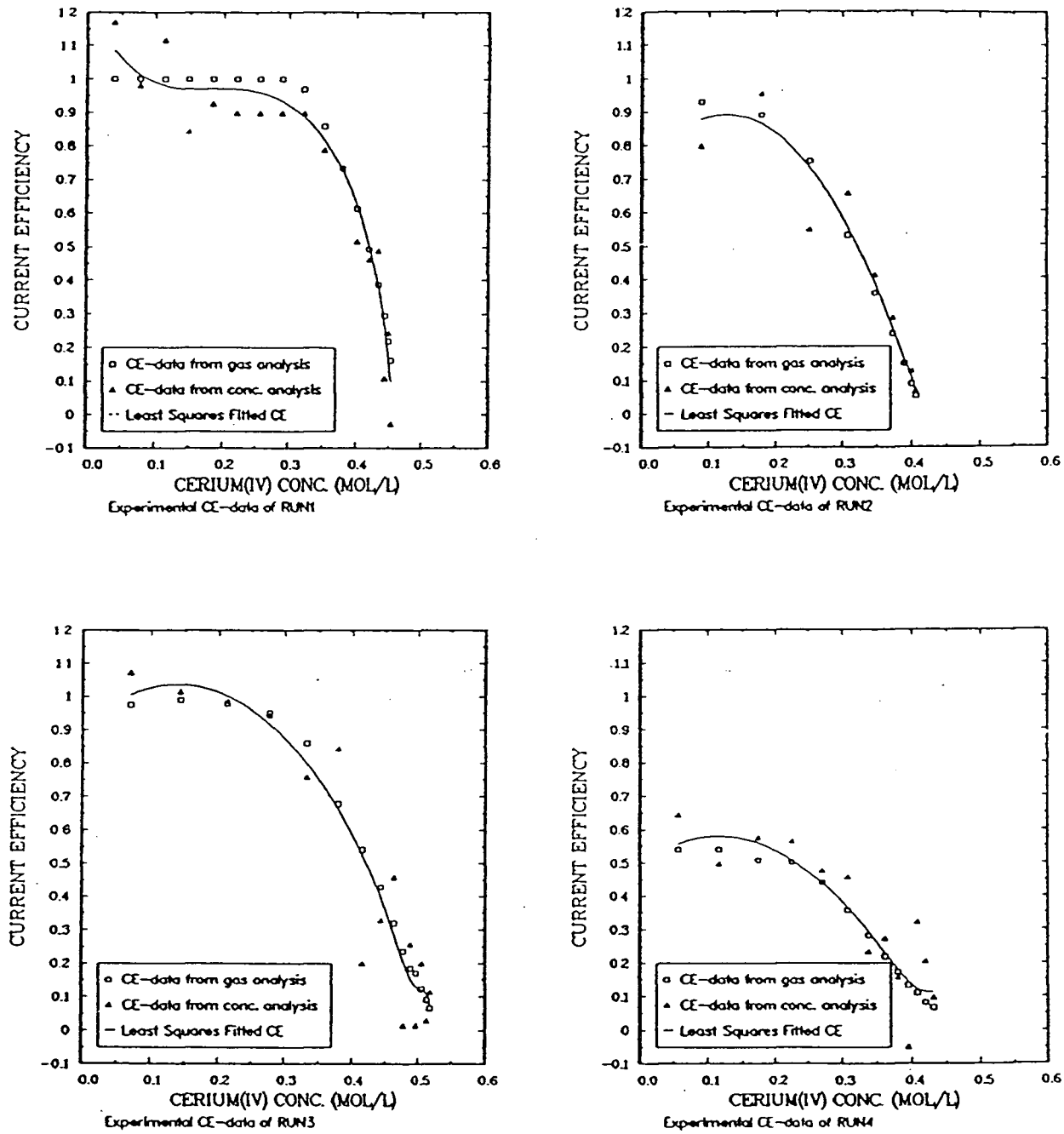

Figure C.33: Cell current efficiencies as determined from the gas analysis and the concentration analysis of runs 1 - 4.

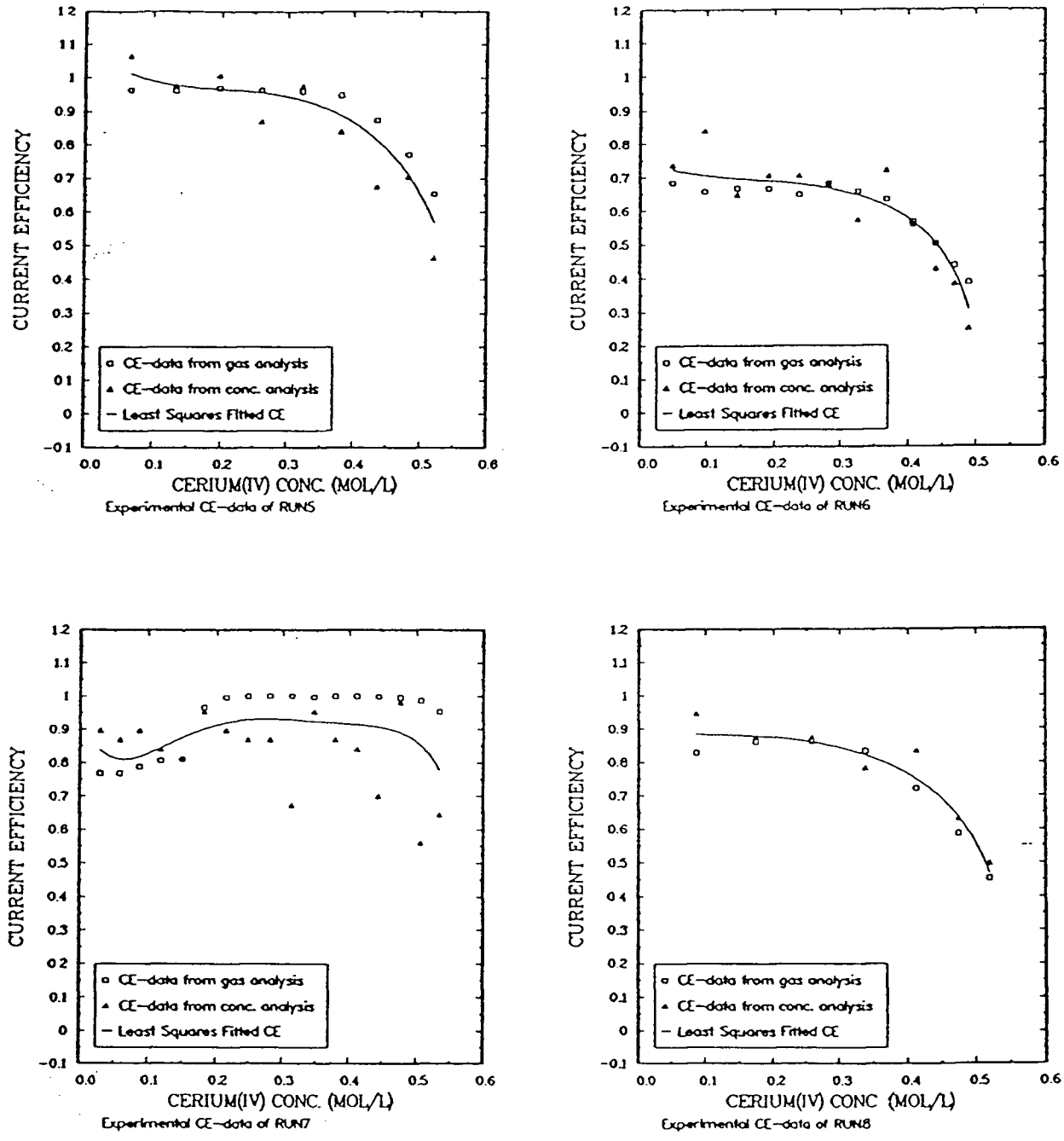

Figure C.34: Cell current efficiencies as determined from the gas analysis and the concentration analysis of runs 5 - 8.

Appendix D

Model Algorithm, Sample Calculations

D.1 Semi-Empirical, Semi-Mechanistic Model Algorithm

1. Calculate the anode and cathode superficial current densities for all runs.
2. Calculate the Reynolds number for all runs based on the equivalent diameter of 1.262 cm^2 and a presumed constant kinematic viscosity of 0.01 cm^2/sec.
3. Convert the Reynolds number to an equivalent rotating disc rotational speed (see Sample Calculation 3, this Appendix).
4. Read the data and compute dissolved cerous sulfate concentration. If the sum of the cerium(IV) and cerium(III) concentrations exceeds the total cerium concentration, the cerium(III) concentration is put equal to the total cerium concentration minus the cerium(IV) concentration.
5. Compute the limiting current density of the cerium(III) oxidation reaction at the anode with the Tafel slopes and intercepts of this reaction and the oxygen evolution reaction using the empirically obtained relationships of chapter five.
6. Calculate the anode potential. This can be done by manipulating the Tafel equations of the oxygen evolution reaction and the cerium oxidation reaction and using the total superficial anode current density which is known.

$$i_{total} = \frac{10^{\frac{V-Ce_{Tint}}{Ce_{Tslo}}}}{1+\frac{1}{i_{lim}}10^{\frac{V-Ce_{Tint}}{Ce_{Tslo}}}} + \frac{10^{\frac{V-Ox_{Tint}}{Ox_{Tslo}}}}{10,000} \tag{D.36}$$

Ce_{Tint} Tafel intercept of the cerium oxidation reaction

Ce_{Tslo} Tafel slope of the cerium oxidation reaction

Ox_{Tint} Tafel intercept of the oxygen evolution reaction

Ox_{Tslo} Tafel slope of the oxygen evolution reaction

i_{lim} limiting current density in Amps/cm^2

i_{total} total anode current density in Amps/cm^2

V anode potential in Volts with reference to the standard calomel electrode

The above equation has one unknown, V, and can thus be solved.

7. Now the anode current efficiency can be calculated by calculating the partial current density of the cerium oxidation reaction and dividing it by the total current density.

8. Assuming 100% current efficiency at the cathode gives the total current efficiency of the reactor.

9. The cathode potential can be calculated at any one time throughout the run using the four regions based on cerium(III) and cerium(IV) concentrations as outlined in chapter five. This potential is negative with respect to the standard calomel electrode.

10. The potential drop across the gap between the electrodes can be found from the simplified equation:

$$V_{iR} = \frac{W(i_{cath} + i_{an})}{2\kappa} \tag{D.37}$$

V_{iR} potential drop in Volts

W electrode gap in cm

i_{cath} cathode current density in Amps/cm^2

i_{an} anode current density in Amps/cm^2

κ conductivity in mho.cm, which is taken as 0.64 mho.cm, an average number obtained from BC Research for cerous sulfate solutions at 50 degrees Celsius.

The effect of gas hold-up has been neglected since the iR-drop at the rotating wire (cathode) did not seem to increase with current density. It is suspected that the effect of the gas on the conductivity is relatively small as compared to the experimental error in the potential values.

11. The cell potential is equal to the sum of the anode and cathode potentials added to the potential drop across the electrode gap.

D.2 Sample Calculation One

Calculation of the overall differential current efficiency for the production of cerium(III) in the tube and wire reactor from:

1. cerium(IV) concentration data

example, run 2

velocity	~2.8 m/s
current	50 Amps
reactor volume	18.3 liters
initial cerium(IV) concentration	0 mol/l
cerium(IV) concentration after 1 hr	0.082 mol/l
reactor gas composition after 1 hr:	90.7 molar % H_2
	3.3 molar % O_2

At 100% current efficiency, the change in concentration is:

$$\frac{50 \text{ Coulombs/sec}}{96500 \text{ (Faraday's no.)}} = 0.000518 \text{ mol/sec}$$

The actual change in concentration is 0.08 mol/l.hr

The overall average current efficiency over the first hour of the run is:

$$\frac{(0.082 \text{ mol/l.hr})(18.3 \text{ l})}{(3600 \text{ sec/hr})(0.000518 \text{ mol/sec})} = 0.80$$

2. gas composition data

Assume a cathode current efficiency of 100%. Then, the anode current efficiency is equal to the overall current efficiency and the number of electrons consumed in the production of hydrogen gas corresponds to the total number of electrons passed through the cell. Also, each mole of hydrogen gas comsumes two moles of electrons,

whereas, each mole of oxygen gas delivers four moles of electrons. Consequently, the anode current efficiency is:

$$1 - \frac{O_2 \text{ (molar\%)}}{H_2 \text{ (molar\%)}} \times \frac{4}{2} = 1 - \frac{3.3}{90.7} \times 2 = 0.93$$

Since both gases are at the same pressure and temperature, the effect of these parameters and the effect of the volumetric flow cancels out.

The assumption of a 100% cathode current efficiency is supported by the close agreement of the current efficiency calculations based on the gas composition data and those based on the cerium(IV) concentration data (see Appendix C, Tables C.11 - C.18, Figures C.33 - C.34).

D.3 Sample Calculation Two

Analysis of a balanced factorial of otherwise randomly chosen observations.

The data is taken from the experimental results of the tube and wire reactor runs which are tabulated in Appendix C, Tables C.11 - C.18.

Data taken from run:hour	*variable 1* Ce^{IV} *conc. mol/l*	*variable 2 total Ce conc. mol/l*	*dependent var. dissolved* Ce^{III} *mol/l*	*12 interaction*
2:1	0.081 (-)	0.51 (-)	0.275	+
5:1	0.071 (-)	0.82 (+)	0.319	-
4:4	0.234 (+)	0.60 (-)	0.333	-
7:8	0.251 (+)	0.76 (+)	0.413	+

Average dissolved cerium(III) concentration = 0.335 mol/l

Variable	*Main Effects*
1	0.152
2	0.124
	Interactive Effect
12	0.036

The above can be repeated for other experimental data. It is seen that the interactive effect is small and, therefore, not apparent. The main effects have definite values of comparible magnitude indicating that both, the cerium(IV) and the total cerium concentrations, affect the dissolved cerium(III) concentration in an approximately equally strong positive way.

D.4 Sample Calculation Three

Converting Reynolds number to an equivalent rotational speed of the rotating disc electrode.

Generally, the diffusion layer thickness of a rotating disc electrode is given by

$$\delta = 1.61 D^{\frac{1}{3}} \nu^{\frac{1}{6}} \omega^{-\frac{1}{2}} \tag{D.38}$$

δ diffusion layer thickness, cm

D diffusion coefficient, cm^2/s

ν kinematic viscosity, cm^2/s

ω rotational speed, rad/s

Turbulent pipe flow is represented by the Chilton and Colburn equation

$$Sh = \frac{d_{eq}}{\delta} = 0.023 Re^{0.8} \left[\frac{\nu}{D}\right]^{\frac{1}{3}} \tag{D.39}$$

Sh Sherwood number

d_{eq} equivalent pipe diameter, cm

Re Reynolds number

Substituting equation 1 into equation 2 and simplifying the result gives:

$$\omega = \frac{0.00137 \nu Re^{1.6}}{d_{eq}^2} \tag{D.40}$$

example:

$$Re = \frac{d_{eq} \times \text{velocity}}{\nu} = \frac{1.262\text{cm} \times 280\text{cm/s}}{0.01\text{cm}^2/\text{s}} = 35,336$$

$$\omega = \frac{0.00137 \times 0.01 \times 35336^{1.6}}{1.262^2} = 162.8\text{rad/s} = 1555 \text{ rpm}$$

In the reactor, the equivalent ω lies between 400 and 1600 rpm.

D.5 Sample Calculation Four

The possible effect of gas evolution at low rotational speeds of the Rotating Disc Electrode assuming Stephan and Vogt's model [45].

At a rotating disc electrode (see sample calcultation three):

$$\delta = 1.61 D^{\frac{1}{3}} \nu^{\frac{1}{6}} \omega^{-\frac{1}{2}}$$

Assuming,

D = 2×10^{-6} cm^2/s

ν = 0.01 cm^2/s

ω = 1000 rpm = 104.72 rad/s

Then, δ = 0.00092 cm

$$k_{mc} = \frac{D}{\delta} = \frac{2 \times 10^{-6}}{0.00092} = 0.00217 \text{cm/s} \qquad \text{(D.41)}$$

k_{mc} the macroconvective mass transfer coefficient, cm/sec

In addition to Stephan and Vogt's model, assume:

- 100% efficiency of gas evolution
- a reactor pressure of 1.5 atmospheres,[1] P
- a constant temperature of 50 degrees Celsius (323 degrees Kelvin), T
- that the ideal gas law holds

(the ideal gas law constant, R, is 82.057 atm.cm^3/mol.K)

- an average bubble diameter of 40×10^{-4}cm, d
- a partial current density of the oxygen evolution reaction of 0.2 Amps/cm^2

The number of moles evolved, n, equals:

$$n = \frac{0.2 \text{ Coulombs/sec.cm}^2}{96500 \text{ Coulombs/mol e's } \times 4 \text{ mol e's/mol } O_2} = 5.18 \times 10^{-7} \text{ mol/sec.cm}^2$$

[1] This is based on the pressure gauge reading which indicated a gauge pressure of 17 psi immediately after the pump at full velocity. If the pressure drop before and after the reactor is approximately the same, the reactor pressure would be ~1.5 atmospheres absolute.

The volumetric flow rate of evolved gas, V_G, per unit area, A, is:

$$\frac{V_G}{A} = \frac{nRT}{P} = \frac{(5.18 \times 10^{-7})(82.057)(323)}{1.5} = 0.00916 \text{ cm}^3/\text{cm}^2.\text{sec}$$

From the model (see chapter two):

$$\begin{aligned} k_c &= \frac{D}{d} 0.93 \left[\frac{V_G d}{A\nu}\right]^{0.5} \left[\frac{\nu}{D}\right]^{0.487} \\ k_c &= \frac{2 \times 10^{-6}}{40 \times 10^{-4}} 0.93 \left[\frac{(0.00916)(40 \times 10^{-4})}{0.01}\right]^{0.5} \left[\frac{0.01}{2 \times 10^{-6}}\right]^{0.487} \\ k_c &= 0.00178 \text{ cm/sec} \end{aligned}$$

k_c the microconvective mass transfer coefficient, cm/sec

The overall mass transfer coefficient, k, can be found from the design equation proposed be Vogt [55]:

$$k = [k_c^2 + k_{mc}^2]^{0.5} = 0.00281$$

This illustrates a 29% increase in mass transfer through the evolution of bubbles. A few more cases have been calculated in which some of the parameters were changed to observe the effect on mass transfer enhancement.

Conditions as above, but with a reactor pressure of one atmosphere

$$\frac{V_G}{A} = 0.0137 \text{ cm}^3/\text{cm}^2.\text{sec}$$

$$k_c = 0.00218 \text{ cm/sec}$$

$k = 0.00308$ cm/sec, a 42% increase in mass transfer

Initial conditions, but with a reactor pressure of one atmosphere and a diffusion coefficient, D, equal to 5×10^{-6} cm^2/sec.

$$\delta = 0.00125 \text{ cm}$$

$$k_{mc} = 0.0040 \text{ cm/sec}$$

$$k_c = 0.0035 \text{ cm/sec}$$

$k = 0.0053$ cm/sec, a 33% increase in mass transfer

Initial conditions, but at a rotational speed, ω, of 50 rad/sec.

$$k_{mc} = 0.00150 \text{ cm/sec}$$

$$k_c = 0.00178 \text{ cm/sec}$$

$k = 0.0023$ cm/sec, a 55% increase in mass transfer

D.6 Sample Calculation Five

Converting the Reynolds number from the flow reactor to an equivalent rotational speed of the rotating wire electrode.

The diffusion layer thickness, δ, of a rotating wire electrode can be predicted from the equation of Eisenberg, Tobias, and Wilke [14].

$$\delta = 99.62 \frac{d_i^{-0.40} \nu^{0.344} D^{0.356}}{S^{0.70}}$$

d_i the diameter of the rotating wire = 0.47 cm

S the rotational speed in rpm

ν kinematic viscosity = 0.01 cm^2/sec

D diffusion coefficient = 2×10^{-6} cm^2/sec

From the Chilton Colburn equation:

$$\frac{d_{eq}}{\delta} = 0.023 Re^{0.8} \nu^{\frac{1}{3}} D^{-\frac{1}{3}}$$

d_{eq} the equivalent flow reactor diameter, cm

Re Reynolds number

Equating and simplifying the above two equations gives:

$$S^{0.70} = 0.216 Re^{0.8}$$

The reactor velocities were 110 cm/sec and 280 cm/sec which corresponds to ~6000 rpm and 17,500 rpm, respectively.

D.7 Sample Calculation Six

The hydrogen ion concentration at the rotating wire electrode surface. The diffusion layer thickness of the rotating wire electrode can be calculated from the equation of Eisenberg, Tobias, and Wilke [14]. The conditions chosen for this calculation are a rotational speed of 1000 rpm and a diffusion coefficient (of hydrogen) of 9×10^{-5} cm^2/sec. For other parameter values see sample calculation five.

$$\begin{aligned}
\delta &= 99.62\frac{d_i^{-0.40}\nu^{0.344}D^{0.356}}{S^{0.70}} \\
\delta &= 99.62\frac{(0.476\text{cm})^{-0.40}(0.01\text{cm}^2/\text{sec})^{0.344}(9\times10^{-5}\text{cm}^2/\text{sec})^{0.356}}{1000\text{ rpm}} \\
\delta &\sim 0.0010\text{ cm}
\end{aligned}$$

Also, assume that the current density is 3 Amps/cm^2 and that the bulk concentration of sulfuric acid is 1.6 molar = 0.0016 mol/cm^3. The number of moles of hydrogen ions consumed at the electrode has to equal the number of moles diffusing towards the electrode during steady state conditions. Or,

$$\frac{3\text{ C/sec.cm}^2}{96500} = \frac{9\times10^{-5}\text{ cm}^2/\text{sec}}{0.001\text{ cm}}[0.0016\text{ mol/cm}^3 - x]$$

Here, x is the hydrogen ion concentration at the electrode surface and is calculated as 1.25 molar. A few more calculated x-values are listed in the following table.

Current Density	*Rotational Speed*	x
Amps/cm^2	*rpm*	*moles/liter*
3	6000	1.54
1	1000	1.48
1	6000	1.58